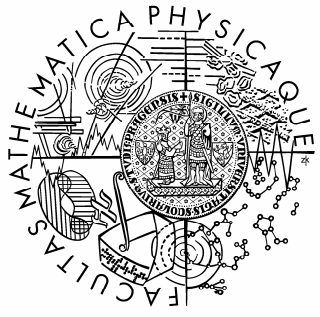

FACULTY
OF MATHEMATICS
AND PHYSICS
Charles University

DOCTORAL THESIS

Jani Jabloňků

Plasmonic biosensing on the microscale and nanoscale

Institute of Photonics and Electronics, v.v.i.
The Czech Academy of Sciences

Supervisor of the doctoral thesis: Prof. Jiří Homola, Ph.D., DSc.
Study programme: Physics
Study branch: Physics of nanostructures

Prague 2017

I declare that I carried out this doctoral thesis independently, and only with the cited sources, literature and other professional sources.

I understand that my work relates to the rights and obligations under the Act No. 121/2000 Coll., the Copyright Act, as amended, in particular the fact that the Charles University has the right to conclude a license agreement on the use of this work as a school work pursuant to Section 60 paragraph 1 of the Copyright Act.

In Prague, ……..

……..
Jani Jabloňků

Title: Plasmonic biosensing on the microscale and nanoscale

Author: Jani Jabloňků

Department / Institute: Institute of Photonics and Electronics, v.v.i, The Czech Academy of Sciences

Supervisor of the doctoral thesis: Prof. Jiří Homola, Ph.D., DSc., Department of Optical Biosensors, Institute of Photonics and Electronics, v.v.i

Abstract: Optical biosensors based on surface plasmon resonance (SPR) represent an advanced, label-free technology for studying biomolecular interactions and for rapid and sensitive detection of biological and chemical agents. In this doctoral thesis, the extension of the technology towards the microscale and nanoscale is pursued. The work includes both theoretical and experimental aspects. In particular, the presented resuls include the development of a plasmonic sensor platform with its sensitive area miniaturized to the microscale, detection of individual analyte molecules through nanoparticle labels, determination of the influence of nanoparticle-label size on the response enhancement in SPR biosensors and the development of a biosensor based on localized surface plasmons on nanoparticles and verification of the nanoscale localization of its sensitivity.

Keywords: surface plasmon, biosensor, SPR, nanoparticles

Název práce: Plasmonické biosenzory v mikro- a nano-škále

Autor: Jani Jabloňků

Katedra / Ústav: Ústav fotoniky a elektroniky, v.v.i, Akademie věd České republiky

Vedoucí disertační práce: prof. Ing. Jiří Homola, CSc., DSc., Oddělení optických biosenzorů, Ústav fotoniky a elektroniky, v.v.i

Abstrakt: Optické biosenzory založené na rezonanci povrchových plasmonů (SPR) představují velmi pokročilou technologii pro výzkum biomolekulárních interakcí a pro detekci chemických a biologických látek. V této dizertační práci je prezentována snaha o rozšíření této technologie do oblasti mikroškály a nanoškály. Práce obsahuje jak teoretické, tak experimentální aspekty. Mezi dosažené výsledky patří: vývoj plazmonové senzorické platformy s citlivou plochou v řádu mikrometrů, detekce jednotlivých molekul pomocí jejich značkování nanočásticemi, osvětlení vlivu velikosti nanočástic použitých jako značky na zesílení odezvy v SPR senzorech a vývoj biosenzoru založeného na rezonanci lokalizovaných povrchových plasmonů na nanočásticích a ověření lokalizace citlivosti tohoto senzoru v řádu nanometrů.

Klíčová slova: povrchové plasmony, biosenzory, SPR, nanočástice

To my beloved family

Table of Contents

1 Introduction

Surface plasmons (SPs) were first observed as anomalies in the reflection spectra of metallic gratings around 1902 by Wood [1], with the explanation of the surface plasmon resonance (SPR) phenomena presented several decades later by Fano [2] and Ritchie [3]. Intensive theoretical and experimental studies followed [4-6]. In the last two or three decades, surface plasmons have found applications outside the field of solid state physics, especially in biosensors [7], enhancement of Raman scattering [8], subwavelength imaging and microscopy [9] and photovoltaic cell development [10], becoming a rather broad interdisciplinary field.

Since late 1990s, the SPR on thin gold layers has found an increasingly important application in the field of biochemical analytics – biosensors based on SPR have become a key tool of biomolecular interactions studies both in life sciences and pharmaceutical research [11], offering real-time analysis. Additionally, they have been increasingly applied in the detection of chemical and biological substances in important areas such as medical diagnostics, environmental monitoring, food safety and security. Among label-free optical biosensor technologies, SPR biosensors today belong to the most advanced [12].

The manifestations of surface plasmons on nanoparticles (localized surface plasmons, LSP; localized surface plasmon resonance, LSPR) have on the other hand been known since antiquity as the bright colours of glass stained with gold and silver colloids [13]. In the 1970s, enhancement of Raman scattering by metal surfaces roughened on the nanoscale has been observed [14] and ascribed to surface plasmons [15]. Later advances in fabrication and characterization technologies [16-19] on the nanoscale enabled the development of the field of nanoplasmonics [20]. The development of biosensors based on plasmonic nanostructures has since become a subject of extensive research [21-30].

1.1 Propagating and localized surface plasmons

Plasmons (or plasma waves) in metals are coherent oscillations of the metal's conduction electrons[*]. The waves can propagate either in the bulk of the metal or along the metal's surface as surface waves (surface plasmons, surface plasma waves). When coupled with photons, they're termed surface plasmon polaritons. Particles comparable to or smaller than the wavelength of light can also support oscillations of its conduction electrons and these are termed the localized surface plasmons.

1.1.1 Propagating surface plasmons on metal-dielectric interfaces

A propagating surface plasmon is an electromagnetic wave that propagates along a boundary (interface) between a metal and a dielectric [6]. The electromagnetic field of a propagating SP is confined to the vicinity of the dielectric-metal boundary and decays exponentially into both media (Figure 1). The propagation constant of a propagating SP β_{SP} can be expressed as:

[*] While the majority of the field of plasmonics lies in the area of classical physics and optics and does not rely upon quantum effects, there is a convention of using the quantum-mechanic term "surface plasmons" instead of "surface plasma waves". We shall follow this convention.

$$\beta_{SP} = \frac{\omega}{c}\sqrt{\frac{\varepsilon_m \varepsilon_d}{\varepsilon_m + \varepsilon_d}}, \quad (1)$$

where ω is the angular frequency, c is the speed of light in vacuum, and ε_m and ε_d are the permittivities of the metal and dielectric medium, respectively. The propagating SP can only exist if the following condition is fulfilled:

$$\mathrm{Re}\,\varepsilon_m < 0 \;\text{ and }\; |\mathrm{Re}\,\varepsilon_m| > \varepsilon_d\,. \quad (2)$$

That is the case for gold, silver and aluminium at visible and near-infrared frequencies. The typical penetration depth of the electromagnetic field into the dielectric and into the metal is on the order of hundreds of nanometers and tens of nanometers, respectively. A typical profile of the SP field is shown in Figure 1.

Due to the ohmic losses in the metal, all SPs are lossy as well and this is manifested in the imaginary part of the propagation constant β_{SP}. The typical propagation length for SPs on thin gold layers is on the order of ten micrometers.

The propagation constant β_{SP} of a propagating SP is always higher than the wavenumber of a free-space lightwave propagating through the dielectric medium. Therefore, in order to excite the propagating SP, i.e. to create a coupling between the free-space lightwave and the SP, a special arrangement is necessary.

In practice, gold is the most often used metal, owing to its chemical stability. While silver provides SPs with longer lifetimes and thus decreased bandwidth, a property desirable for the increased performance of a sensor, the challenges associated with higher reactivity of silver usually preclude its use outside of research settings.

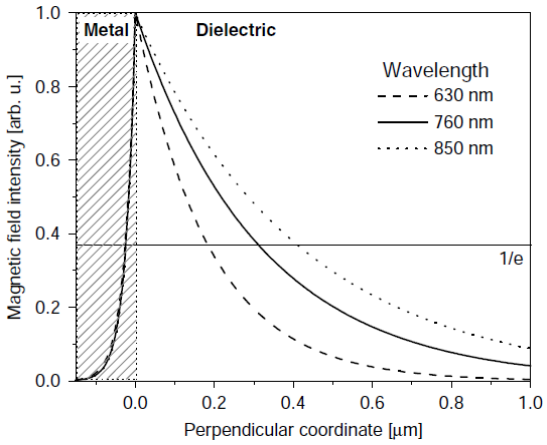

Figure 1. Distribution of the magnetic field of a propagating SP at the gold–water interface for three different wavelengths. From [12].

Excitation on planar surfaces

In case of optical excitation of propagating SPs on planar surfaces, attenuated total reflection (ATR) in an optical prism is the most used configuration. In the so-called Kretschmann configuration [31], a thin metal layer (e.g. 50 nm of gold) is deposited on the prism (Figure 2). The light wave in the prism undergoing ATR couples to the SP on the opposite side of the metal layer. The refractive index of the dielectric on the opposite side (typically water or air) has to be lower than the refractive index of the prism. The opposite side is typically the inside of a microfluidic chamber.

In practice, the thin metal layer is actually deposited on a glass slide (forming the dispos-

able “SPR chip”) instead of on the prism and the slide is then contacted with the prism via an refractive index matching oil. The metal layer is usually deposited by means of thermal evaporation in vacuum.

The coupling between the lightwave incident from the prism and the propagating SP only occurs when the lightwave’s wavevector component parallel to the boundary matches the propagation constant of the SP, i.e. when

$$\mathrm{Re}\,\beta_{\mathrm{SP}} = \frac{\omega}{c} n_{\mathrm{p}} \sin\theta\,, \tag{3}$$

where n_{p} is the refractive index of the prism.

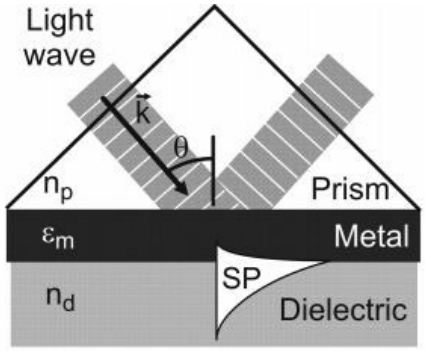

Figure 2. Excitation of surface plasmons in the Kretschmann geometry of the attenuated total reflection method. From [32].

Excitation on gratings and structured surfaces

The mismatch between the propagation constant of the SP β_{SP} and the wavevector component of the incident lightwave parallel to the boundary $k_{||} = (\omega/c) n_{\mathrm{d}} \sin\theta$ can also be bridged when the surface of the metal is not purely planar, but has a grating profile with the period Λ and wavevector size $G = 2\pi/\Lambda$. For grating vector **G** lying in the plane of incidence, the incident lightwave is coupled with SP when

$$k_{||} = \pm\,\mathrm{Re}\,\beta_{\mathrm{SP}} + mG, \quad m = 0, \pm 1, \pm 2, \ldots\,, \tag{4}$$

where m is the diffraction order (see Figure 3). The diffraction order that excites the SP is always evanescent.

Besides periodic grating profiles, the profiles of sharp nonperiodic or quasiperiodic structures or even profiles of random surface roughness can contain in their spatial frequencies spectrum such components which are suitable for satisfying the matching condition and can therefore serve to couple incoming energy into and out of the propagating SP (in the case of surface roughness it is an undesirable effect).

1.1.2 Localized surface plasmons on metallic nanoparticles

Localized surface plasmons are the collective oscillations of the conduction electrons of a metallic particle whose size is comparable to or smaller than the wavelength of light [13]. The attraction between the positively charged metal lattice and the cloud of conduction electrons displaced by an incident electromagnetic wave acts as the restorative force, possibly leading to resonant behaviour. The electromagnetic field of the localized SP is decaying into the surrounding medium faster than in the case of propagating SPs on planar surfaces and its penetration depth ranges from nanometers to tens of nanometers for noble me-

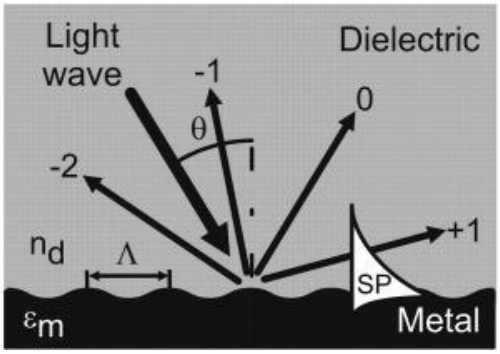

Figure 3. Excitation of propagating SPs via a grating coupler by the -2^{nd} order. From [11].

tal nanoparticles in optical and near-infrared frequencies. While propagating SPs have a continuum of frequencies and associated wavenumbers, localized SPs are discrete modes. The frequency of the localized SP mode depends on the size, shape and type of metal. While spherical noble metal nanoparticles have their SP bands in the visible, with increasing elongation of the nanoparticles the SP band can red-shift to near-infrared.

Unlike propagating SPs, localized SPs on nanoparticles couple with incident free-space lightwaves without the need for any special coupling arrangements. Similarly to propagating SPs, localized SPs are lossy modes. The quality factor of the mode for gold nanoparticles is highest for elongated particles thanks to the lower ohmic losses in gold in the near-infrared in comparison to the visible region.

Noble metal nanoparticles can be fabricated either by chemical means, i.e. growth from solution (the "bottom-up" approach) or by lithographic mean, usually by electron beam (EBL) or optical lithography (the "top-down" approach). Gold is the material of choice for NPs in plasmonic biosensors, since the small size of nanoparticles requires even higher chemical stability than is the case for planar surfaces and propagating SPs.

Noble metal nanoparticles are very strong scatterers within their SP bands. Their extinction cross-section can be an order of magnitude higher than their geometrical cross-section, while the extinction cross-section of dielectric nanoparticles is significantly smaller than their geometrical cross-section [13]. (Extinction is defined as the sum of absorption and scattering.) In the approximation of particles small compared with the wavelength λ, it can be shown that the extinction cross-section $C_{\text{ext}}(\lambda)$ for a spherical particle of permittivity $\varepsilon_1(\lambda)$ in a dielectric medium of permittivity ε_m is proportional to [13]

$$C_{\text{ext}}(\lambda) \sim \text{Im}\left\{\frac{\varepsilon_1(\lambda)-\varepsilon_m}{\varepsilon_1(\lambda)+2\varepsilon_m}\right\} \tag{5}$$

A maximum, i.e. an extinction band corresponding to the resonant excitation of a localized SP, is thus found at frequencies where $\text{Re}\{\varepsilon_1(\lambda)+2\varepsilon_m\} \approx 0$ is close to zero. For elongated particles, the condition changes to $\text{Re}\{\varepsilon_1(\lambda)+L\varepsilon_m\} \approx 0$ where L increases with with increasing elongation of the particle, reaching $L=12$ for aspect ratio of 1:4. Clearly, the position of the localized SP band is also sensitive to the refractive index of the surrounding medium. The dependence of the extinction spectrum of a 30 nm gold nanoparticle on the refractive index of its medium is shown in Figure 4.

Particles larger than about 100 nm are usually not suitable for plasmonic sensors because radiative damping causes significant broadening of the LSPR band, limiting the precision of the determination of its position and thus the performance of the sensor utilizing the particle.

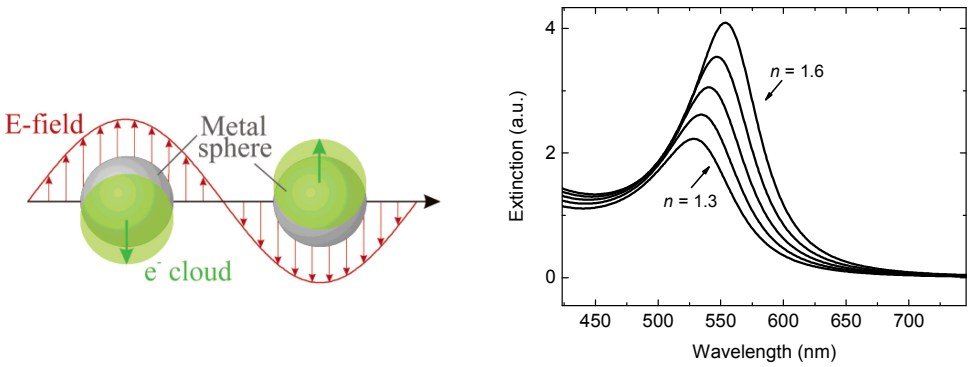

Figure 4. Left: Schematic representation of the oscillation of the conduction electrons a metallic nanosphere when driven by an incident lightwave (from [33]). **Right:** Dependence of the extinction spectrum of a 30 nm gold spherical nanoparticle on the refractive index of its medium.

1.2 Biosensors based on plasmonic optical transducers

Biosensors are analytical devices, which determine the presence and/or other properties of an analyte (molecule or other small organic particle) by means of the combination of a biological recognition element (molecule) and a transducer (Figure 5) [32]. The biorecognition element (molecule) is immobilized at the biosensor surface and specifically binds to (recognizes) the analyte thanks to its high chemical affinity towards the analyte and low affinity to other molecules, and is usually an antibody, an enzyme, a nucleic acid or an aptamer. The transducer then converts the binding within most of the surface or within a part of the surface (the sensitive area) into a more easily measurable quantity, optical, electrical or mechanical. Specifically, refractometric optical biosensors with surface plasmons take advantage of the increase in the refractive index near the surface of the biosensor upon the binding and accumulation of analyte molecules, as the refractive index of biomacromolecules is higher than that of water or other background fluid (e.g. blood serum). The properties of the surface plasmons excited at the surface change upon the change in refractive index and the measurement of SP properties is used to determine the extent of analyte binding.

The biorecognition element molecules can be either immobilized directly or through functional groups or biomolecular linkers within additional functional layers (see 1.2.2). These functional layers are usually added to reduce the non-specific binding to the biosensor surface [12] and to provide optimal orientation of the binding sites of the biorecognition elements to capture the analyte effectively.

The biosensor surface usually forms one of the walls of a microfluidic chamber that is used along with some sort of tubing and pump systems to transport the sample liquid containing the analyte towards the biosensor surface.

1.2.1 Optical arrangements and platforms of plasmonic biosensors

Propagating SPs

Most optical platforms upon which biosensors with propagating SPs are based excite the SPs in the Kretschamann configuration, i.e. through the attenuated total reflection (ATR) (Figure 2) in an optical prism coupler on a thin metal layer (typically, about 50 nm of gold). Alternatively, a grating coupler is used, wherein the gold surface has a periodic relief which p rovides matching of the wavectors between the incident light and SPs.

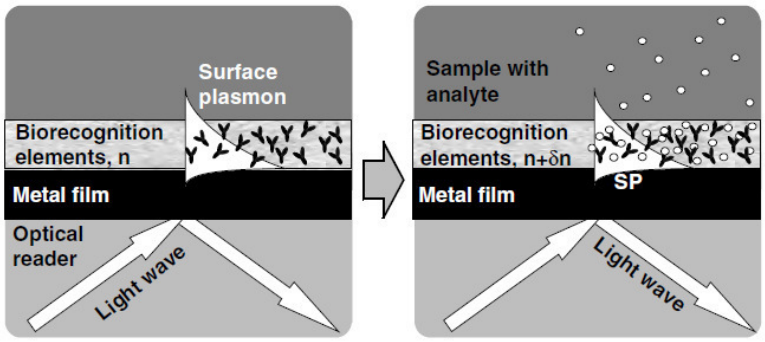

Figure 5. Principle of operation of a SPR biosensor. From [11].

There are three main optical arrangements that can be applied to both the prism-coupled and grating-coupled SPR platforms, shown schematically in Figure 6 (a), (b) and (c), respectively:

- Multiple wavelengths, single angle (wavelength interrogation): here, a polychromatic lightsource (an incandescent, a LED or super-luminescent LED). Changes in the resonant wavelength are tracked.
- Single wavelength, multiple angles (angular interrogation): usually, a convergent laser beam illuminates the surface where SPs are excited, and the divergent fan is incident on a 1D array detector (a CCD array or a photodiode array). Changes in the resonant angle are tracked.
- Single wavelength, single angle: a collimated monochromatic beam illuminates the surface where SPs are excited and the intensity of the reflected light is measured by a photodetector. This approach is suitable for parallel measurement in high numbers (tens to hundreds) of channels, with the photo-detector then being a high-speed 2D CCD or CMOS camera.

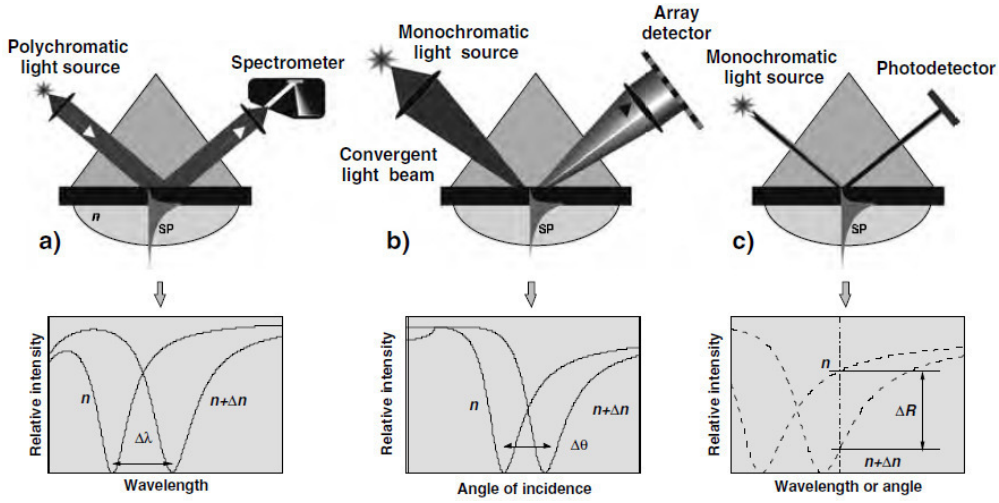

Figure 6. Optical arrangements of biosensors with propagating SPs based on modulation of (a) wavelength, (b) angle of incidence, and (c) light intensity. From [11] .

Localized SPs

Noble metal nanoparticles supporting localized SPs can be utilized in biosensors in three ways:

1. As the core of the biosensor's transducer, with the analyte binding inducing a shift of the LSPR band (analogously to biosensors with propagating SPs). The nanoparticle can be either:
    a. immobilized on or fabricated on a planar substrate (usually glass) [30].
    b. suspended in solution [34, 35], or
2. As response enhancing labels for use in sensors based on propagating SPs [36, 37], where the NPs are bound to the analyte molecules captured at the biosensor surface and the high optical cross-section of NPs enhances the response due to analyte capture.

Optical platforms for case 2. have been discussed in the previous sub-chapter. The case 1.b. of nanoparticles suspended in solution is beyond the scope of this thesis.

The optical platforms of sensors utilizing localized SPs on nanoparticles on planar substrates (1.a.) are much more varied than those of propagating SP platforms. Since the localized SPs on nanoparticles or on arrays of nanoparticles can be readily excited by a free-space lightwave, they do not require prisms or other coupling devices and therefore the simplest collinear transmission arrangement of light source-nanoparticle array-detector is possible. However, more complex arrangements are often used to, for example, overcome turbidity of the sample liquid or to allow the use of non-transparent microfluidic hardware for sample delivery to the nanoparticle array. The ATR configuration can also be useful when there is a need to suppress the background light in order to increase the contrast of the signal from nanoparticles [38] or to excite propagating optical modes coupled with the localized SPs [39, 40]. Most of the above configurations can also be used in an optical microscope when there is a need for more spatial resolution [41, 42].

1.2.2 Surface functionalizations

The core of any biosensors is the biorecognition element (antibody, peptide, DNA/RNA, aptamer), which imparts to the biosensor chemical selectivity and specificity. The biorecognition element has to be immobilized on the properly chemically prepared surface of the biosensor. The ideal functional coating of the surface of the biosensor [12]

- provides the desired surface concentration of the biorecognition elements,
- provide optimum orientation of the binding sites of the biorecognition elements to capture the analyte molecules effectively,
- does not disturb the biological activity of the biorecognition elements,
- minimizes fouling, i.e. the nonspecific adsorption of molecules other than the analyte to the surface of the biosensor [43, 44].

The biorecognition element molecules can be immobilized either directly by e.g. electrostatic interaction, or by means of biomolecular linkers or functional groups incorporated in more complex functional layers [11]. A very often used technique employs the spontaneous self-organization of n-alkylthiols or disulfides on gold surfaces (Figure 7) [32]. These self-assembled monolayers (SAMs) have been employed in many immobilization methods for spatially controlled attachment of biomolecular recognition elements [45].

Functionalization of nanoparticles presents additional challenges due to very small radii of

curvature and multiple materials used (e.g. gold NPs on glass), but also new opportunities when selectively functionalizing areas of higher electric field strength [46, 47].

The choice of surface functionalization, especially the total thickness of the biomolecular layer including the analyte to be captured, can inform the selection of a plasmonic system with the corresponding penetration depth of its electromagnetic fields. For thick layers more than tens of nanometers thick, propagating SPs (SPR) are the proper choice. On the other hand, for very thin layers and small analytes, plasmonic sensors employing localized SPs on nanoparticles smaller than about 30 nm or sharp-tipped nanoparticles are the better choice.

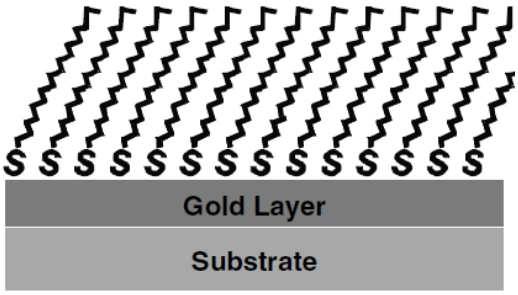

Figure 7. Scheme of n-dodecanethiolate self-assembled on gold surface. The assembly is held together by bonds between the sulfur head groups and the gold surface and van der Waals and hydrophobic interactions between neighboring hydrocarbon chains. From [11].

1.2.3 Applications

Although SPR sensors were at first applied for gas sensing [7], the main application fields for sensors based on SPR later became the detection of chemical and especially macromolecular biochemical analytes [12] for environmental monitoring and food safety and the analysis of the interactions of biological macromolecules [48]. The latter has become indispensable in the life sciences and pharmaceutical research.

Detection of several groups of analytes has been pursued with SPR biosensors, including fungal toxins [49], agricultural pesticide residues [50], hormones [51] and endocrine disruptors [52], nucleic acids including micro-RNAs [53-55], various proteins [56-58], viruses [59] and bacteria [60, 61].

The scope of applications of biosensors based on localized SPs (LSP resonance, LSPR) is similar to that of SPR biosensors. However, while SPR biosensors present an established technology with numerous important applications, the field of LSPR biosensors is much less mature and remains mostly in the proof-of-concept stage [30]. The difficulties of surface functionalization and fouling prevention are bigger compared to SPR biosensors, since LSPR biosensors present an inhomogeneous surface consisting of multiple materials (e.g. gold, glass) and complex geometries (e.g. sharp-tipped nanoparticles). Performing detection in real samples (e.g. blood serum) as opposed to buffers presents a challenge, as the detection limits in serum are often several orders of magnitude worse than in buffers [30].

1.2.4 Performance characteristics

There are several terms in the context of plasmonic biosensors related to the performance. Among the most important are [12]:

- Limit of detection (LoD) is defined as the analyte concentration that results in a

sensor output corresponding to 3 standard deviations of sensor output for a blank sample.

- Sensitivity is defined as the ratio of the change in sensor output (the wavelength or angle of the SP dip/peak) to the change in the quantity to be measured (e.g., concentration of analyte). Sensitivity depends on two factors: sensitivity of the sensor output to the refractive index at the sensor surface and efficiency of the conversion of the presence of analyte molecules in the liquid sample to a change in refractive index near the surface.
- Minimum resolvable surface coverage is the smallest increase in the mass of adsorbed molecules on the biosensor surface per unit area of the surface that results in a measurable increase in sensor output (related to the root-mean-square of the sensor output noise).

However, there are many more factors that influence biosensor performance and which contribute in a specific detection protocol to the resulting limit of detection. Various Figures of Merit (FoM) have been defined, taking into account various properties of the plasmonic structure or other parts of the biosensor system, for example:

- bandwidth of the spectral feature: narrower peak/dip allows higher precision in determining its position and lower noise of the sensor output,
- penetration depth of the plasmonic EM field: shallower depth is favourable for thin functional layers,
- dependence of spectra on angle of incidence: plasmonic structures with optical spectra mostly independent on the angle of incidence allow for illumination in a larger solid angle, resulting in larger photon flux and lower photon shot noise
- etc.

1.3 Numerical modelling of surface plasmons: FDTD

The chief method of solving electromagnetic problems used in this work is the Finite Differences in Time Domain (FDTD). FDTD solves Maxwell's equations directly by discretizing the electric & magnetic fields and the material properties on a rectangular grid (Figure 8) and advancing the discretized fields in time by means of the Maxwell's curl equations [62]. Both 2D and 3D formulations are available. Most other computational methods work in the frequency domain, but FDTD follows the time evolution of the fields (hence the name). The frequency dependence of required quantities is then obtained through discrete Fourier transform of their time dependence which is the immediate result of the simulation. Also, the cross-sections of absorption and scattering can be computed numerically through integration of the Poyinting vector over a surface surrounding the simulated object (e.g. a nanoparticle).

Simulations including surface plasmons present additional challenges over dielectric structures, since the spatial (and to retain stability also temporal) resolution needed is significantly higher for evanescent waves in metals than for free-space waves in dielectrics. The permittivity of metal also has to be modelled, e.g. by a Drude model, since FDTD is a time-domain method.

The method was first introduced by Yee in 1966 [63], however it became widely used only in the last two decades with the availability of sufficient computing power. The computation time scales linearly with the volume of the simulated domain, which is slower scaling than for many popular frequency-domain methods of solving plasmonic problems (Discrete Dipole Approximation [64], Finite Elements Method [65]). As computing power in-

creases, this type of scaling gives FDTD an increasing advantage. It can be therefore expected that FDTD will capture an increasing share of use in the future. On the other hand, an intrinsic disadvantage of FDTD as a time-domain method is that narrow spectral ranges cannot be computed separately, increasing the difficulty of simulating high-Q resonant structures.

In the current commercial implementations, the bottleneck of FDTD performance is usually the bandwidth of the memory subsystem (RAM). Since the CPU computations needed for updating a single point of the grid are rather simple, fetching the grid data to/from memory is the bottleneck. Computers have several levels of memory cache subsystems designed to alleviate memory bandwidth limitations, but present FDTD implementations have not taken advantage of the cache subsystems, essentially bypassing them altogether. Recent work by Zakirov et al. [66] has implemented an FDTD algorithm that updates a block of the whole domain small enough to fit within the cache for many timesteps followed by updating the neighbouring block and resolving the dependencies of the blocks. They showed that by taking advantage of the cache and memory hierarchy, the FDTD algorithm can run up to two orders of magnitude faster.

General Purpose Computation on Graphical Processing Units (GPGPU) has been advantageously applied in many numerical simulation fields, leveraging the huge investments and advances spearheaded by the 3D video game industry [67]. However, GPGPU has seen very slow adoption for FDTD despite the very high performance of the memory subsystem of 3D graphics cards. The much larger amount of system RAM, albeit slower, is usually more advantageous than the smaller amount of high-speed RAM on the graphics card. Being able to simulate larger domains of photonic devices within FDTD and without resorting to more approximate method has usually higher value than the speed provided by GPUs.

However, coupling the recent advance of exploiting the presence of memory cache with GPGPU, a system could be created where the fast and rather small RAM of the GPU would act as a cache of the system GPU, combining the advantages of both [66]. It can therefore be predicted that in the coming years, FDTD software surpassing the speed of the current commercial FDTD software by orders of magnitude could become reality.

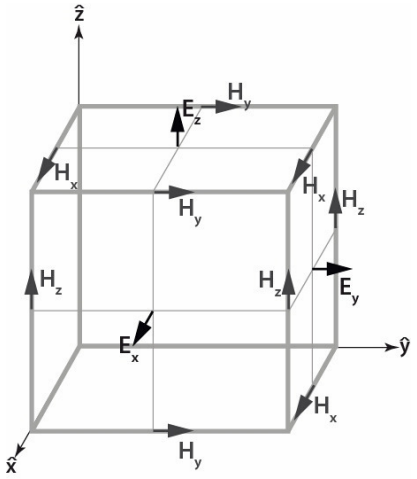

Figure 8. Yee cell, the discretization scheme for FDTD. It is chosen to facilitate the evaluation of the discretized Maxwell's curl equations by central differences. From [62].

2 Objectives

The aim of this thesis is to explore the potential of extending the surface plasmon biosensor technology towards the microscale and nanoscale, especially through confining high-performance plasmonic biosensing to microscopic areas and through exploring the utilization of plasmonic nanoparticles in biosensors. This work encompasses the following main types of activities:

- Theoretical analysis of plasmonic nanostrucutres, especially via computer modelling.
- Development of optical sensor platforms with miniaturized sensitive areas and platforms utilizing localized SPs on nanoparticles.
- Characterization and evaluation of the performance of the new platforms in model biosensing experiments.

3 Results

The presented thesis is based on works authored or co-authored by the thesis author during her Ph.D. studies. The individual journal papers are attached as Appendices I—VI and thesis author's contribution to them is described in the List of Appendices (pg. 33). The results achieved can be divided into three areas:

1. Propagating SPs confined to micrometer sized areas for biosensing – Appendices I, II, III.
2. Plasmonic nanoparticles for response enhancement in SPR biosensors – Appendix IV.
3. Biosensor based on localized SPs of gold nanoparticles on a solid substrate and the nanometer-scale localization of its sensitivity – Appendices V and VI.

A summary of the works is presented in the following three sections.

3.1 Propagating SPs confined to micrometer sized areas for biosensing

In biosensors, propagating SPs have been mostly used to probe surface areas on the order of square millimeters. For such state-of-the-art biosensors [68], the lowest detectable surface coverage (about 0.9 pg/mm^2) of the analyte corresponds to millions of biomolecules. Reducing the area probed by the propagating SP by several orders of magnitude can lower the number of analyte molecules needed to elicit biosensor response correspondingly. Prospectively, bringing the number down to a single molecule would open up new areas and applications for biosensors with propagating SPs. While such attempts have already been made [69], the miniaturization of the probed area has also resulted in a corresponding drop in signal-to-noise ratio, limiting the analytical performance of the biosensor. As a part of the effort towards the goal of "single molecule detection" without the loss in analytical performance, two approaches to confining biosensing with propagating SPs to micrometer sized areas have been developed and are presented below.

In order to miniaturize the area probed by the SPs down to the wave-optical limit, it is necessary to employ high-resolution optics, while still allowing for the coupling between incident/reflected light and propagating SPs on the gold surface. The approach available in literature achieves this dual goal by using a microscope objective of an extremely high numerical aperture, N.A. > 1.40 [70, 71]. The final lens of such an objective fulfills the same role as the coupling prism in the Kretschmann configuration (see Figure 2). However, extremely high N.A. objectives are impractical due to their extremely short working distance and depth of focus, limited field of view, the need for special immersion oils and high cost.

To overcome the disadvantages of using microscope objectives with extremely high N.A., two approaches have been developed. Both methods utilize an ordinary, medium-magnification microscope objective (N.A. = 0.65) and take advantage of the gold surface having a shallow sine relief grating whose depth is on the nanometer scale, which acts as the coupler between free-space light waves and propagating SPs on gold surface.

3.1.1 Single-wavelength multiple-angle approach

Appendix I describes the first method and the confinement achieved. A laser beam is focused on the gold surface, exciting SPs there and the reflected light is analyzed by a CCD camera (Figure 9, left). The experimental arrangement is thus an extension of one of the basic SPR arrangements, namely the "single wavelength-multiple angles" arrangement (Figure 6b) and is also optically similar to an epi-illuminated microscope. Coupling of the incident light into SPs is manifested in the cone of reflected light as a lack of light for certain angles of incidence. SPs are confined to the vicinity of the laser focus, where they are excited, by their limited propagation length along the lossy surface (~micrometers) and also by the interference of SP waves excited in a range of azimuth angles.

Specifically, a 750 nm laser beam is focused by a microscope objective (40x/0.65 N.A.) onto the gold surface having a sine relief grating (period 520 nm, depth 30 nm) into a diffraction-limited spot (about 0.9 um diameter). The relief has been prepared by means of UV interference lithography. The back focal plane of the objective is projected by another lens onto a CCD camera, since the spatial distribution of light in the back focal plane corresponds to the angular distribution of light reflected from the focus on the gold surface. In the angular distribution of the reflected light it is then possible to observe two dark arcs (Figure 9, left) that correspond to incident plane-wave components $\mathbf{k}_{||}$ that have coupled into SPs according to the coupling condition (Equation 4). The coupling condition extended to 3D is schematically presented in Figure 9 (middle). Propagating SPs are thus excited in a range of azimuthal angles centered along the grating wavevector, perpendicular to the grating lines.

The position and diameter of the dark arcs has been shown to change with the refractive index (RI) of the medium in contact with gold surface (air, water, photoresist).

To determine the actual level of confinement of SPs within the vicinity of the focus, we have presented the SPs with an obstacle in the form of a step change in the RI near the gold surface, i.e. a boundary between the part of the gold surface covered with a layer of dielectric material neighbouring an uncoated part of the gold surface. When the boundary is within the reach of SPs excited in the laser focus, the thickness of the dark arcs increases due to limited lifetime/propagation length available.

To produce such step change of RI on the gold surface, a simple optical microlithography system has been built. A mask has been projected using blue light by a 40x microscope objective onto a layer of positive photoresist spin-coated on the gold surface. After etching of the resist, several rectangular regions free of photoresist have been created on the gold surface (Figure 11, right, a).

Focusing the laser beam within an area where the photoresist has been removed, well-formed dark arcs corresponding to SPs on an gold-air interface have been recorded (labeled "SP-air" in Figure 9, right, b). When the focus has been closer to the boundary than 14 μm along the grating vector, or closer than 7 μm perpendicular to the grating vector, a change in pattern of dark arcs has been noted (Figure 9, right, a and c), which corresponds to the disturbance of the SP mode of the gold-air interface and to the presence of SP modes of the gold-photoresist interface (labeled "SP-resist") and a waveguide mode within the photoresist layer ("WG-resist"). The results suggest that the SPs have been successfully confined to an area no larger than 100 μm^2. Since the top and bottom dark arcs and left and right halves of the dark arcs reacted to step changes independently, SPs can be considered to be effectively confined to an area of about 25 μm^2.

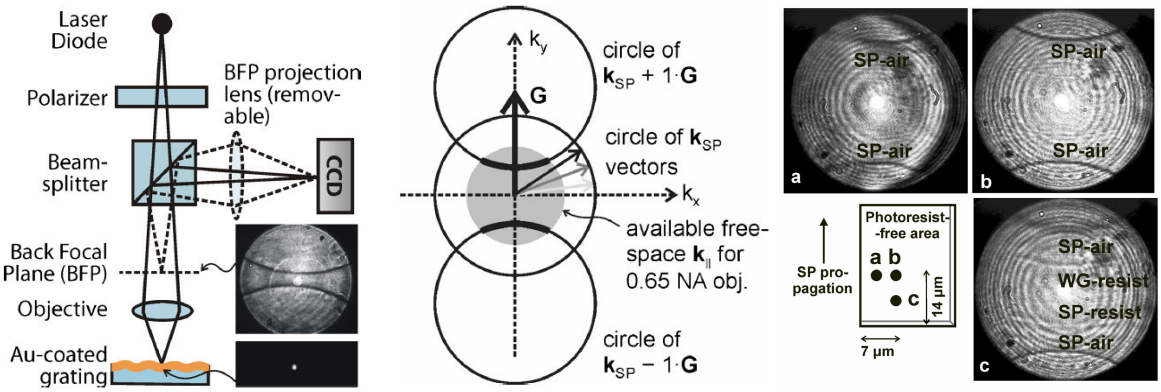

Figure 9. Left: Layout of the optical system for confined excitation of propagating SPs. *Top inset:* CCD image of the Back Focal Plane of the objective. *Bottom inset:* CCD image of the gold surface. **Middle:** Diagram of surface plasmon $\mathbf{k}_{SP}$ vectors and matching incident wave vector components $\mathbf{k}_{||} = (k_x, k_y)$ coupled via a diffraction grating with the vector **G**. **Right:** SP arcs observed when moving the focal point from the photoresist-free to photoresist-coated areas. Grating vector is vertical in the image. SP-air and SP-resist denote arcs corresponding to SPs on the gold–air and gold–photoresist interface, respectively. WG-resist denotes the arc for a waveguide mode propagating in the photoresist layer. In (c), the top three arcs correspond to WG and SP modes propagating downwards in the image and traversing the air–resist boundary; the bottom arc corresponds to an unperturbed SP mode propagating along the gold–air interface. The concentric fringes are due to interference within the coverslip gold–air gap.

3.1.2 Multiple-wavelength single-angle approach

In the second approach (presented in **Appendix II)**, after passing through a microscope objective, a broadband collimated beam illuminates ~1 mm^2 of the gold surface (as opposed to the focused laser beam of App I/3.1.1), exciting SPs on it and the reflected light passes through a small aperture to a spectrometer (Figure 10). This arrangement corresponds to the "multiple wavelength-single angle" basic SPR arrangement (Figure 6a) and optically resembles an epi-illuminated spectroscopic microscope. The angle of incidence of the collimated beam is selected per the coupling condition (equation 4). Coupling of the incident light into propagating SPs is manifested as a lack of reflected light for certain wavelengths.

The optical arrangement is depicted in Figure 10. The plane of the aperture is optically conjugated with the gold surface through the microscope objective. Only light reflected from the gold surface area that corresponds to the demagnified image of the aperture is analyzed. Therefore, it can be said that the confinement of SPs is "virtual" as opposed to "actual" confinement of section 3.1.1. However, the spatial extent of SP modes which contribute to the signal in the collected light (i.e. the sensitive area of a sensor based on this platform) is larger than the image of the aperture, just as it was larger than the laser focus in work described in the previous section. It should be noted that in contrast to that work (Appendix I), SPs are excited in a single azimuthal angle only in the propagating in a single direction only in this work (Appendix II).

To determine the level of confinement, a layer of photoresist on the gold surface with micrometer-scale photoresist-free areas (Figure 11, right, a) has been used (as described in 3.1.1) and the spectra of the reflected light have been recorded for different distances (along the grating vector) between the edge of the resist-free area and the edge of the aperture image on the gold surface (Figure 11, left). Similar measurement has been performed for various lateral distances. Towards the boundary of the photoresist layer, the dip in SPR wavelength spectrum gets wider and shallower, corresponding to a decrease in its life-

time/propagation length. (Similar changes were described in section 3.1.1 for the SPR angular spectrum.) According to these results, it can be said that only a surface area of about 60 μm^2 is influencing the plasmons whose outcoupled light is collected by the aperture.

Another way of visualizing and determining the confinement was achieved by replacing the light source with a laser diode and the collection aperture with a CCD camera, resulting in a "singlewavelength-single angle" arrangement with 2D imaging (usually called SPR imaging). The angle of incidence has been tuned to coincide with the SPR minimum for the gold-air interface. In the image (Figure 11, right, b) the resist-free area (gold-air) appears black, while the resist-covered area (gold-resist interface) appears black, except for areas close to the top boundary, where the length of the available resist-free gold-air interface was not sufficient to allow for a fully developed SP mode.

This second approach and platform have been selected for further work as a biosensor, in order to determine how many analyte (protein) molecules are necessary to produce a signal above the sensor's noise level.

First, the baseline noise of the sensor output (SPR wavelength vs. time) has been determined to be 0.3 pm (root-mean-square, at 3 s averaging time per datapoint). For comparison, the spectral half-width of the SPR dip in this arrangement is about 10 nm.

Second, the relation between protein surface concentration and resulting SPR wavelength shift has been calibrated using a biochemical system known to reproducibly create a monolayer of protein molecules. Since the protein monolayer has to be created in-situ, a microfluidic flow-cell system had to be developed. The flow-cell has the glass slide with gold surface for SP excitation as one of its walls and the other wall is a cover slip to allow the microscope objective to illuminate the gold surface on the inside of the cell. The cell is sealed by a vinyl gasket. The presence of the protein (streptavidin) monolayer (~34,000 molecules per μm^2, 3.4 ng/mm^2) resulted in a shift of 1.45 nm (Figure 12).

The detection limit of the presented platform in terms of surface coverage is thus about 0.7 pg/mm^2 (well comparable with state-of-the-art sensors with macroscopic sensitive surfaces [68]). At about 60 μm^2 of sensitive area, it corresponds to about 450 individual protein molecules at the detection limit, which represents an improvement of three orders of magnitude in comparison with state-of-the-art macroscopic SPR biosensors.

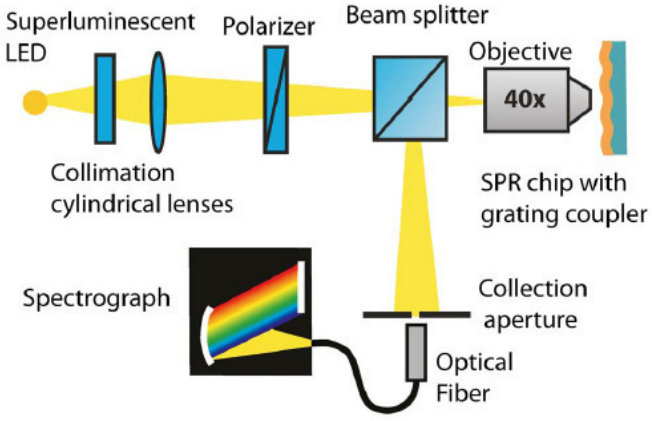

Figure 10. Optical setup of the SPR sensor with a minimized sensing area. Between the objective and the gold surface the beam is collimated (not shown). Optional microfluidic flow-cell is not shown.

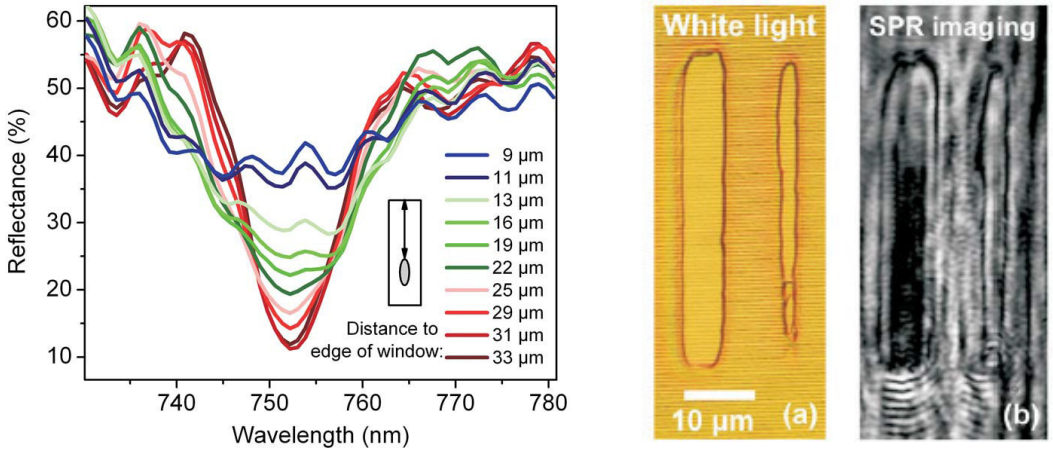

Figure 11. Left: Dependence of the shape of the SPR dip on the distance between the collection area and the edge of the resist-free window. **Right:** (a) Optical micrograph of the gold surface with a photoresist layer and resist-free windows of different sizes (the grating grooves are clearly visible). (b) SPR image of the resist-free windows. The dark color corresponds to the excitation of propagating SPs.

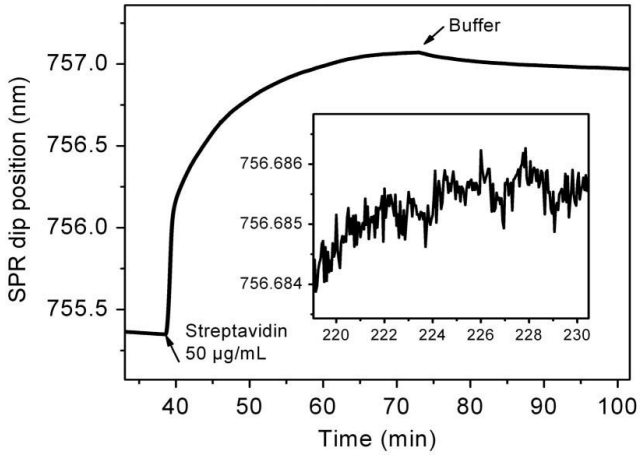

Figure 12. Temporal response of the SPR sensor to the formation of a streptavidin monolayer. Inset: baseline noise.

3.1.3 Detection of individual protein molecules through nanoparticle labels

In an effort to extend the detection capabilities of the biosensor platform (Figure 10) presented in previous section towards the goal of single-molecule detection, the SPR signal corresponding to the binding of individual molecules to the biosensor surface has been amplified by attaching spherical gold nanoparticles (Au NPs) of 30 nm diameter to the analyte already captured on the surface as labels (**Appendix III**).

For the model detection experiment, DNA hybridization detection assay was selected (Figure 13, left). A target DNA sequence TP53 (a part of a gene sequence with a key role in tumor suppression) in the solution binds to a DNA probe 1 immobilized on the surface. Then, DNA probe 2 terminated with biotin binds to the target DNA. Finally, 30 nm gold nanoparticle functionalized with streptavidin binds to probe 2 via streptavidin-biotin interaction.

The binding of Au NPs produced well-resolved steps (discontinuities) in the sensor output (the dependence of SPR wavelength vs. time), in relation to the baseline noise. Since NPs

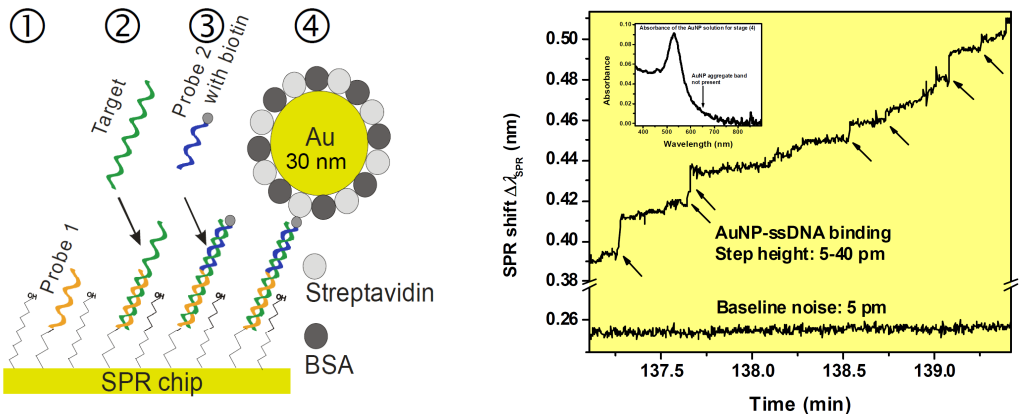

Figure 13. Left: Amplification scheme using functionalized AuNPs. The DNA target binds to DNA probe 1 (2); then DNA probe 2 terminated with biotin binds to the target (3); finally, AuNPs bind to probe 2 via the streptavidin-biotin interaction (4). **Right:** A segment of the sensor response to AuNPs (stage (4)) showing the steps corresponding to the binding of individual AuNP-labeled short ssDNA molecules. Inset: Absorbance of the AuNP solution showing that AuNPs are not aggregated.

have a tendency to aggregate, it was necessary to prove that the steps (discontinuities) did not correspond to NP aggregates, which could be orders of magnitude larger than individual NPs. This has been cross-checked through the following observations:

- Step rate (steps per minute) was proportional to Au NP solution concentration, proving that the steps were not due to unrelated surface processes.
- Absorption spectrum of the Au NP solution as measured before its injection into the flow-cell (inset in Figure 13, right) is a typical spectrum of non-aggregated solution. There isn't any appreciable contribution of aggregate spectra. Isolated NPs are thus the dominant species in the solution.
- Out of the total SPR wavelength shift achieved during Au NP solution's injection, about 80 % was the sum of individual steps, proving that the steps were due to the dominant species (isolated NPs per previous point) and not due to a minority species, such as a very low concentration of aggregates.

Thus, the sensor platform has been shown to be able to detect individual binding events between a surface bound DNA strand and a 30 nm Au NP as discrete steps in the sensor output curve well above the noise level.

It should be noted that the total SPR wavelength shift achieved during the assay is not dependent on the size of the sensitive area of the sensor and the same shift should be achieved by all SPR sensors working at the same wavelength and angle of incidence. It is the magnitude of the steps that increases with decreasing the sensitive area. Also, the number of steps per unit of time decreases with decreasing sensitive area.

The potential ability to resolve individual binding events without sacrificing performance in terms of minimum resolvable surface coverage has very promising consequences. For example, in traditional SPR biosensors, the minimum detectable analyte concentration is often determined by competition of the gradual SPR wavelength shift due to analyte binding with parasitic shifts due to various noise sources other than analyte binding (drift), including mechanical, chemical and electronic. Prolonging the measurement beyond the usual period (e.g. 10 minutes) is then of no help. However, when the binding results in discrete steps instead of in continuous change, the binding is then easily separated from many sources of noise. In the single-binding-event detection mode, much lower concentrations can in principle be detected, essentially limited only by the time available for the measurement (a sufficient number of steps would need to be registered to achieve a set level of

confidence about the presence of the analyte molecules in the sample liquid).

3.2 Plasmonic nanoparticles for response enhancement in SPR biosensors

In the previous sections it has been described how the sensor output (SPR wavelength shift) has been amplified by attaching gold nanoparticles to the bound analytes. Gold nanoparticles provide high signal enhancement relative to their size, thanks to the localized surface plasmon (localized SP, LSP) mode that can be excited in optical frequencies for nanoparticles in about 5—100 nm diameter range. However, the enhancement depends on nanoparticle size in a complex way. Previously published works regarding the size dependence provided ambiguous results. The work presented in **Appendix IV** has explored this dependence in detail, disentangling the contributing factors in order to guide in the future the proper selection of nanoparticles for response enhancement in SPR sensors.

The two main factors which influence the sensor response enhancement have been investigated: equilibrium surface density of NPs vs. NP size, and sensor response to unit NP surface density.

The optical sensor platform used for the work was in the "single angle-multiple wavelength" arrangement, with a prism coupler. Propagating SPs were excited on the gold-liquid interface by attenuated total reflection of light incident on the glass-gold interface (the Kretschmann configuration, Figure 2). Reflected light was analyzed with a spectrometer. The coupling resulted in a dip in the spectrum of the reflected light. SPs were excited over macroscopic areas of several mm^2 in four independent channels. A microfluidic flow-cell allowed flowing liquids along the gold surface.

In the model chemical assay (Figure 14, left, a), a sandwich of antibody 1-CEA-antibody 2 has been formed on the sensor surface (CEA – carcinoembryonic antigen, a protein). Au NPs of sizes between 10 and 52 nm then bound until saturation to antibody 2 through a chemical linker, with sparse coverage of the surface with antibody 2. The sensor response (SPR wavelength shift) for various sizes of NPs is shown in Figure 14, right.

In order to determine the surface density of NPs on a large number of SPR chips in a reproducible way, a semi-automated system of SEM imaging has been implemented using a Raith e_Line Plus instrument (a SEM/EBL system). After the operator registered the corners of the SPR chip and focused manually on them, the system automatically obtained a series of well-focused, high-resolution SEM images of 10×10 μm^2 areas from several positions on each of the spots corresponding to microfluidic channels of the SPR sensor system. After the transfer of the image data to a post-processing computer, the images were analyzed in batches using a software tool which has been implemented within the ImageJ image processing platform (*http://imagej.nih.gov/ij/*) to yield average particle counts per μm^2.

The surface density of NPs drops quickly with NP diameter (Figure 15, left). It has been hypothesized that it could be caused by multiple small NPs binding to a single antibody on the one hand, and large NPs not being able to bind to antibodies whose linker molecule had a sub-optimal position on the antibody.

Using the knowledge of equilibrium NP surface density (as a function of NP diameter), it was possible to calculate the sensor response per unit NP surface density (Figure 16), showing a response proportional to NP volume, as intuitively expected. To support the argument, a closed form equation has been developed. NP optical properties (LSPs) have been approximated with electrostatic approximation and the layer of nanoparticles has been modeled as a medium of a homogeneous refractive index (the effective medium the-

ory). Finally, the electric field depth profile of the propagating SP have been taken into account using the perturbation theory. The resulting formula is

$$S_\sigma \approx d_g{}^3 \frac{S_b n_m}{L_{pd}} \mathrm{Re}\left\{\frac{(\varepsilon_g - \varepsilon_m)}{6\varepsilon_m + 2(\varepsilon_g - \varepsilon_m)}\right\} \quad (6)$$

where S_σ is the sensor response per unit NP coverage, d_g is the diameter of the gold NP, S_b is the sensor sensitivity to a unit change in the bulk refractive index of the medium, n_m is the refractive index of the medium (liquid), L_{pd} is the penetration depth of the propagating SP, ε_g and ε_m are the complex permittivities of the gold and liquid medium, respectively. The graph comparing the theoretical prediction of eq. 6 with the measured values is shown in Figure 16 (dashed line), showing good agreement. The full line in Figure 16 represents a numerical calculation done with a less simplified approximation similar to eq. 6, demonstrating the correctness of the approach.

In conclusion, two opposing trends contributing to the response amplification capabilities of spherical NPs of different sizes have been identified, offering an explanation to previously published ambiguous results.

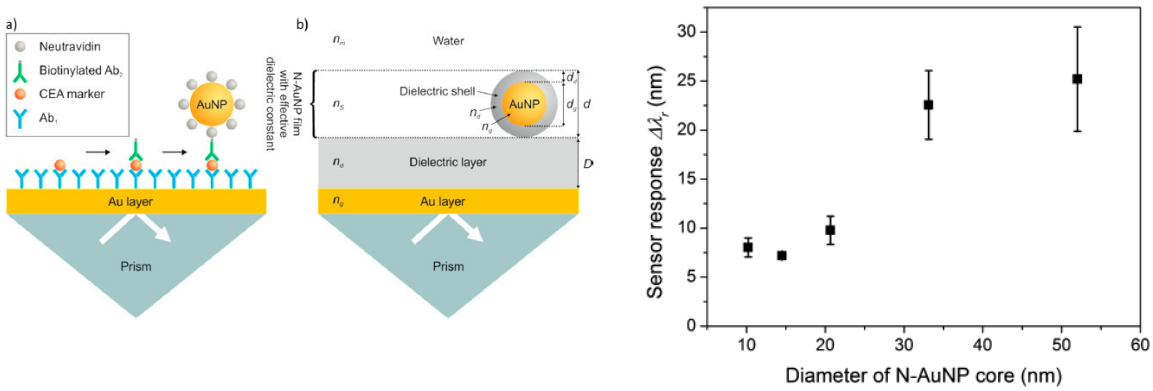

Figure 14. Left: (a) Scheme of the experiment: sandwich assay for the AuNP-enhanced detection of CEA. (b) Theoretical representation−multilayer structure described by multiple refractive indexes (n_g, n_d, n_S, n_m) and thicknesses of the layers (D, d). **Right:** Sensor responses, $\Delta\lambda_r$, for AuNPs with diameters of the gold core of 10, 15, 21, 33, and 52 nm. Errors were calculated as the standard deviation from at least three measurements regarding different SPR chips.

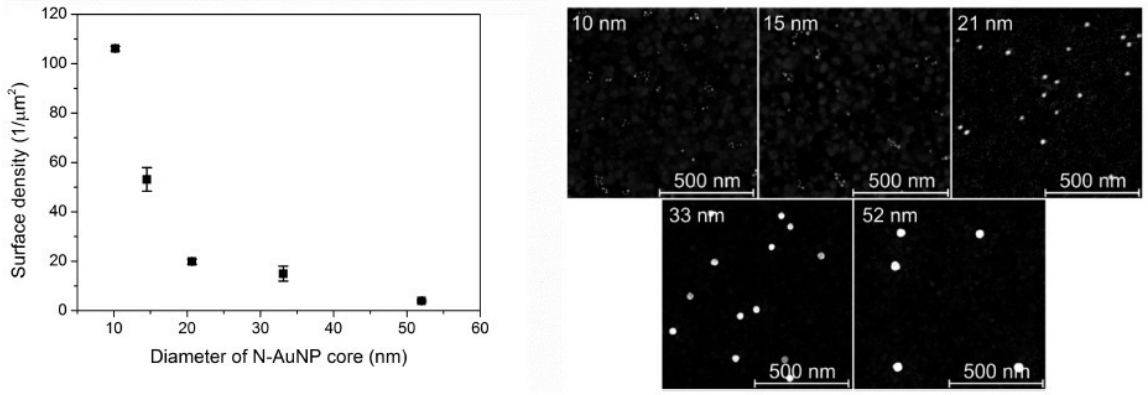

Figure 15. Left: Surface densities obtained for five different AuNP sizes. Errors were calculated as the standard deviation from three different chips, where five spots were measured across each chip. **Right:** SEM images of the surface of an SPR chip with AuNPs of different sizes.

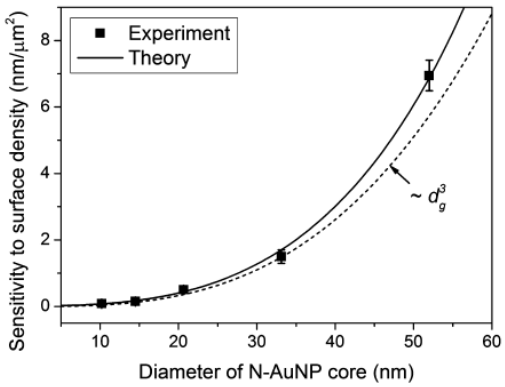

Figure 16. Theoretical (calculated using eq. 6) and experimental sensor sensitivity to surface density as a function of AuNP size. The dotted line represents a cubic dependence of sensitivity on the AuNP diameter calculated by the simplified model using eq. 6. The error bars are the propagated standard deviation from the results shown in Figures 14 and 15.

3.3 Biosensor based on localized SPs of nanoparticles on a solid substrate and the nanometer-scale localization of its sensitivity

In the previous section, gold NPs had been used as a response-enhancing agent for biosensors based on observing changes in properties of propagating SPs on thin gold layers. However, gold NPs on solid substrates can also be employed as the core of the biosensor's transducer in place of the thin gold layer. Changes in the frequency of the localized SP band of the NPs can then be used to infer on analyte binding near the surface of the NPs in a similar manner.

There are several potential advantages that can be expected from a NP-based (LSP-based) biosensor. The penetration depth of the EM field (within which biomolecular binding is monitored) of the localized SP mode into the surrounding liquid is about an order of magnitude shorter in comparison with propagating SPs. While an antibody as the typical biorecognition element is less than 15-20 nm large, the penetration depth of propagating SPs on gold in near-infrared is about 200-400 nm, thus diluting the response to antibody-analyte binding with a large dead volume and decreasing the biosensor performance. Shorter penetration depth of localized SPs on nanoparticles is better suited for monitoring binding events within such thin functional layers.

While biosensors based on LSPs had been demonstrated and shown to be able to detect low numbers of molecules, their analytical performance in terms of limits of detection has been rather limited. This work focused on demonstrating that analytical performance equal to or better than established biosensors based on propagating SPs is possible for biosensors based on localized SPs.

To guide the optimization of the geometrical parameters of the nanorods and of the nanorod array, a computational model has been prepared using the Finite Differences in Time Domain (FDTD) method, employing a commercial software package (Lumerical Solutions, Inc., Canada). A 12-node compute cluster has been built for this purpose. The results of the model and their comparison with experimentally obtained optical spectra are shown in Figure 18.

As noted in 1.3, the bottleneck for the FDTD algorithm is nowadays usually the memory subsystem of the computer. In case of computation on multiple nodes connected by a net-

work, it was observed that the network transfer speed became the bottleneck. Therefore, the 12-node compute cluster has been equipped with high-speed Infiniband DDR network interconnects, which provided up to twenty times the throughput of common LAN interconnects.

After optimizing the dimensions of the nanorods and the nanorod array with respect to the contrast of the localized SP band and to minimizing its bandwidth, arrays of gold nanorods (40 × 110 nm, 30 nm thickness) were fabricated on transparent substrates using electron beam lithography (EBL). In the optical platform, quasi-monochromatic light was used to illuminate the substrate with nanorods, which were attached to an optical prism and the incident beam underwent attenuated total reflection (ATR) (Figure 17). While ATR is not necessary for the excitation of localized SPs, this arrangement was selected to allow for a straightforward comparison with a biosensor system built on the same optical platform but utilizing propagating SPs on a thin gold layer [68]. The reflected light was projected onto a CCD camera. In order to increase the sensor sensitivity, phase change of the reflected light was taken into account as well as intensity, by means of a linear polarizer in front of the prism and an quarter-wave waveplate and another linear polarizer in front of the camera.

In the model detection experiment short oligonucleotides (targets) were detected via complementary oligonucleotides (probes) immobilized on the sensor surface. Target concentrations ranging from 100 nM down to 500 pM have been used. The resulting temporal response of the biosensor is shown in Figure 19, with even the lowest concentration resulting in clearly discernible response. Based on the sensor's baseline noise, a limit of detection of 200 pM has been extrapolated. This is comparable to high-performance SPR biosensors based on propagating SPs, with limits of detection of the order of nM or 100 pM [68].

The limit of detection in terms of surface coverage has been determined to be 35 fg/mm^2, which is much lower than that of 910 fg/mm^2 for state-of-the-art biosensor with propagating SPs. The difference lies mainly in the low fraction of the surface represented by the gold nanorods on their dielectric substrate and the shallower penetration depth of localized SPs. If the detection were of an analyte for which the diffusion of molecules from the sample bulk to the surface would be the limiting factor (e.g. large proteins) instead of the at-surface binding rate, then even the limit of detection in terms of analyte concentration would be probably be lower for the presented LSP-based sensor.

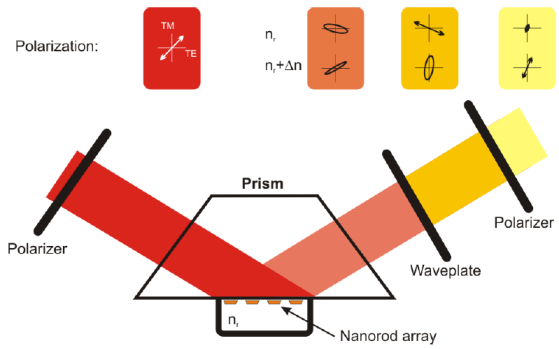

Figure 17. The schematic of the optical arrangement of the optical sensor based on the excitation of LSPs on an array of gold nanorods by the total internal reflection and polarization contrast (bottom) and the state of polarization of light in different sections of the optical path for two different values of the refractive index in the vicinity of the gold nanorods (top).

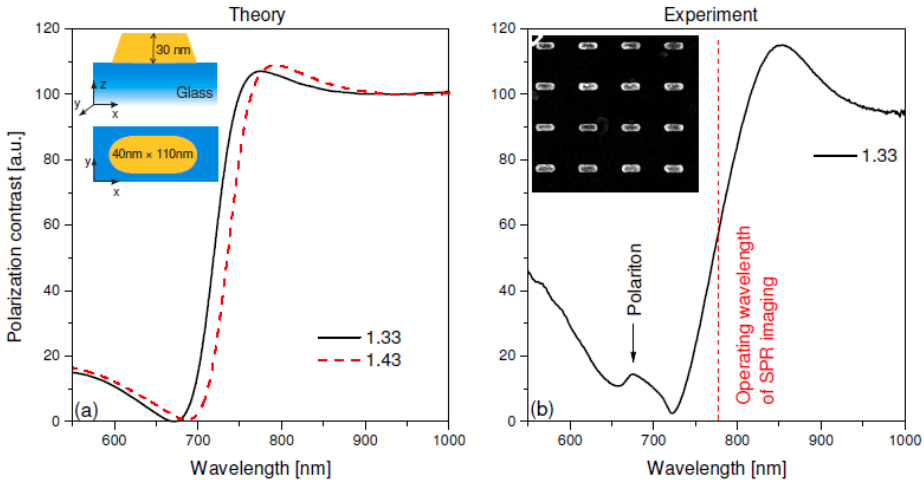

Figure 18. Wavelength spectrum of the light intensity in polarization contrast configuration. (a) Calculated spectra based on the FDTD model and (b) measured spectra of the fabricated nanorod array.

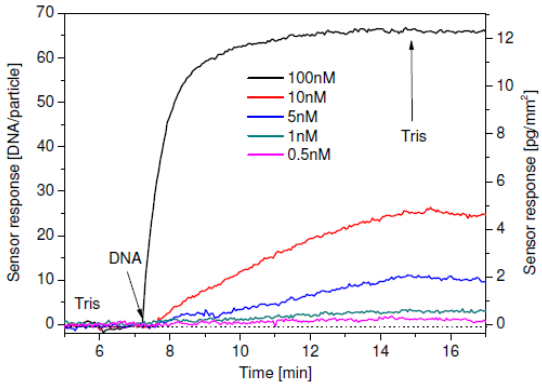

Figure 19. Temporal response of the LSP-based sensor to five different concentrations of target oligonucleotides.

The electric field of nonspherical metallic nanoparticles is highly localized on their tips, contrasting with the uniform electric field of propagating SPs on planar metal layers. It has been theorized that majority of the biosensor response (LSP wavelength shift) would originate from molecules binding in the areas of high local electric field. We have verified this assumption both computationally using FDTD and experimentally **(Appendix VI)**. For the experiment, an additional EBL manufacturing step has been added to the nanorod fabrication procedure, resulting in strip masks of polymer dielectric (PMMA) running perpendicular to the nanorod axes and covering various parts of the nanorods and playing the role of analyte molecules adsorbed on the respective parts of the nanorods. The extinction spectra of the resulting structures have been recorded and compared with the results of the FDTD model (Figure 20), showing good agreement in the wavelength of the LSP resonance and its shift with the polymer strips present. It is clearly visible that dielectric masks covering the centers of the nanorods elicited a lower response than masks covering the tips of the nanorods. Based on the LSP wavelength shifts corresponding to masks of various widths, a profile of differential sensitivity has been deconvoluted out of the data (Figure 21), confirming the hypothesis of refractometric sensitivity being highly localized on the nanorod tips.

It can be thus be assumed that if only the tips of the nanorods were made available to analyte binding, then even better limits of detection could be achieved for the detection of analytes whose binding to the surface is limited by diffusion from the bulk of the liquid.

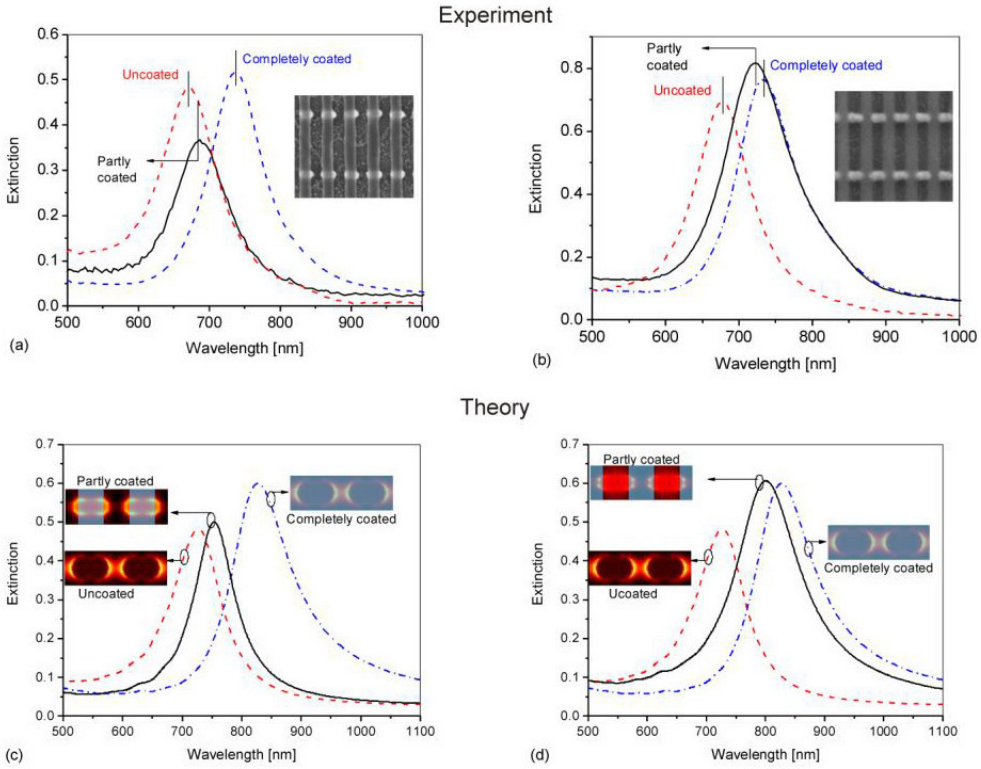

Figure 20. Extinction spectra of the nanostructure coated with PMMA masks at different positions (solid black curve). Experimental results are plotted in (a) for a 45 nm wide center mask and (b) for a 60 nm wide gap mask; SEM images of the respective configurations are attached. Results of FDTD simulations are plotted in (c) for a 50 nm wide center mask (d) for a 50 nm wide gap mask.

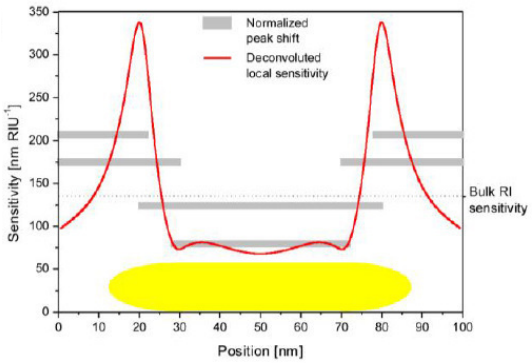

Figure 21. Local sensitivity as deduced experimentally using the mask method. Measured LSP peak shifts are plotted as grey horizontal bars – their horizontal position indicates the mask overlap with the nanoparticle and their vertical position indicates the peak shift normalized to mask width and RI; the average (bulk) sensitivity to bulk RI is indicated. The deconvoluted distribution of the sensitivity is plotted as the solid line for one period of the nanoparticle array. The nanoparticle is visualized in the graph for reference.

4 Conclusions

In this thesis, several research efforts related to extending the surface plasmon resonance biosensor technology towards the microscale and nanoscale are presented. New optical biosensor platforms based on propagating SPs, localized SPs, or both have been developed and their development involved both theoretical and experimental work. The platforms have been characterized and tested in model biosensing experiments and the interaction of propagating and localized SPs in a biosensor has been elucidated.

In the first part of the research, we have pursued the miniaturization of the sensitive area of biosensors based on propagating SPs (SPR biosensors) while retaining high analytical performance. Two optical platforms have been devised for this purpose, based on exciting SPs with the help of structuring the sensing surface into a shallow sine grating and employing a 40× microscope objective. Reduction of the sensitive area through both actual and virtual confinement has been experimentally verified and determined to be about 60 μm^2. At the same time, a minimum resolvable surface coverage of 0.7 pg/mm^2 has been achieved, comparable to the state-of-the-art laboratory SPR biosensors. The smallest measurable response is produced by about 450 protein molecules, representing a reduction of three orders of magnitude. By amplifying the sensor response to analyte binding with gold nanoparticles, detection of individual binding events has been achieved well above the noise floor.

In the second part of the research, the dependence of the size of gold nanoparticles (NPs) used for enhancing the SPR biosensor response has been explored in light of ambiguous previously published results. The magnitude of enhancement has been broken down into two factors with opposite dependences on NP size. The sensor response to a unit surface density of NPs has been shown theoretically and experimentally to be proportional to the NP volume. The maximum surface density of NPs binding to biotinylated antibodies decreases with the NP size due to steric effects. Rational selection of an appropriate size of the NPs for sensor response enhancement has thus been facilitated.

In the third part, a biosensor based on localized SPs on gold nanorods (LSPR biosensor) has been developed. The nanostructure has been optimized through FDTD calculations and fabricated on a transparent substrate using electron beam lithography. It has been shown to be able to detect a concentration of a model analyte, an oligonucleotide, of 200 pM, comparable with state-of-the-art SPR biosensors, while being able to resolve a surface coverage more than an order of magnitude lower (35 vs. 910 fg/mm^2), promising enhanced performance for larger analytes. The sensitivity of the nanorods has been shown both theoretically and experimentally to be co-localized with the electric field of the localized SP at the tips of the nanorods tips.

These works demonstrate that extending the technology of biosensors based on surface plasmons towards the microscale and nanoscale can bring increased performance and promising new capabilities.

5 List of Abbreviations

ATR	Attenuated Total Reflection
BFP	Back Focal Plane
BSA	Bovine Serum Albumin
CCD	Charge Coupled Device
DNA	Deoxyribonucleic Acid
EBL	Electron Beam Lithography
FDTD	Finite Differences in Time Domain
LED	Light-Emitting Diode
LoD	Limit of Detection
LSP	Localized Surface Plasmon
LSPR	Localized Surface Plasmon Resonance
N.A.	Numerical Aperture
NP	Nanoparticle
Obj.	Objective
PMMA	Poly(methyl methacrylate)
PSP	Propagating Surface Plasmon
RI	Refractive Index
RNA	Ribonucleic acid
S/N	Signal-to-noise
SEM	Scanning Electron Microscope
SERS	Surface-enhanced Raman Scattering
SLED	Superluminescent Light-Emitting Diode
SP	Surface Plasmon
SPR	Surface Plasmon Resonance

6 Bibliography

[1] R. W. Wood, "On a Remarkable Case of Uneven Distribution of Light in a Diffraction Grating Spectrum," *Proceedings of the Physical Society of London*, vol. 18, p. 269, 1902.

[2] U. Fano, "The Theory of Anomalous Diffraction Gratings and of Quasi-Stationary Waves on Metallic Surfaces (Sommerfeld's Waves," *Journal of the Optical Society of America*, vol. 31, pp. 213–222, 1941.

[3] R. H. Ritchie, "Plasma Losses by Fast Electrons in Thin Films," *Physical Review*, vol. 106, pp. 874–881, 1957.

[4] A. Otto, "Excitation of nonradiative surface plasma waves in silver by the method of frustrated total reflection," *Zeitschrift für Physik*, vol. 216, no. 4, pp. 398–410, 1968.

[5] E. Kretschmann and H. Raether, "Radiative decay of non radiative surface plasmons excited by light," *Zeitschrift für Naturforschung A*, vol. 23, no. 12, pp. 2135–2136, 1968.

[6] H. Raether, "Surface plasmons on smooth surfaces," in *Surface plasmons on smooth and rough surfaces and on gratings*, Springer, 1988, pp. 4–39.

[7] B. Liedberg, C. Nylander, and I. Lunström, "Surface plasmon resonance for gas detection and biosensing," *Sensors and actuators*, vol. 4, pp. 299–304, 1983.

[8] P. L. Stiles, J. A. Dieringer, N. C. Shah, and R. P. Van Duyne, "Surface-enhanced Raman spectroscopy," *Annu. Rev. Anal. Chem.*, vol. 1, pp. 601–626, 2008.

[9] X. Zhang and Z. Liu, "Superlenses to overcome the diffraction limit," *Nature materials*, vol. 7, no. 6, p. 435, 2008.

[10] K. R. Catchpole and A. Polman, "Plasmonic solar cells," *Optics express*, vol. 16, no. 26, pp. 21793–21800, 2008.

[11] M. Piliarik, H. Vaisocherová, and J. Homola, "Surface Plasmon Resonance Biosensing," in *Biosensors and Biodetection*, Humana Press, 2009, pp. 65–88.

[12] J. Homola, "Surface plasmon resonance sensors for detection of chemical and biological species," *Chemical reviews*, vol. 108, no. 2, pp. 462–493, 2008.

[13] C. F. Bohren and D. R. Huffman, *Absorption and scattering of light by small particles*. Weinheim: Wiley-VCH, 2004.

[14] M. Fleischmann, P. J. Hendra, and A. J. McQuillan, "Raman spectra of pyridine adsorbed at a silver electrode," *Chemical Physics Letters*, vol. 26, no. 2, pp. 163–166, 1974.

[15] D. L. Jeanmaire and R. P. Van Duyne, "Surface Raman spectroelectrochemistry: Part I. Heterocyclic, aromatic, and aliphatic amines adsorbed on the anodized silver electrode," *Journal of Electroanalytical Chemistry and Interfacial Electrochemistry*, vol. 84, no. 1, pp. 1–20, 1977.

[16] A. Biswas, I. S. Bayer, A. S. Biris, T. Wang, E. Dervishi, and F. Faupel, "Advances in top–down and bottom–up surface nanofabrication: Techniques, applications & future prospects," *Advances in colloid and interface science*, vol. 170, no. 1, pp. 2–27, 2012.

[17] M. R. Jones, K. D. Osberg, R. J. Macfarlane, M. R. Langille, and C. A. Mirkin, "Templated techniques for the synthesis and assembly of plasmonic nanostructures," *Chemical Reviews*, vol. 111, no. 6, pp. 3736–3827, 2011.

[18] H.-D. Yu, M. D. Regulacio, E. Ye, and M.-Y. Han, "Chemical routes to top-down nanofabrication," *Chemical Society Reviews*, vol. 42, no. 14, pp. 6006–6018, 2013.

[19] N. Guillot and M. L. de la Chapelle, "Lithographied nanostructures as nanosensors," *Journal of Nanophotonics*, vol. 6, no. 1, pp. 064506–1, 2012.

[20] T. V. Shahbazyan and M. I. Stockman, *Plasmonics: theory and applications*. New York: Springer, 2013.

[21] K. M. Mayer and J. H. Hafner, "Localized surface plasmon resonance sensors," *Chemical reviews*, vol. 111, no. 6, pp. 3828–3857, 2011.
[22] M.-C. Estevez, M. A. Otte, B. Sepulveda, and L. M. Lechuga, "Trends and challenges of refractometric nanoplasmonic biosensors: a review," *Analytica chimica acta*, vol. 806, pp. 55–73, 2014.
[23] E. Petryayeva and U. J. Krull, "Localized surface plasmon resonance: nanostructures, bioassays and biosensing—a review," *Analytica chimica acta*, vol. 706, no. 1, pp. 8–24, 2011.
[24] A. G. Brolo, "Plasmonics for future biosensors," *Nature Photonics*, vol. 6, no. 11, pp. 709–713, 2012.
[25] A. B. Dahlin, "Sensing applications based on plasmonic nanopores: The hole story," *Analyst*, vol. 140, no. 14, pp. 4748–4759, 2015.
[26] O. Kedem, A. Vaskevich, and I. Rubinstein, "Critical issues in localized plasmon sensing," *The Journal of Physical Chemistry C*, vol. 118, no. 16, pp. 8227–8244, 2014.
[27] B. Sepúlveda, P. C. Angelomé, L. M. Lechuga, and L. M. Liz-Marzán, "LSPR-based nanobiosensors," *Nano Today*, vol. 4, no. 3, pp. 244–251, 2009.
[28] S. Szunerits and R. Boukherroub, "Sensing using localised surface plasmon resonance sensors," *Chemical Communications*, vol. 48, no. 72, pp. 8999–9010, 2012.
[29] M. I. Stockman, "Nanoplasmonic sensing and detection," *Science*, vol. 348, no. 6232, pp. 287–288, 2015.
[30] B. Špačková, P. Wrobel, M. Bocková, and J. Homola, "Optical biosensors based on plasmonic nanostructures: a review," *Proceedings of the IEEE*, vol. 104, no. 12, pp. 2380–2408, 2016.
[31] E. Kretschmann and H. Raether, "Radiative decay of non radiative surface plasmons excited by light," *Zeitschrift für Naturforschung A*, vol. 23, no. 12, pp. 2135–2136, 1968.
[32] A. Rasooly and K. E. Herold, Eds., *Biosensors and biodetection: methods and protocols*. New York, NY: Humana Press, 2009.
[33] K. L. Kelly, E. Coronado, L. L. Zhao, and G. C. Schatz, *The optical properties of metal nanoparticles: the influence of size, shape, and dielectric environment*. ACS Publications, 2003.
[34] K. Saha, S. S. Agasti, C. Kim, X. Li, and V. M. Rotello, "Gold nanoparticles in chemical and biological sensing," *Chemical reviews*, vol. 112, no. 5, pp. 2739–2779, 2012.
[35] S. Zeng, K.-T. Yong, I. Roy, X.-Q. Dinh, X. Yu, and F. Luan, "A review on functionalized gold nanoparticles for biosensing applications," *Plasmonics*, vol. 6, no. 3, p. 491, 2011.
[36] L. Huang *et al.*, "Prostate-specific antigen immunosensing based on mixed self-assembled monolayers, camel antibodies and colloidal gold enhanced sandwich assays," *Biosensors and bioelectronics*, vol. 21, no. 3, pp. 483–490, 2005.
[37] T. Špringer and J. Homola, "Biofunctionalized gold nanoparticles for SPR-biosensor-based detection of CEA in blood plasma," *Analytical and bioanalytical chemistry*, vol. 404, no. 10, pp. 2869–2875, 2012.
[38] I. Ament, J. Prasad, A. Henkel, S. Schmachtel, and C. Sönnichsen, "Single unlabeled protein detection on individual plasmonic nanoparticles," *Nano letters*, vol. 12, no. 2, pp. 1092–1095, 2012.
[39] L. S. Live *et al.*, "Angle-dependent resonance of localized and propagating surface plasmons in microhole arrays for enhanced biosensing," *Analytical and bioanalytical chemistry*, vol. 404, no. 10, pp. 2859–2868, 2012.
[40] B. Špačková, P. Lebrušková, H. Šípová, P. Kwiecien, I. Richter, and J. Homola, "Ambiguous refractive index sensitivity of fano resonance on an array of gold nanoparti-

cles," *Plasmonics*, vol. 9, no. 4, pp. 729–735, 2014.
[41] S. Kumar, N. J. Wittenberg, and S.-H. Oh, "Nanopore-induced spontaneous concentration for optofluidic sensing and particle assembly," *Analytical chemistry*, vol. 85, no. 2, pp. 971–977, 2012.
[42] S. K. Dondapati, T. K. Sau, C. Hrelescu, T. A. Klar, F. D. Stefani, and J. Feldmann, "Label-free biosensing based on single gold nanostars as plasmonic transducers," *Acs Nano*, vol. 4, no. 11, pp. 6318–6322, 2010.
[43] H. Vaisocherova *et al.*, "Ultralow fouling and functionalizable surface chemistry based on a zwitterionic polymer enabling sensitive and specific protein detection in undiluted blood plasma," *Analytical chemistry*, vol. 80, no. 20, pp. 7894–7901, 2008.
[44] C. Rodriguez Emmenegger, E. Brynda, T. Riedel, Z. Sedlakova, M. Houska, and A. B. Alles, "Interaction of blood plasma with antifouling surfaces," *Langmuir*, vol. 25, no. 11, pp. 6328–6333, 2009.
[45] M. Piliarik, H. Šípová, P. Kvasnička, N. Galler, J. R. Krenn, and J. Homola, "High-resolution biosensor based on localized surface plasmons," *Opt. Express, OE*, vol. 20, no. 1, pp. 672–680, Jan. 2012.
[46] J. Y. Lin, A. D. Stuparu, M. D. Huntington, M. Mrksich, and T. W. Odom, "Nanopatterned substrates increase surface sensitivity for real-time biosensing," *The Journal of Physical Chemistry C*, vol. 117, no. 10, pp. 5286–5292, 2013.
[47] J. Ferreira *et al.*, "Attomolar protein detection using in-hole surface plasmon resonance," *Journal of the American Chemical Society*, vol. 131, no. 2, pp. 436–437, 2008.
[48] R. Karlsson, "SPR for molecular interaction analysis: a review of emerging application areas," *Journal of Molecular Recognition*, vol. 17, no. 3, pp. 151–161, 2004.
[49] S. J. Daly *et al.*, "Development of surface plasmon resonance-based immunoassay for aflatoxin B1," *Journal of Agricultural and Food Chemistry*, vol. 48, no. 11, pp. 5097–5104, 2000.
[50] E. Mauriz, A. Calle, J. J. Manclus, A. Montoya, and L. M. Lechuga, "Multi-analyte SPR immunoassays for environmental biosensing of pesticides," *Analytical and bioanalytical chemistry*, vol. 387, no. 4, pp. 1449–1458, 2007.
[51] J. W. Chung, R. Bernhardt, and J. C. Pyun, "Sequential analysis of multiple analytes using a surface plasmon resonance (SPR) biosensor," *Journal of immunological methods*, vol. 311, no. 1, pp. 178–188, 2006.
[52] K. Hegnerová, M. Piliarik, M. Šteinbachová, Z. Flegelová, H. Černohorská, and J. Homola, "Detection of bisphenol A using a novel surface plasmon resonance biosensor," *Analytical and bioanalytical chemistry*, vol. 398, no. 5, pp. 1963–1966, 2010.
[53] B. P. Nelson, M. R. Liles, K. B. Frederick, R. M. Corn, and R. M. Goodman, "Label-free detection of 16S ribosomal RNA hybridization on reusable DNA arrays using surface plasmon resonance imaging," *Environmental microbiology*, vol. 4, no. 11, pp. 735–743, 2002.
[54] T. T. Goodrich, H. J. Lee, and R. M. Corn, "Enzymatically amplified surface plasmon resonance imaging method using RNase H and RNA microarrays for the ultrasensitive detection of nucleic acids," *Analytical chemistry*, vol. 76, no. 21, pp. 6173–6178, 2004.
[55] H. Šípová, S. Zhang, A. M. Dudley, D. Galas, K. Wang, and J. Homola, "Surface plasmon resonance biosensor for rapid label-free detection of microribonucleic acid at subfemtomole level," *Analytical chemistry*, vol. 82, no. 24, pp. 10110–10115, 2010.
[56] C. Wittekindt, B. Fleckenstein, K.-H. Wiesmüller, B. R. Eing, and J. E. Kühn, "Detection of human serum antibodies against type-specifically reactive peptides from the N-terminus of glycoprotein B of herpes simplex virus type 1 and type 2 by surface plasmon resonance," *Journal of virological methods*, vol. 87, no. 1, pp. 133–144, 2000.

[57] H. Vaisocherova, K. Mrkvová, M. Piliarik, P. Jinoch, M. Šteinbachová, and J. Homola, “Surface plasmon resonance biosensor for direct detection of antibody against Epstein-Barr virus,” *Biosensors and Bioelectronics*, vol. 22, no. 6, pp. 1020–1026, 2007.
[58] M. H. Meyer, M. Hartmann, and M. Keusgen, “SPR-based immunosensor for the CRP detection—A new method to detect a well known protein,” *Biosensors and Bioelectronics*, vol. 21, no. 10, pp. 1987–1990, 2006.
[59] C. Zeng *et al.*, “Rapid and sensitive detection of maize chlorotic mottle virus using surface plasmon resonance-based biosensor,” *Analytical biochemistry*, vol. 440, no. 1, pp. 18–22, 2013.
[60] H. Baccar, M. B. Mejri, I. Hafaiedh, T. Ktari, M. Aouni, and A. Abdelghani, “Surface plasmon resonance immunosensor for bacteria detection,” *Talanta*, vol. 82, no. 2, pp. 810–814, 2010.
[61] M. Vala, S. Etheridge, J. A. Roach, and J. Homola, “Long-range surface plasmons for sensitive detection of bacterial analytes,” *Sensors and Actuators B: Chemical*, vol. 139, no. 1, pp. 59–63, 2009.
[62] A. Taflove and S. C. Hagness, *Computational electrodynamics: the finite-difference time-domain method*, 3rd ed. Boston: Artech House, 2005.
[63] K. Yee, “Numerical solution of initial boundary value problems involving Maxwell’s equations in isotropic media,” *IEEE Transactions on antennas and propagation*, vol. 14, no. 3, pp. 302–307, 1966.
[64] B. T. Draine and P. J. Flatau, “Discrete-dipole approximation for scattering calculations,” *JOSA A*, vol. 11, no. 4, pp. 1491–1499, 1994.
[65] S. Burger, L. Zschiedrich, J. Pomplun, and F. Schmidt, “Finite element method for accurate 3D simulation of plasmonic waveguides,” 2010, p. 76040F.
[66] A. V. Zakirov, V. D. Levchenko, A. Y. Perepelkina, and Y. Zempo, “High performance FDTD code implementation for GPGPU supercomputers,” *Препринты Института прикладной математики им. МВ Келдыша РАН*, no. 0, pp. 44–22, 2016.
[67] Y. Cai and S. See, *GPU Computing and Applications*. Singapore ; s.l.: Springer Singapore : Imprint: Springer, 2015.
[68] H. Vaisocherová *et al.*, “Investigating oligonucleotide hybridization at subnanomolar level by surface plasmon resonance biosensor method,” *Biopolymers*, vol. 82, no. 4, pp. 394–398, 2006.
[69] K. M. Mayer, F. Hao, S. Lee, P. Nordlander, and J. H. Hafner, “A single molecule immunoassay by localized surface plasmon resonance,” *Nanotechnology*, vol. 21, no. 25, p. 255503, 2010.
[70] K. Watanabe, N. Horiguchi, and H. Kano, “Optimized measurement probe of the localized surface plasmon microscope by using radially polarized illumination,” *Applied optics*, vol. 46, no. 22, pp. 4985–4990, 2007.
[71] B. Huang, F. Yu, and R. N. Zare, “Surface plasmon resonance imaging using a high numerical aperture microscope objective,” *Analytical chemistry*, vol. 79, no. 7, pp. 2979–2983, 2007.

7 List of Appendices

The presented Ph.D. thesis is based on the following works which have been authored or co-authored by the thesis author. For works where the thesis author is the first author, contributions of the other authors are listed. For works where the thesis author is not the first author, her contributions are listed. Thesis author's official name and surname have changed during her studies and are listed below in the current form and abbreviated as *J. J.*

I. Jani Jabloňků and Jiří Homola, "Convenient Method of Micrometer-Scale Excitation of Propagating Surface Plasmons by a Focused Laser Beam," *Plasmonics* vol. 9, no. 4: 737-739 (2014).

External contribution: Gold grating fabrication.

II. Jani Jabloňků, Karel Chadt, Milan Vala, Markéta Bocková, Jiří Homola, "Toward single-molecule detection with sensors based on propagating surface plasmons," *Optics Letters* vol. 37**,** no. 2, 163-165 (2012).

Other authors' contributions: Mechanical design of the microfluidic flow-cell (K.Ch.). Fabrication of gold gratings (M.V.). Surface chemistry (M.B.).

III. Jani Jabloňků, Tomáš Špringer, Milan Vala and Jiří Homola, "Micro-SPR sensor for the detection of a low number of DNA molecules," Conference poster, Book of Abstracts of the *Europt(r)ode XI 2012 – Conference on Optical Chemical Sensors and Biosensors*, Barcelona.

Other authors' contribution: Surface functionalization (T.Š.). Fabrication of gold gratings (M.V.).

IV. Tomáš Špringer, Maria Laura Ermini, Barbora Špačková, Jani Jabloňků, and Jiří Homola, "Enhancing sensitivity of surface plasmon resonance biosensors by functionalized gold nanoparticles: size matters," *Analytical Chemistry* vol. 86, no. 20: 10350-10356 (2014).

J. J. contribution: SEM imaging of sensor chips. Developed a system of semi-automated SEM substrate imaging and mapping. Developed a software tool for SEM image batch processing and particle density determination.

V. Marek Piliarik, Hana Šípová, Jani Jabloňků, Nicolle Galler, Joachim R. Krenn, and Jiří Homola, "High-resolution biosensor based on localized surface plasmons," *Optics Express* vol. 20, no. 1: 672-680 (2012).

J. J. contribution: Development of a computational cluster for FDTD. FDTD modelling of LSPs on gold nanorods and the optical response of the sample.

VI. Marek Piliarik, Jani Jabloňků, Nicolle Galler, Joachim R. Krenn, Jiří Homola, "Local refractive index sensitivity of plasmonic nanoparticles," *Optics Express* vol. 19**,** no. 10, 9213-9220 (2011).

J. J. contribution: FDTD modelling of the nanostructures.

Plasmonics (2014) 9:737–739
DOI 10.1007/s11468-013-9653-4

Convenient Method of Micrometer-Scale Excitation of Propagating Surface Plasmons by a Focused Laser Beam

Pavel Kvasnička · Jiří Homola

Received: 20 November 2013 / Accepted: 25 November 2013 / Published online: 7 December 2013

Abstract Surface plasmons (SPs) excited on microscopic areas are desired in a variety of applications, including SP microscopy and (bio)sensing. We present an optical method of excitation of SPs using a dry, medium-magnification microscope objective and a diffraction grating. SPs are excited by focusing laser light into a diffraction-limited spot on the grating. We demonstrate that the excitation of SPs is manifested by dark arcs in the light cone reflected from the focus. The behavior of the arcs with respect to the spatial distribution of refractive index in the vicinity of the focal spot is explored.

Keywords Surface plasmons · Diffraction gratings · Optical sensing and sensors · Microscopy

In recent years, there has been a growing interest in the excitation and observation of surface plasmons (SPs, [1]) within microscopic areas of the metal surface [2, 3]. The most common method of exciting SPs is via attenuated total reflection with the use of a prism coupler [1]. However, this method precludes the use of high magnification, high numerical aperture (N.A.) optics for imaging and thus limits the achievable spatial resolution in surface plasmon resonance (SPR) microscopy [4] and the minimal area of excitation of SPs in SPR sensors (250×600 μm; [5]). Recently, extremely high N.A. microscope objectives (N.A.>1.40) have been used to simultaneously serve as both a coupling prism and magnifying optics [3]. However, extremely high N.A. objectives are impractical due to their extremely short working distance and depth of focus, limited field of view, and the additional need for special immersion oils. In this letter, we present a convenient arrangement for the excitation of SPs by a laser beam focused into a sub-micron diffraction-limited spot via a regular dry (non-immersion) microscope objective using a diffraction grating as the coupling element and show that it allows observing changes in the spatial distribution of refractive index in the vicinity of the focal spot.

In order to excite SPs on a metal–dielectric interface by a free-space plane wave, the wave vector component parallel to the interface ("in-plane" component), $\mathbf{k}_{\|}=(k_x,k_y)$ has to match the wave vector of the SP, $\mathbf{k}_{\mathrm{SP}}$. However, the propagation constant of the SP,

$$k_{\mathrm{SP}} = k_0\sqrt{\frac{\varepsilon_{\mathrm{d}}\varepsilon_{\mathrm{m}}}{\varepsilon_{\mathrm{d}}+\varepsilon_{\mathrm{m}}}}, \tag{1}$$

is always larger than the wave number in the dielectric, where $k_0=2\pi/\lambda_0, \lambda_0$ is the free-space wavelength, ε_{d} is the permittivity of the dielectric, and ε_{m} is the permittivity of the metal. Figure 1 shows a diagram of $\mathbf{k}_{\mathrm{SP}}$ and of $\mathbf{k}_{\|}$ vectors corresponding to incident waves that are able to couple to SPs. The $\mathbf{k}_{\mathrm{SP}}$ vectors for different SP propagation azimuths constitute the circle marked "$\mathbf{k}_{\mathrm{SP}}$," lying outside the area of in-plane wave vectors available from a dry (i.e., N.A.<1) objective (gray area). When the metal surface is periodically corrugated into a diffraction grating with the wave vector $\mathbf{G}$, where $G=2\pi/\Lambda$ and Λ is the pitch of the grating, the wave vectors of incident waves that can couple with SPs obey

$$\mathbf{k}_{||,\mathrm{coupled}} = \mathbf{k}_{\mathrm{SP}} + m\mathbf{G},\ \ m = 0, \pm1, \pm2, \ldots \tag{2}$$

The $\mathbf{k}_{||,\mathrm{coupled}}$ vectors constitute the circles marked "$\mathbf{k}_{\mathrm{SP}}+1\cdot\mathbf{G}$" and "$\mathbf{k}_{\mathrm{SP}}-1\cdot\mathbf{G}$" in Fig. 1. It can be clearly seen from Fig. 1 that SPs on a diffraction grating can be excited by an incident free-space plane wave within the acceptance angle of a dry objective when the $\mathbf{k}_{\mathrm{SP}}$ and $m\mathbf{G}$

P. Kvasnička · J. Homola (✉)
Institute of Photonics and Electronics, Academy of Sciences of the Czech Republic, Chaberská 57, 18251 Prague, Czech Republic
e-mail: homola@ufe.cz

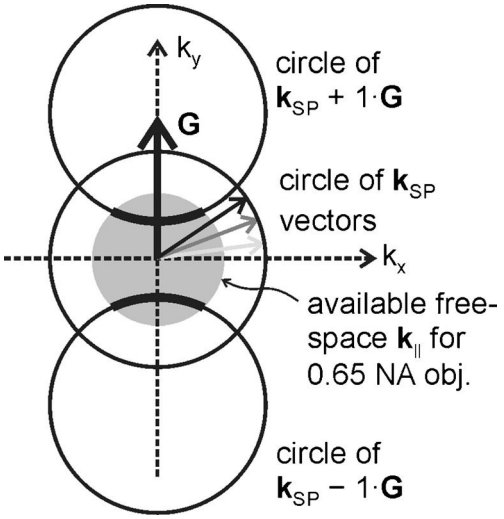

Fig. 1 Diagram of surface plasmon $\mathbf{k}_{SP}$ vectors and matching incident wave vector components $\mathbf{k}_{||}=(k_x, k_y)$ coupled via a diffraction grating with the wave vector G

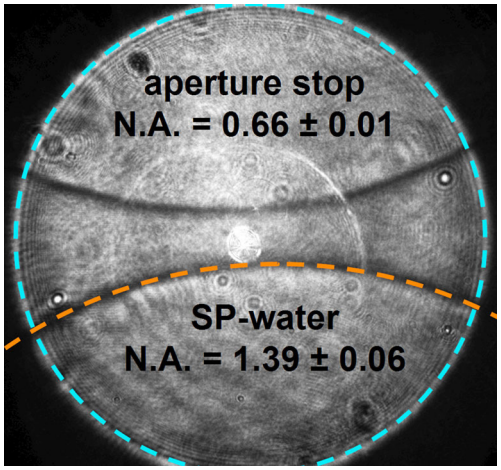

Fig. 3 (Color online) CCD image of the objective back focal plane showing the angular distribution of the intensity of the light reflected from the gold surface. The angular diameters of the objective's aperture stop (*blue*) and of the SP arcs for gold–water interface (SP-water, *orange*) are shown

vectors point in roughly opposite directions for their sum to match the $\mathbf{k}_{||,coupled}$ vector.

By focusing the light produced by a point source via the objective onto the grating, it is possible to excite SPs in an area of close vicinity of the diffraction-limited focus. The angular distribution (more precisely, the $\mathbf{k}_{||}$ distribution) of the light reflected from the focus can be observed in the back focal plane (BFP) of the objective (the distribution corresponding to the gray area, Fig. 1). The excitation of SPs is then manifested by two dark arcs in the image of the BFP. The arcs are essentially parts of grating-shifted copies of the $\mathbf{k}_{SP}$ circle, which itself lies beyond the reach of a dry objective.

In our experimental setup (Fig. 2), light from a laser diode (λ_0=750 nm) with the proper linear polarization was focused by a 40×/0.65 N.A. dry microscope objective onto the surface of an opaque gold film (thickness, 100 nm) that was vacuum-evaporated on a shallow relief diffraction grating (period, 520 nm; depth, 30 nm). The laser diode was operated below the lasing threshold to suppress the interference fringes in the images. The light reflected from the gold surface was imaged

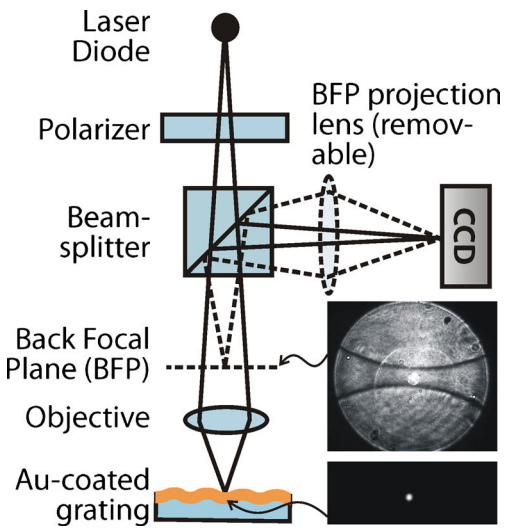

Fig. 2 (Color online) Layout of an optical system for excitation of SPs. *Top inset*: CCD image of the Back Focal Plane of the objective. *Bottom inset*: CCD image of the gold surface

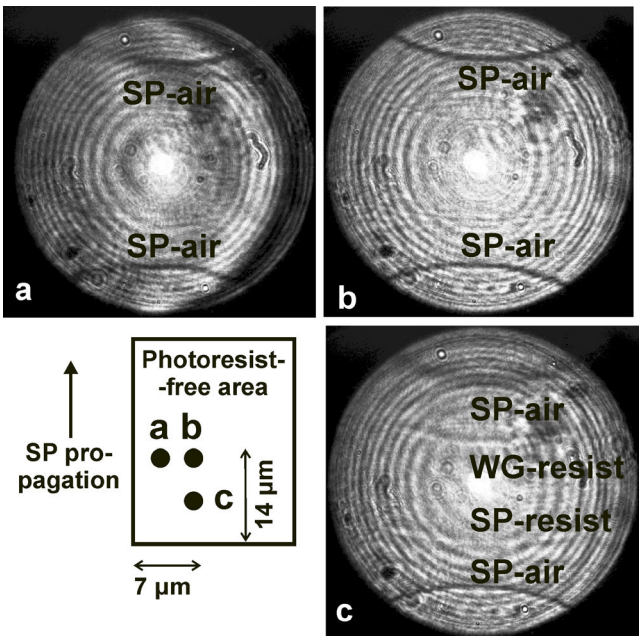

Fig. 4 SP arcs observed when moving the focal point from the photoresist-free to photoresist-coated areas. SP-air and SP-resist denote arcs corresponding to SPs on the gold–air and gold–photoresist interface, respectively. WG-resist denotes the arc for a waveguide mode propagating in the photoresist layer. In (*c*), the top three arcs correspond to WG and SP modes propagating downwards in the image and traversing the air–resist boundary; the bottom arc corresponds to an unperturbed SP mode propagating along the gold–air interface. The concentric fringes are due to interference within the coverslip gold–air gap

onto a CCD camera with or without an intermediate lens. The latter case allowed observing the spot created by the incident light (diameter about 0.9 μm, Fig. 2, bottom inset). In the former case (using an intermediate lens), the image of the BFP of the objective is projected onto the CCD (Fig. 2, top inset) clearly showing two dark arcs corresponding to the excitation of SPs.

To demonstrate that the observed arcs (Fig. 3) are indeed caused by the excitation of SPs, we compared the diameter of the arcs with a diameter predicted using Eq. (1), specifically, for the case of a gold-coated grating interfaced with water (using a drop of water and a coverslip). In order to determine the N.A. corresponding to the diameter of the dark arcs in Fig. 3, we calibrated the diameter of the image of the objective's aperture stop by measuring the divergence of the light cone exiting the objective (N.A. 0.66±0.1), and then determined that the arcs corresponded to a N.A. of 1.39±0.06 (FWHM of the arc's transverse profile is about 0.02). This value agrees well with the theoretical value (N.A.=1.39) predicted using Eq. (1).

When the refractive index of the dielectric medium in the vicinity of the laser focus is not homogeneous, the behavior of the arcs becomes more complex. To explore this behavior, we covered the gold with a thick layer of photoresist (thickness ~500 nm) by spin coating and removed the photoresist in a rectangle of 40×20 μm. Thus, we created two adjacent areas of different refractive indices. We then recorded images of the objective back focal plane while focusing light on different spots within the rectangular area. Figure 4 shows how the SP arcs change when the focus of the incident light approaches the boundary of the photoresist-free area. When the focus approaches the boundary lying in the direction of propagation of the SPs (Fig. 4 b–c), a reduction of the distance to the boundary from 14 to 7 μm causes the SP arc (corresponding to this direction, top arc) to double in width with a loss of contrast. In addition, two new arcs emerge; one arc corresponds to a SP on the photoresist-coated area ("SP-resist"), while the other is caused by a waveguide mode supported by the photoresist layer ("WG-resist"), as confirmed by the performed analysis of modes of the corresponding planar metal–dielectric waveguide. When the focus approaches the boundary which is perpendicular to the direction of propagation of SP (Fig. 4 b–a), reduction of the distance to the photoresist boundary from 7 to 3.5 μm results in broadening only of that half of the arc that faces the boundary (left side of a). This part of the arc corresponds to the SPs that propagate towards the boundary. These experiments suggest that the size of the area on the gold surface within which SPs are sensitive to changes in the refractive index is approximately 100 μm^2. The main factors affecting the size of the area are the propagation length of the SPs and the shape of the converging/diverging SP beam, which results from the excitation of SPs only in a limited span of azimuthal (within surface plane) angles (27°), as limited by the aperture of the objective.

In conclusion, we have presented an optical method of excitation of surface plasmons by focusing a laser beam into a diffraction-limited spot and demonstrated that excitation of surface plasmons gives rise to dark arcs in the reflected light cone and that the characteristics of the arcs are sensitive to the spatial distribution of refractive index in the vicinity of the focus. While the presented method allows for the localization of surface plasmons on a surface area of less than 100 μm^2, it retains the practical advantages of dry, medium-magnification microscope objectives. These advantages may benefit the development of surface plasmon resonance (SPR) biosensors for highly localized measurements.

Acknowledgments This research was supported by Praemium Academiae of the Academy of Sciences of the Czech Republic and the Czech Science Foundation under contract # P205/12/G118.

References

1. Raether H (1988) Surface plasmons on smooth and rough surfaces and on gratings. Vol. 111. Springer
2. Huang B, Yu F, Zare RN (2007) Surface plasmon resonance imaging using a high numerical aperture microscope objective. Anal Chem 79(7):2979–2983. doi:10.1021/ac062284x
3. Watanabe K, Horiguchi N, Kano H (2007) Optimized measurement probe of the localized surface plasmon microscope by using radially polarized illumination. Appl Opt 46(22):4985–4990. doi:10.1364/AO.46.004985
4. Yeatman EM (1996) Resolution and sensitivity in surface plasmon microscopy and sensing. Biosens Bioelectron 11(6–7):635–649. doi:10.1016/0956-5663(96)83298-2
5. Piliarik M, Homola J (2008) Self-referencing SPR imaging for most demanding high-throughput screening applications. Sensors Actuators B Chem 134(2):353–355. doi:10.1016/j.snb.2008.06.011

Toward single-molecule detection with sensors based on propagating surface plasmons

Pavel Kvasnička, Karel Chadt, Milan Vala, Markéta Bocková, and Jiří Homola*

Institute of Photonics and Electronics, Academy of Sciences of the Czech Republic, Chaberská 57, 18251 Prague, Czech Republic
**Corresponding author: homola@ufe.cz*

Received October 6, 2011; revised November 20, 2011; accepted November 21, 2011;
posted November 22, 2011 (Doc. ID 156096); published January 10, 2012

Surface plasmon resonance (SPR) sensors are known to be able to detect very low surface concentrations of (bio) molecules on macroscopic areas. To explore the potential of SPR biosensors to achieve single-molecule detection, we have minimized the read-out area (to ~64 μm^2) by employing a sensor system based on spectroscopy of surface plasmons generated on a diffractive structure via a microscope objective and light collection through a small aperture. This approach allows for decreasing the number of detected molecules by 3 orders of magnitude compared to state-of-the-art SPR sensors. A protein monolayer has been shown to produce a response of 5000 times the baseline noise, suggesting that as few as ~500 proteins could be detected by the sensor.

OCIS codes: 240.6700, 240.6680, 240.6690, 240.0310, 230.1950.

Surface plasmon resonance (SPR) biosensors have become an important tool for the investigation of (bio)molecules and their interactions in the life sciences [1] and have also been increasingly used in bioanalytics to detect chemical and biological substances related to medical diagnostics, environmental monitoring, food safety, security, etc. [2]. In the past decade, SPR biosensor technology has also made great advances in terms of portability, multiplexing capabilities, and performance [2,3]. In SPR sensors, propagating surface plasmons (PSPs) are typically excited and read out over an area of the order of 1 mm^2. At the lowest surface concentration of analyte molecules detectable by state-of-the-art SPR biosensors, such an area contains about a million molecules [4]. In recent years sensors utilizing localized surface plasmons (LSPs) [5] have been widely researched with the goal of developing highly miniaturized biosensors (down to individual nanoparticles) that would be able to achieve the ultimate goal of detecting a single molecule. LSP-based sensors have been demonstrated to be able to detect hundreds of protein molecules with the potential for improvement down to the single-molecule level [6,7]. In this Letter, we explore the possibility of developing an experimental platform based on propagating surface plasmons, which would enable the SPR sensor to detect extremely small numbers of molecules.

The presented approach is based on an optical system with a minimized PSP excitation and collection area. In our experiments, we used spectroscopy of PSPs excited on a thin gold film with a relief diffraction grating via diffractive coupling. We have minimized the PSP collection area by imaging the sensing surface by a microscope objective onto a small aperture and collecting and analyzing the light passing through (Fig. 1). The virtual image of the aperture on the surface defined the sensing area from which the light was collected. In the experimental setup, polychromatic light emitted by a superluminescent light-emitting diode (SLED) (740–760 nm wavelength) was linearly polarized and then collimated by a series of cylindrical lenses and a microscope objective (40×, 0.65 NA or 60×, 0.85 NA). The obliquely incident light was coupled to PSPs by a sine relief grating (pitch, 520 nm; depth, 30 nm) on the SPR chip, prepared by replicating a grating master (prepared by optical interferometric lithography) into a UV-curable polymer layer on a glass substrate, and coating the replica with a 150 nm thick Au layer by thermal evaporation in vacuum. The chip was interfaced with a microfluidic flow cell. Light reflected from the chip was separated from the incident light by a beam splitter and imaged onto a collection aperture (roughly 0.1 mm × 0.5 mm), which restricted the chip area from which the light was collected. The virtual image of the aperture on the chip was 2.0 μm × 6.5 μm. The collected light was analyzed using a spectrograph. The SPR spectrum was obtained by dividing the spectrum measured with the TM-polarized light by that obtained for the TE polarization. The spectral position of the SPR dip (FWHM, 8 nm) was calculated and tracked as a function of time.

Even though the collection area is only 2.0 μm × 6.5 μm, the area contributing to changes in SPR dip position (the sensitive area) is larger. The length of the sensing area should be comparable to the propagation length of the PSPs (about 45 μm for the gold/air interface at 755 nm and about 18 μm for the gold/water interface). Once PSPs are excited, they propagate a certain length along the gold layer, and undergo attenuation and outcoupling into light again. PSPs excited farther from the collection spot contribute less to the collected spectrum due to their exponential attenuation ($1/e^2$ over

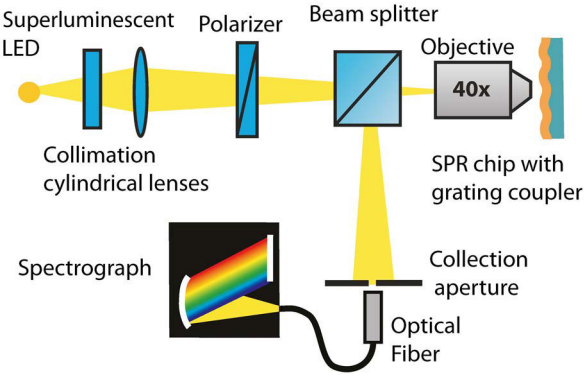

Fig. 1. (Color online) Optical setup of the SPR sensor with a minimized sensing area.

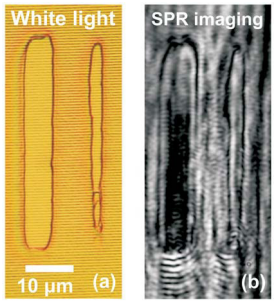

Fig. 2. (Color online) (a) Optical micrograph of the sensing structure with a photoresist layer and resist-free windows of different sizes (the grating grooves are clearly visible). (b) SPR image of the resist-free windows. The dark color corresponds to the excitation of PSPs.

the propagation length). Moreover, it should be noted that PSPs are excited and propagate in a range of angles, whose span is equal to the illuminating beam's divergence in the plane parallel to the grating grooves, defining the width of the sensing area.

To estimate the dimensions of the sensing area, we covered the sample with a photoresist layer and in the layer we etched elongated resist-free windows of different sizes [$6\,\mu\text{m} \times 40\,\mu\text{m}$ and $2.6\,\mu\text{m} \times 40\,\mu\text{m}$, Fig. 2(a)]. We observed changes in the SPR dip in the reflectance spectrum as the distance between the collection spot and the window edge along the direction of PSP propagation decreases (Fig. 3) (for PSPs on the gold/air interface and 60× objective). At the distance of ~18 μm, the photoresist was found to disturb the SPR dip, which became shallower and wider, manifesting the limited lifetime and propagation length available to the PSPs. The disturbance is due to the momentum matching condition not being fulfilled over the resist-covered areas. In the smaller window ($2.6\,\mu\text{m} \times 40\,\mu\text{m}$), no SPR dip was observed. To observe the absence of PSPs in the smaller window directly and with a resolution better than the collection area size, we employed an SPR imaging approach by replacing the wide-bandwidth SLED with a laser diode tuned to the resonant wavelength. Figure 2(b) presents the SPR image of the two windows. PSPs are not excited in the smaller window, because its width is not sufficient to support the full range of propagation angles. The dark area in

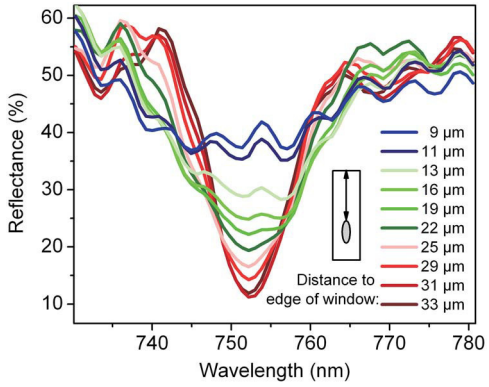

Fig. 3. (Color online) Dependence of the shape of the SPR dip on the distance between the collection area and the edge of the resist-free window.

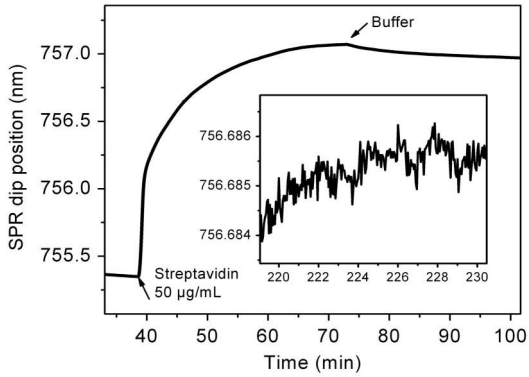

Fig. 4. Temporal response of the SPR sensor to the formation of the streptavidin monolayer. Inset: baseline noise.

the larger window corresponds to the excitation of PSPs, which propagate in one direction only (from the bottom to the top in Fig. 2). At the distance of ~15 μm from the upper end of the window, the area gets lighter as the PSPs collected there are more disturbed by the edge of the window. The propagation length of the PSP for the gold/water interface is only about 40% of that for the gold/air interface, reducing the decaying part of the sensing area accordingly. The effective length of the sensing area for water as the medium was then 13 μm (sum of the propagation length of the PSP and the collection area length). The width of the dark area of 4 μm sets an upper limit on the width of the sensing area and is clearly sufficient to support the full range of propagation angles (if some of the PSPs originating in the dark area hit the left or right edge, the area would not appear completely dark). The total sensing area is thus smaller than $4 \times 13\,\mu\text{m}^2 = 52\,\mu\text{m}^2$. For the 40× objective, the area is smaller than $4 \times 16\,\mu\text{m}^2 = 64\,\mu\text{m}^2$.

To determine the lowest number of protein molecules detectable by the sensor, we first determined the noise in the position of the SPR dip (0.3 pm rms for 3 s averaging time and 40× objective) (Fig. 4 inset) and then measured the shift in the position of the SPR dip induced by a protein monolayer of a known surface coverage. By following the protocol in [8], we coated the sensing surface with a streptavidin monolayer. In short, a self-assembled alkanethiol monolayer was formed on the surface, functional groups were activated using *N*-hydroxysuccinimide/1-ethyl-3-[3-dimethylaminopropyl]carbodiimide hydrochloride chemistry, and then streptavidin molecules were attached via covalent coupling. This procedure leads to highly reproducible streptavidin monolayers with a surface concentration of ~34,000 molecules per μm^2 (~5×5 nm^2 per molecule) or a surface coverage of 3.4 ng/mm^2 [8]. In our experiment, the presence of the streptavidin monolayer resulted in a shift of the SPR dip by 1.45 nm (Fig. 4). If we define the minimum detectable surface concentration as the number of molecules inducing an SPR dip shift equivalent to the sensor's RMS noise—(monolayer surface coverage) × (sensitive area) × (baseline noise/monolayer response)—the minimum detectable surface concentration achieved in our experiments is as low as 450 molecules. This value corresponds to a surface coverage of 0.7 pg/mm^2. In comparison, state-of-the-art SPR sensors based on

spectroscopy of PSPs (with a sensing spot area of about 7 mm^2 and a minimum detectable surface coverage of 0.13 pg/mm^2) [9] and SPR imaging (with a spot size of 0.15 mm^2 and a minimum detectable surface coverage of 0.2 pg/mm^2) [4] can detect about 9×10^6 and 3×10^5 molecules, respectively. These values are comparable with those achieved by the typical commercial SPR sensors.

In conclusion, we have demonstrated that the lowest number of molecules detectable by SPR sensors based on propagating surface plasmons can be improved by 3 orders of magnitude in comparison with the existing SPR sensors. The performance of our sensor is limited mainly by the propagation length of the PSPs. It is envisioned that, by engineering the propagation length through changes to the operating wavelength and grating profile, and by further improving the experimental setup (e.g., increasing light levels, improving mechanical stability), the lowest detectable number of molecules can be reduced to several tens.

This research was supported by the Academy of Sciences of the Czech Republic by Praemium Academiae and under the contract KAN200670701, and by the Ministry of Education, Youth, and Sports under contracts OC09058 and LH11102.

References

1. R. L. Rich and D. G. Myszka, J. Mol. Recognit. **23**, 1 (2010).
2. J. Homola, Chem. Rev. **108**, 462 (2008).
3. M. Piliarik and J. Homola, Opt. Express **17**, 16505 (2009).
4. M. Piliarik and J. Homola, Sens. Actuators B **134**, 353 (2008).
5. T. Sannomiya and J. Voros, Trends Biotechnol. **29**, 343 (2011).
6. A. D. McFarland and R. P. Van Duyne, Nano Lett. **3**, 1057 (2003).
7. K. M. Mayer, F. Hao, S. Lee, P. Nordlander, and J. H. Hafner, Nanotechnology **21**, 255503 (2010).
8. X. D. Su, Y. J. Wu, R. Robelek, and W. Knoll, Langmuir **21**, 348 (2005).
9. K. Pimková, M. Bocková, K. Hegnerová, J. Suttnar, J. Čermák, J. Homola, and J. Dyr, "Surface plasmon resonance biosensor for the detection of VEGFR-1—a protein marker of myelodysplastic syndromes," Anal. Bioanal. Chem., doi:10.1007/s00216-011-5395-3 (to be published).

micro-SPR SENSOR FOR THE DETECTION OF A LOW NUMBER OF DNA MOLECULES

Pavel Kvasnička, Tomáš Špringer, Milan Vala and Jiří Homola
Institute of Photonics and Electronics, Chaberská 57, Prague, Czech Republic

❶ INTRODUCTION

Surface plasmon resonance (SPR) biosensors for bioanalytics have traditionally been focused on low limits of detection with respect to volume concentration of analyte in a liquid sample. However, even for the best SPR biosensors, the actual detectable *number of molecules* bound to the sensing surface is on the order of millions.

Here we present an **SPR-based** optical platform and an amplification method which allow for the **detection of individual ssDNAs** (TP53 - a part of a gene sequence with a key role in tumor suppression), when **labeled** by 30 nm gold nanoparticles **(AuNPs)**.

❷ micro-SPR SENSOR

The previously developed *micro-SPR* sensor platform allows for the reduction of the number of detected molecules by minimizing the readout area (64 μm^2) on the surface of the SPR chip [1]. It is based on spectroscopy of **propagating surface plasmons** excited via a diffractive coupling on a gold-coated harmonic diffraction grating (the SPR chip) using a **microscope objective** (Figure 1). The readout area is delimited by a 0.1x0.5 mm aperture in the image plane.

The S/N ratio of the micro-SPR sensor is sufficient for the detection of ~500 unlabeled protein molecules (surface concentration 0.7 pg/mm^2).

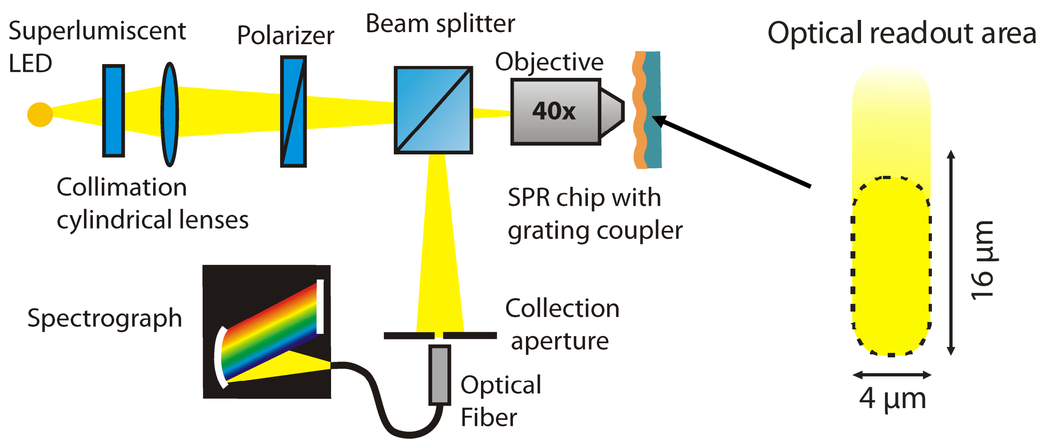

Figure 1. Optical setup of the micro-SPR sensor platform with a minimized sensing area.

❸ ssDNA AMPLIFICATION

To enable resolving individual biotinilated TP53 molecules an amplification method using streptavidin-functionalized 30 nm AuNPs was developed. Stages of the assay are shown in Figure 2.

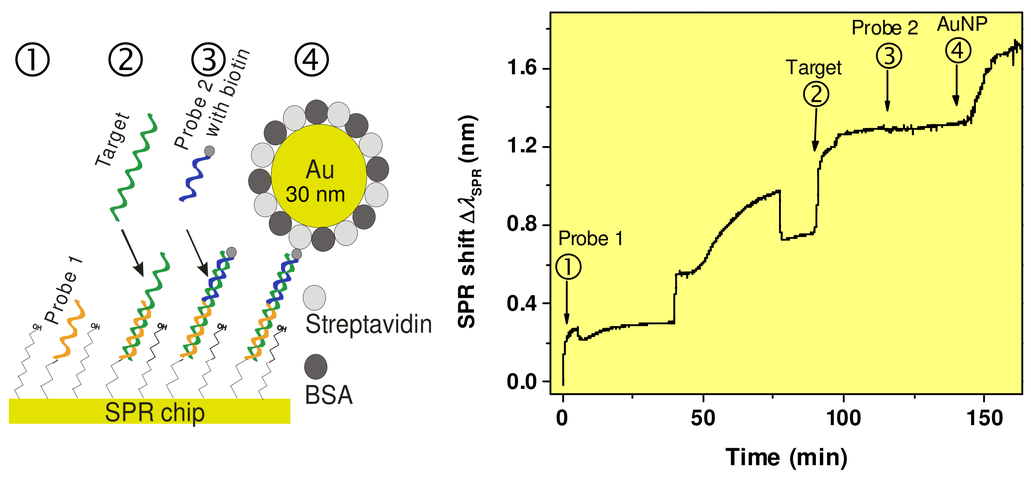

Figure 2. LEFT: Amplification scheme using functionalized AuNPs. The DNA target binds to DNA probe 1 (2); then DNA probe 2 terminated with biotin binds to the target (3); finally, AuNPs bind to probe 2 via the streptavidin-biotin interaction (4). **RIGHT:** Sensor response for (1)-(4).

[1] P. Kvasnička, J. Homola et al., Optics Letters ***37*** (2), 163-165 **(2012)**

Acknowledgement: This work was supported by the Academy of Sciences of the Czech Republic by Praemium Academiae and the Czech National Science Foundation (grant # P 205/12/G118).

❹ SENSOR RESPONSE TO SINGLE ssDNA – AuNP BINDING

The sensor response (SPR dip wavelength shift vs. time) contains **well-resolved steps** (discontinuities) as a result of the binding events between ssDNA molecules on surface and the AuNPs (Figure 3).

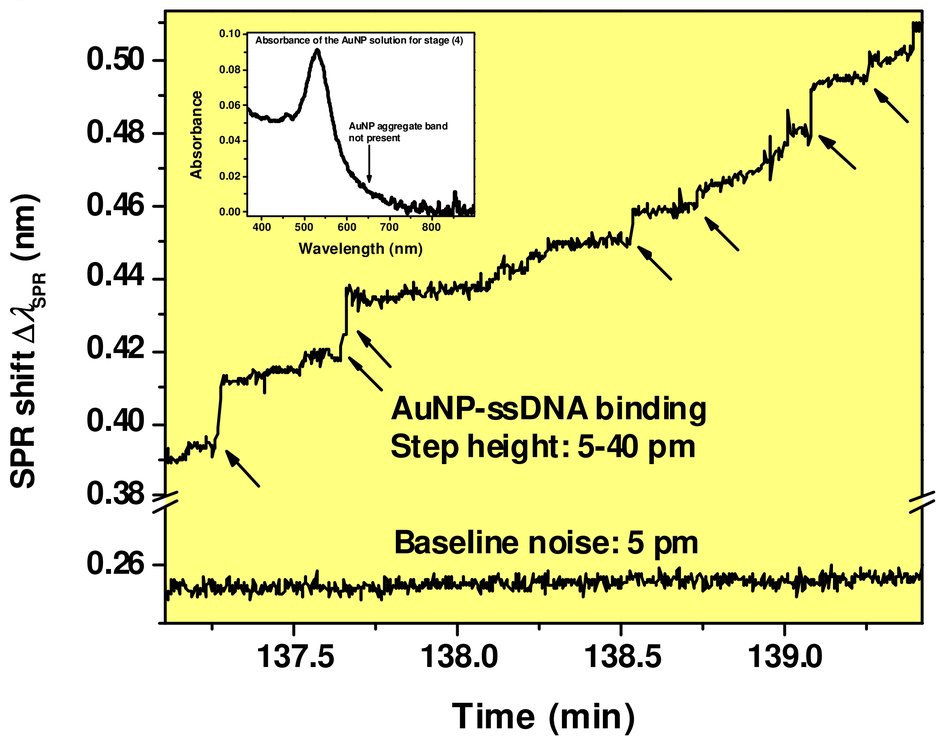

Figure 3. A segment of the sensor response to AuNPs (stage (4) in Figure 2) showing the steps corresponding to the binding of individual Au-NP labeled short ssDNA molecules. **Inset:** Absorbance of the AuNP solution showing that AuNPs are not aggregated.

To verify that the steps correspond to individual AuNP bindings, we have investigated the following:

AuNP-concentration dependence of step rate

The step rate is approximately proportional to concentration (for higher step rates some steps were not resolvable due to mutual proximity) => steps are caused by the AuNP solution.

AuNP relative concentration	steps / min	total SPR shift / min $\Delta\lambda_{SPR}$ (pm)
1	1.1	12
3	2.7	30
9	>6.7	77

Continuous vs. discrete SPR shift

The steps (~200 counts) account for about 80% of the total SPR shift => steps are caused by the dominantly contributing species – AuNPs or AuNP aggregates.

Absorption spectrum of the AuNP solution

AuNP aggregates comprise negligible part of the AuNP solution, as shown by the lack of the 650 nm aggregate absorption band (Figure 3, inset) => steps are caused by individual AuNPs.

❺ CONCLUSIONS

The feasibility of obtaining SPR response from individual functionalized AuNPs was shown. These can serve as labels for DNA molecules, which could then be **individually** detected.

www.ufe.cz | kvasnicka@ufe.cz

INSTITUTE OF PHOTONICS AND ELECTRONICS

analytical chemistry

Article

pubs.acs.org/ac

Enhancing Sensitivity of Surface Plasmon Resonance Biosensors by Functionalized Gold Nanoparticles: Size Matters

Tomáš Špringer, Maria Laura Ermini, Barbora Špačková, Jani Jabloňků, and Jiří Homola*

Institute of Photonics and Electronics AS CR, v. v. i., Chaberská 57, 182 51, Prague, Czech Republic

Supporting Information

ABSTRACT: We study how the size of spherical gold nanoparticles (AuNPs) influences their ability to enhance the response of optical biosensors based on surface plasmon resonance (SPR). We present a theoretical model that relates the enhancement generated by the AuNPs to their composition, size, and concentration, thus allowing for accurate predictions regarding the SPR sensor response to various AuNPs. The effect of the AuNP size is also investigated experimentally using an SPR biosensor for the detection of carcinoembryonic antigen (CEA) in which AuNPs covered with neutravidin (N-AuNPs) are used in the last step of a sandwich assay to enhance the sensor response to biotinylated secondary antibody against CEA. The experimental data are in excellent agreement with the results of the theoretical analysis. We demonstrate that the sensor response enhancement generated by the N-AuNPs is determined by (i) the sensor sensitivity to N-AuNP surface density (S_σ) and (ii) the ability of the N-AuNPs to bind to the functionalized surface of the sensor. Our results indicate that, while S_σ increases with the size of the N-AuNP, the ability of the functionalized surface of the sensor to bind the N-AuNPs is affected by steric effects and decreases with the size of N-AuNP.

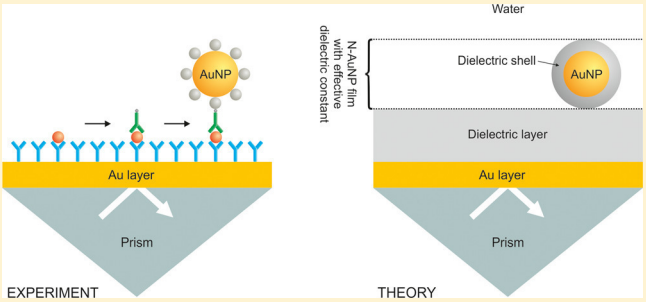

Surface plasmon resonance (SPR) biosensors are among the most advanced label-free optical biosensor technologies and hold potential for applications in numerous important fields, such as medical diagnostics, environmental monitoring, food safety, and security.[1] In order to push for the detection of analytes present at extremely low concentrations, various methods for increasing the sensitivity of SPR biosensors have been developed. Most of these methods are based on changing the refractive index at the sensor surface by means of a variety of (bio)chemical or nanoparticle agents, which are captured by the sensor surface subsequent to the binding of the target analyte to the primary biorecognition elements. These methods include the use of secondary and tertiary antibodies,[2−4] antibodies labeled with enzymes,[5,6] and dielectric[7,8] or metallic nanoparticles (NPs).[6,9−12] In particular, gold spherical nanoparticles (AuNPs) of diameters ranging from 5 to 40 nm have been widely used to enhance the response of SPR biosensors. For instance, Huang et al. used a biotinylated secondary antibody along with 20 nm AuNPs coated with streptavidin to improve the limit of detection (LOD) for prostate-specific antigen in buffer from 10 ng/mL to subng/mL levels.[9] Cao and Sim used a double-enhancement strategy in which AuNPs were coated with HRP-labeled antibody for the detection of PSA down to the subng/mL level.[6] In our recent work, we employed 30 nm AuNPs functionalized with streptavidin to detect carcinoembryonic antigen (CEA) in 50% blood plasma down to a 0.1 ng/mL level.[10] Despite this rather broad use of AuNPs in SPR biosensors, there is a lack of quantitative data describing the influence of the size of AuNPs on the outcome of the detection.[13,14]

Previous experimental studies involving the effect of the size and surface density of bare AuNPs on the sensor response have been somewhat limited, both in number and in scope. In two separate studies, Lyon et al. investigated the sensor response to AuNPs with diameters ranging from 25 to 60 nm. They observed that the sensor response increased with the size of AuNPs; however, the increase was not consistent across their studies.[15,16] He et al. adsorbed 12 and 45 nm AuNPs onto a SiO_2-coated SPR chip and observed that 45 nm AuNPs produced a similar sensor response as 12 nm AuNPs, although the surface density of 45 nm AuNPs was smaller by a factor of 20.[17] Halpern et al. also adsorbed AuNPs having diameters in the range of 20 to 100 nm and observed that the sensor response increased with the volume of AuNPs.[18] Unlike the adsorption of bare nanoparticles, AuNPs employed in biomolecular detection assays are typically functionalized with molecules that bind to the analyte (or to another molecule bound to the analyte) previously captured on the sensor surface. The affinity between the functionalized AuNPs and the sensor is influenced by several conditions at the surface (Coulombic interactions, steric effects, stability of the complex with an analyte), all of which may influence the binding of

Received: July 17, 2014
Accepted: September 16, 2014
Published: September 16, 2014

   dx.doi.org/10.1021/ac502637u | *Anal. Chem.* 2014, 86, 10350−10356

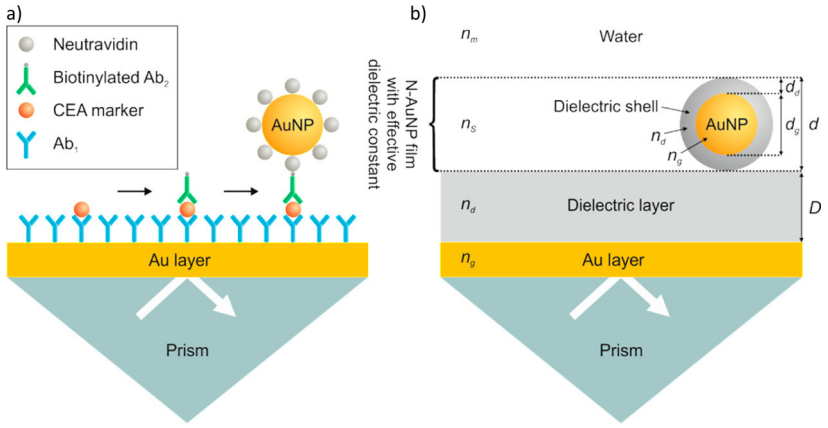

Figure 1. (a) Scheme of the experiment: sandwich assay for the N-AuNP-enhanced detection of CEA. (b) Theoretical representation—multilayer structure described by multiple refractive indexes (n_g, n_d, n_S, n_m) and thicknesses of the layers (D, d).

AuNPs on a surface of SPR biosensor.[13] The affinity binding of AuNPs of varying sizes has been reported only in a limited number of SPR studies,[11,19,20] which due to these complexities produced results which are difficult to draw universal conclusions from. While the studies performed by Uludag and Tothill[11] and Albers et al.[20] led to the conclusion that larger AuNPs produce a higher sensor response enhancement, Mitchell et al. observed no significant difference between the sensor response enhancement when using AuNPs with diameters ranging from 25 to 50 nm.[19] This suggests that the role the size of AuNPs plays in the interaction with an SPR surface is not fully understood.

In this paper, we investigate the ability of functionalized AuNPs to enhance the response of an SPR biosensor in a biomolecular detection assay, with special attention given to the study of the effect of the size of AuNPs. The sensor response (a shift in the SPR wavelength, $\Delta\lambda_r$) is studied in terms of two aspects: the surface density of captured AuNPs ($\Delta\sigma$) and the sensor sensitivity to AuNP surface density (S_σ) which are related as follows:

$$\Delta\lambda_r = \Delta\sigma \cdot S_\sigma \tag{1}$$

The first aspect ($\Delta\sigma$) is defined by the ability of the functionalized AuNPs to bind to the SPR sensor surface (the interaction of the functionalized AuNPs with the target molecule). This aspect is investigated in a model experiment in which a cancer biomarker (carcinoembryonic antigen, CEA) is detected using an SPR biosensor in a sandwich detection format. Specifically, neutravidin-functionalized AuNPs (N-AuNPs) of different sizes are used to enhance the sensor response to CEA via a biotinylated secondary antibody (Figure 1a). The second aspect (S_σ) is defined only by the optical properties of both the functionalized N-AuNPs and the properties of the sensor. This aspect represents the ratio between changes in the sensor response to changes in the N-AuNP surface density. To offer a better insight into this aspect, we present a new analytical theory describing the relationship between S_σ and the parameters of the experimental setup based on both perturbation theory,[21] which is used to describe the sensitivity to surface refractive index changes of a multilayer structure (Figure 1b), and the theory of an effective dielectric constant of a film consisting of randomly distributed nanoparticles.[22] Compared to previous theoretical studies concerning the effect of the presence of AuNPs on the optical response of an SPR sensor,[22,23] the model presented here provides an analytical formula that makes it possible to quantify the effects of parameters directly related to the experiment and, furthermore, allows for the design of an experimental system providing optimal performance.

MATERIALS AND METHODS

Reagents. Sodium acetate buffer solution, 3 M, pH 5.2 (25 °C), KH_2PO_4, Na_2HPO_4, KCl, NaCl, ethanolamine, bovine serum albumin (BSA), streptavidin, and glutaraldehyde were purchased in molecular biology grade or higher from Sigma-Aldrich, USA. *N*-Hydroxysuccin imide (NHS) and 1-ethyl-3-(3-(dimethylamino)propyl) carbodiimide hydrochloride (EDC) were purchased from GE Healthcare, USA. Primary IgG1-type antibody (Ab_1) against CEA, biotinylated secondary IgG1-type antibody (Ab_2) against CEA, and CEA were purchased from Fitzgerald, USA. Carboxy-terminated [HS−$(CH_2)_{11}$−EG_6−OCH_2−COOH] and hydroxy-terminated [HS−C_{11}−EG_4−OH] alkanethiols were purchased from Prochimia, Poland. Ethanol for spectroscopy (purity 99.9% or greater) was purchased from Merck, USA. The composition of phosphate buffer (PBS) was 1.4 mM KH_2PO_4, 8 mM Na_2HPO_4, 2.7 mM KCl, and 137 mM NaCl, pH 7.4 at 25 °C. PBS_{NaCl} consisted of phosphate buffer with the addition of 750 mM NaCl. PBS_{BSA} buffer was prepared by adding BSA to PBS to reach a concentration of 250 μg/mL. SA_{10} consisted of 10 mM sodium acetate, pH 5 at 25 °C. All buffers were prepared using deionized water (18 MΩ/cm resistivity, Direct-Q from Millipore).

Gold Nanoparticles. Spherical AuNPs covalently functionalized with neutravidin via a 2 nm polymer bridge were purchased from Nanopartz Inc., USA. The diameters of the gold core of N-AuNPs were calculated as (10 ± 2), (15 ± 2), (21 ± 2), (33 ± 1), and (52 ± 3) nm via scanning electron microscopy (SEM). These N-AuNPs were highly purified upon purchase; however, for precautionary measures, we washed them with PBS_{BSA} in order to remove any potentially free neutravidin from the solution prior to the SPR experiments. The N-AuNPs were centrifuged once for the 10 and 15 nm N-AuNPs (at 12 500 rpm for 30 min) and five times for the 21, 33, and 52 nm N-AuNPs (at 10 000 rpm for 15 min). Between the centrifugation cycles, the supernatant liquid was removed and the pellet was dissolved in 1 mL of PBS_{BSA}. After the last washing cycle, solutions of N-AuNPs were diluted in PBS_{BSA} to reach an optical density of 0.1 for the 10 and 15 nm N-AuNPs and 0.3 for the 21, 33, and 52 nm N-AuNPs (maximum of UV

dx.doi.org/10.1021/ac502637u | *Anal. Chem.* 2014, 86, 10350−10356

absorbance peak, 1 mm optical path length). The optical densities of N-AuNPs were measured using a NanoPhotometer Pearl UV−vis absorption spectrometer (Implen, Germany). The concentrations of N-AuNPs were calculated to be 10.5 (2.6 or 16.7 nM for the control experiment), 3.1, 3.4, 0.9, and 0.2 nM (0.11 or 0.45 nM for the control experiment) for N-AuNPs of the diameters of 10, 15, 21, 33, and 52 nm, respectively. The extinction coefficients (obtained from Nanopartz Inc.) for the 10, 15, 21, 33, and 52 nm N-AuNPs were 9.5×10^7, 3.2×10^8, 8.8×10^8, 3.3×10^9, and 1.5×10^{10} M^{-1} cm^{-1}, respectively.

SPR Biosensor. A laboratory four-channel SPR platform based on the wavelength spectroscopy of surface plasmons (Plasmon IV)[21] using dispersionless microfluidics[24,25] developed at the Institute of Photonics and Electronics, Czech Republic, was used in this study. In this type of SPR sensor, the angle of incidence of the light beam is fixed and the SPR dip is observed in the spectrum of light coupled to a surface plasmon. The sensor response is expressed in terms of the wavelength at which the SPR dip occurs (SPR wavelength). This response is sensitive to changes in the refractive index caused by the binding of molecules to the surface of an SPR chip. A shift of 1 nm in the SPR wavelength represents a change in the protein surface coverage of 17 ng/cm^2.[10] SPR chips were prepared by coating BK7 glass substrates with thin layers of titanium (1−2 nm) and gold (48 nm) via e-beam evaporation in vacuum.

The SPR chips used in this work were functionalized with a self-assembled monolayer of mixed carboxy-terminated and hydroxy-terminated alkanethiols, on which antibodies were immobilized using the covalent coupling as described previously.[10] A brief description of the immobilization process is provided below. Initially, a 3:7 mixture of $HS-(CH_2)_{11}-(EG)_6-OCH_2-COOH$ and $HS-C_{11}-(EG)_4-OH$ thiols was dissolved in ethanol at a total concentration of 0.2 M. A clean SPR chip was immersed in the thiol mixture for 10 min at 40 °C and stored at a room temperature for at least 12 h. Then, the chip was rinsed with ethanol and deionized water and mounted into the SPR sensor. SA_{10} buffer was flowed along the SPR chip surface for 5 min, after which the chip surface was incubated in 0.5 M NHS/0.1 M EDC (dissolved in SA_{10}) for 10 min to activate the carboxyl groups. After the activation, Ab_1 at a concentration of 10 μg/mL (67 nM) in SA_{10} was injected for 15 min to achieve a maximum surface coverage level. After short injection of SA_{10}, PBS_{NaCl} was pumped for 5 min to remove the noncovalently bound Ab_1. After another short injection of SA_{10}, 1 mM aqueous ethanolamine (pH 8 at 25 °C) was flowed along the sensor surface for 5 min to deactivate any remaining carboxyl groups.

SPR Experiments. The effect of the AuNPs size on the SPR sensor response was studied in a model sandwich assay for the detection of CEA. A scheme of this assay is shown in Figure 1a.

In a typical SPR experiment, all four channels (two detection and two reference channels) were used to measure the binding of two different sizes of N-AuNPs. In each detection channel, CEA, Ab_2, and N-AuNPs were consecutively injected to form the sandwich, while in the reference channel all the assay steps were performed except for the injection of CEA. Specific steps were as follows. Prior to the detection of CEA, the sensor surface with immobilized Ab_1 was incubated in PBS_{BSA} for 15 min. Then, CEA at a concentration of 500 ng/mL (2.5 nM) in PBS_{BSA} and PBS_{BSA} was injected for 10 min through the detection and reference channels, respectively. After a short injection of PBS_{BSA}, Ab_2 (10 μg/mL, 67 nM) was pumped through both the detection and reference channels for 15 min. After another short injection of PBS_{BSA}, solutions of N-AuNPs were flowed through both channels. In order to capture the maximum amount of N-AuNPs (and achieve a maximum enhancement), the concentrations of N-AuNPs in each SPR experiment were preselected to maximize the sensor response obtained within a time frame of several hours, such that the N-AuNP surface density had approached an equilibrium state. Finally, the solution of N-AuNPs was replaced with PBS_{BSA}.

An additional experiment was carried out to confirm the long-term stability of the Ab_1-CEA-Ab_2 complex. In this experiment, a rather high concentration of CEA (1000 ng/mL) was used, and after the formation of Ab_1-CEA-Ab_2, PBS_{BSA} was pumped through the sensing channel for several hours, while the sensor response was recorded. For the determination of kinetic and equilibrium constants, CEA at concentrations of 250, 500, 1500, and 5000 ng/mL in PBS_{BSA} were injected into the parallel channels of the SPR sensor and flowed over the antibody-coated surface for 10 min. Then, PBS_{BSA} was pumped for 20 min to obtain the dissociation phase of the interaction. The kinetic constants were determined with BIAevaluation software (Biacore, version 4.1) using a 1:1 Langmuir model, which also considered mass transport effects. It should be noted that all SPR experiments reported in this work used a flow rate and temperature of 20 μL/min and 25 °C, respectively.

SEM Measurements. After the SPR experiments, the SPR chips were analyzed via SEM (e_LiNE plus system produced by Raith, Germany) in order to determine the diameter and surface density of the N-AuNPs on the SPR chip surface. In order to avoid any loss of N-AuNPs from the surface of an SPR chip during the transition from the SPR sensor to the SEM, the N-AuNPs were covalently immobilized to the surface of the SPR chip via glutaraldehyde. The immobilization was performed as follows. PBS_{BSA} was replaced with SA_{10}, and 2.5% (v/v) glutaraldehyde in SA_{10} was injected for 30 min to cross-link the amino-groups of molecules on the surface of SPR chip. Then, SA_{10} was again injected. Before the removal of a chip from the SPR biosensor, Q water was flowed through the flow-cell to remove any residual salts from the surface of the SPR chip.

The diameter and surface density of N-AuNPs on the SPR chip surface were determined from SEM images collected by an e_LiNE plus system by means of an in-lens secondary electron detector and a 10 kV acceleration voltage. Surface densities were calculated using the public domain software ImageJ (http://imagej.nih.gov/ij/). The images (10 μm × 10 μm) were taken from five different spots across each channel.

RESULTS AND DISCUSSION

SPR Sensor Response to N-AuNPs. In order to characterize the enhancement of the sensor response due to the capture of N-AuNPs, we utilized the sandwich assay shown in Figure 1a. A typical sensorgram showing the sensor response in different stages of the assay is shown in Figure 2. The injection of CEA ($K_{D(CEA)} = 3.3 \times 10^{-10}$ M; see Figure S-1 in the Supporting Information) gave rise to a sensor response that increased linearly with time, reaching a value of 0.45 ± 0.05 nm after 10 min (measured across all experiments). This injection time was limited in order to obtain a sensor surface having a low CEA surface density as to minimize potential effects related to crowding. We determined that the surface density of CEA (M = 200 kDa) was 228 CEA/μm^2, which implied that only 2.9% of the Ab_1 (the response of 12 nm, M = 150 kDa) was occupied by CEA. The response to the secondary antibody was

dx.doi.org/10.1021/ac502637u | Anal. Chem. 2014, 86, 10350−10356

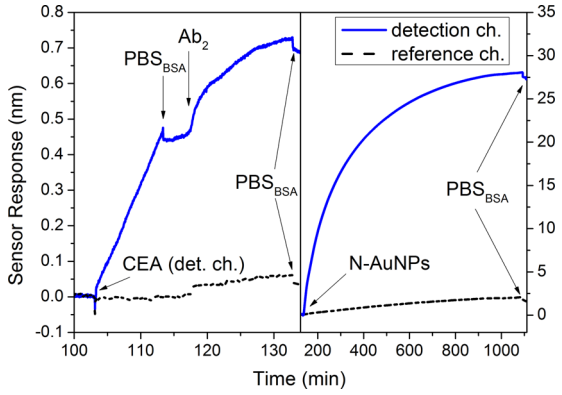

Figure 2. Sensor response obtained during a typical CEA assay using 33 nm N-AuNPs.

found to increase with time, reaching a plateau of 0.17 ± 0.03 nm in 15 min. The subsequent time-response to N-AuNPs was dependent on the size of N-AuNPs and varied from several nanometers to several tens of nanometers. The nonspecific binding of N-AuNPs in a reference channel (caused by both the adsorption of N-AuNPs to the SPR chip surface and by specific binding of N-AuNPs to nonspecifically bound biotinylated Ab_2) was in each case lower than 10% of the enhanced sensor response obtained in the detection channel. Therefore, the nonspecific binding of N-AuNPs had a rather minor effect on the outcome of the experiments considering the much higher specific sensor response.

Using the results of each detection experiment, we calculated the equilibrium sensor response ($\Delta\lambda_r$) as the difference between the sensor response of the detection and the reference channels, where $\Delta\lambda_r$ thus describes the sensor response to only the specifically bound N-AuNPs. The values of $\Delta\lambda_r$ obtained for the 5 different sizes of N-AuNPs are shown in Figure 3.

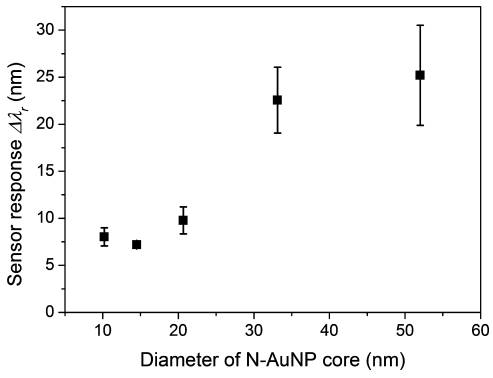

Figure 3. Sensor responses, $\Delta\lambda_r$, for N-AuNPs with diameters of the gold core of 10, 15, 21, 33, and 52 nm. Errors were calculated as the standard deviation from at least three measurements regarding different SPR chips.

The $\Delta\lambda_r$ values obtained for the two smallest N-AuNPs did not differ considerably, and the $\Delta\lambda_r$ values of the three smallest N-AuNPs were much lower than the $\Delta\lambda_r$ values observed for the two largest N-AuNPs. Specifically, the 52 nm diameter N-AuNPs generated a $\Delta\lambda_r$ value 3.5 times higher than that observed when using 15 nm N-AuNPs. The trend of higher $\Delta\lambda_r$ values obtained with larger AuNPs is in agreement with results published in Uludag and Tothill[11] and Albers et al.[20] As follows from Figure 3, the relative standard deviation of $\Delta\lambda_r$ tends to increase with increasing diameter of N-AuNPs. We believe that this is mainly due to the greater ability of bigger AuNPs to enhance the differences among different experiments.

We also performed control experiments where we evaluated (i) the effect of different concentrations of N-AuNPs (for the same nanoparticle size) and (ii) the long-term stability of the Ab_1-CEA-Ab_2 complex. Regarding (i), we investigated whether $\Delta\lambda_r$ was independent of the concentration of the injected N-AuNPs. We pumped 2.6 and 16.7 nM solutions of 10 nm N-AuNPs and 0.11 and 0.44 nM solutions of 52 nm N-AuNPs across the surface with immobilized Ab_2 at a constant surface coverage (see Figure S-2 in the Supporting Information). Note here that these two N-AuNP concentrations were chosen to be lower and higher than the respective concentrations used in the main SPR experiment (10.5 and 0.2 nM for 10 and 52 nm N-AuNPs, respectively). From Figure S-2 in the Supporting Information, it can be seen that the obtained $\Delta\lambda_r$ values were approximately the same for both N-AuNP concentrations, for both diameters (10 and 52 nm). Therefore, we concluded that the $\Delta\lambda_r$ values have rather low dependence on the particle concentration (where the N-AuNP concentration used herein is well above the equilibrium dissociation constant of the Ab_2/N-AuNP affinity complex). Regarding the long-term stability of the Ab_1-CEA-Ab_2 complex (ii), buffer was flowed across the sensor surface with the Ab_1-CEA-Ab_2 complex for several hours and the dissociation phase of the bound CEA-Ab_2 complex was observed (see Figure S-3 in the Supporting Information). This experiment revealed that Ab_2 does not dissociate from the surface of an SPR chip (in appreciable amounts during the time scales involved within this study) and confirmed that the stability of the Ab_1-CEA-Ab_2 complex is not of concern here.

Surface Density of N-AuNPs. The surface densities ($\Delta\sigma$) of N-AuNPs for each measurement were obtained via SEM images as the difference between the densities measured in the detection and reference channels (see Figure 4). The mean values of surface densities $\Delta\sigma$ were found to be 106.1, 53.2, 19.9, 15.0, and 3.9 N-AuNPs/μm^2 for the diameters of 10, 15, 21, 33, and 52 nm, respectively. From the SPR sensor response to the biotinylated secondary antibody, we estimated the surface density of Ab_2 to be 116 $Ab_2/\mu m^2$. Assuming that the N-AuNP/Ab_2 obeys a 1:1 affinity interaction, we estimated that 91.5% and 3.4% of Ab_2 were occupied by the smallest and largest N-AuNPs, respectively.

As follows from the SEM measurements (Figure 4), the dependence of $\Delta\sigma$ on the size of the N-AuNPs was rather dramatic: $\Delta\sigma$ for the 10 nm N-AuNPs was 27 times larger than that observed for the 52 nm N-AuNPs. This remarkable difference cannot be explained by the blocking of the N-AuNP binding due to the closely packed arrangement of N-AuNPs on a chip surface. We estimate that the surface coverage was only about 0.8% for both 10 and 52 nm N-AuNPs, which offered ample room for the capture of additional N-AuNPs. This steep decrease in $\Delta\sigma$ cannot be explained by the difference in concentrations of N-AuNPs, as we observed only very low sensitivity of $\Delta\lambda_r$ to the variations in the concentration of N-AuNP (see above). Therefore, we hypothesize that this effect of N-AuNP size on $\Delta\sigma$ was caused by (a) steric effects that influenced the accessibility of biotin for binding to the N-AuNPs, (b) binding of several N-AuNPs to multiple biotins on a single Ab_2, and (c) binding of one N-AuNP to one or more biotins on multiple Ab_2 antibodies. These effects will be explored below.

dx.doi.org/10.1021/ac502637u | Anal. Chem. 2014, 86, 10350−10356

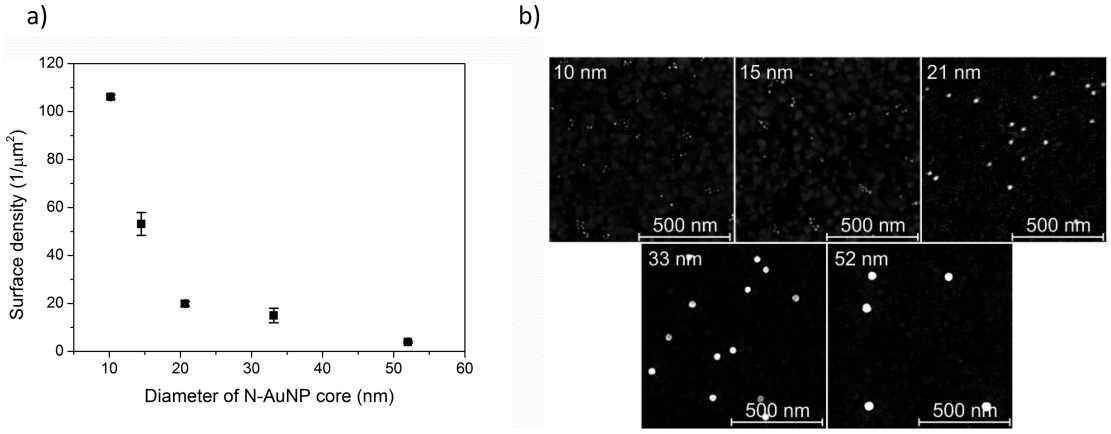

Figure 4. (a) Surface densities obtained for five different N-AuNP sizes. Errors were calculated as the standard deviation from three different chips, where five spots were measured across each chip. (b) SEM images of the surface of an SPR chip with N-AuNPs of different sizes.

To investigate the role of steric effects on the binding of N-AuNPs on the surface of an SPR chip (a), we carried out an experiment in which the incubation of the surface with the largest 52 nm N-AuNPs was followed by the injection of the smallest 10 nm N-AuNPs (Figure 5). The sensor exhibited a

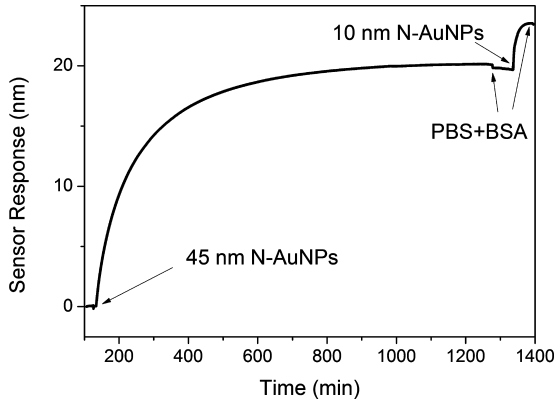

Figure 5. Reference compensated sensor response to the injection of 0.2 nM, 52 nm N-AuNPs followed by the injection of 10.5 nM, 10 nm N-AuNPs.

$\Delta\lambda_r$ value of 20 nm to the injection of the 52 nm N-AuNPs and was followed by a response of 4 nm to the 10 nm N-AuNPs. This additional binding of the 10 nm N-AuNPs demonstrated that there were unoccupied biotins still present on the surface of an SPR chip, and furthermore, these unoccupied sites remained active for the interaction with additional N-AuNPs. Quantitatively, the amount of unoccupied biotin sites after incubation with the 52 nm N-AuNPs was approximately 50% of the originally accessible biotin. This experiment clearly demonstrated that the accessibility of biotins for N-AuNP binding was higher for the smaller N-AuNPs and, furthermore, provides a partial explanation for the strong effect that the N-AuNP size has on $\Delta\sigma$ seen in Figure 4a. This hypothesis was also supported by another experiment in which streptavidin was pumped along the surface of the SPR chip prior to the injection of N-AuNPs (data are not shown). We estimated that each Ab_2 was able to bind approximately three streptavidins. In comparison, this binding capacity was higher by a factor of 3 and 6 with respect to $\Delta\sigma$ values of the 10 and 15 nm N-AuNPs, respectively.

In regards to (b), the observed $\Delta\sigma$ may have also been affected by the binding of several N-AuNPs to a single Ab_2. Although we do not know the exact volume occupied by each Ab_2, the typical dimensions of an antibody vary from 15 to 20 nm in length, from 6 to 15 nm in width, and from 6 to 10 nm in height.[11] These dimensions suggest that the probability of multiple N-AuNP binding events to a single Ab_2 will increase with a decrease in the size of the N-AuNP, in particular for the smallest N-AuNPs used in this study. Therefore, it is likely that this effect will lead to an increase in $\Delta\sigma$ for smaller N-AuNPs.

In regards to (c), the possible binding of one N-AuNP to one or more biotins on multiple Ab_2 antibodies, assuming the above stated dimensions of Ab_2 (specifically the average footprint: 18 nm × 10 nm), the coverage of Ab_2 was estimated to be about 2%, having an average distance between homogeneously distributed Ab_2 of approximately 77 nm. In reality, the distribution of Ab_2 on the surface is random and the real distance between Ab_2 will be much smaller, allowing for the possibility of a larger N-AuNP to bind to biotin sites on multiple Ab_2. As follows, it is likely that this effect will lead to a decrease in $\Delta\sigma$ for larger N-AuNPs.

Sensitivity to Surface Density of AuNPs. Experimental values of S_σ (Figure 6) were obtained by dividing the equilibrium sensor response $\Delta\lambda_r$ (Figure 3) by the surface density $\Delta\sigma$ determined by SEM measurements (Figure 4) for each N-AuNP size.

Below, we present an analytical theory describing the experimental system. The multilayer structure that we consider is shown in Figure 1b, which consists of a gold layer ($n_g = (\varepsilon_g)^{1/2} = 0.138 + 4.49i$ at $\lambda_r = 750$ nm[26]), a thin dielectric layer representing a self-assembled monolayer of alkylthiols with immobilized biorecognition elements ($D = 10$ nm, $n_d = (\varepsilon_d)^{1/2} = 1.42$[27]), a layer composed of randomly distributed N-AuNPs of overall thickness d surrounded in aqueous medium, and the aqueous medium ($n_m = (\varepsilon_m)^{1/2} = 1.33$). N-AuNPs were simulated as core−shell particles, composed of a gold core with a diameter d_g and a dielectric shell representing the linker layer and biomolecules attached to the surface of the AuNP ($d_d = 10$ nm). The effective dielectric constant of the layer of N-AuNPs $\varepsilon_S = n_S^2$ was simulated using the theory of optical properties of materials consisting of randomly distributed nanoparticles at low surface coverage[22] and can be written as

$$\varepsilon_S = \varepsilon_m\left(1 + \frac{\sigma\alpha}{d}\right) \quad (2)$$

dx.doi.org/10.1021/ac502637u | Anal. Chem. 2014, 86, 10350−10356

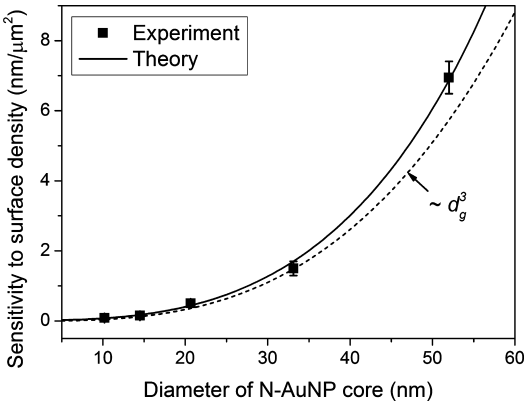

Figure 6. Theoretical (calculated using eq 6) and experimental sensor sensitivity S_σ to surface density as a function of N-AuNP size. The dotted line represents a cubic dependence of S_σ on the AuNP diameter calculated by the simplified model using eq 7. The error bars are the propagated standard deviation from the results shown in Figures 3 and 4.

where σ and α are the surface density and polarizability of the N-AuNP, respectively. If the N-AuNP size is smaller than the wavelength of the incident light, we can apply the electrostatic approximation,[28] where the polarizability of the N-AuNP is expressed as

$$\alpha = \pi d^3 \frac{\varepsilon - \varepsilon_m}{6\varepsilon_m + 2(\varepsilon - \varepsilon_m)F} \tag{3}$$

where ε is the effective dielectric constant of the core−shell particle,[28] $\varepsilon = \varepsilon_d[1 + 3\beta/(1 - \beta)]$, with $\beta = f(\varepsilon_g - \varepsilon_d)/(3\varepsilon_d + (\varepsilon_g - \varepsilon_d))$, and $f = d_g^3/(d_g + 2d_s)^3$ is the fraction of the total particle volume occupied by the gold core. The factor $F = 1 - F_1 - F_2 - F_3$ includes three correction terms which take into account the dynamic depolarization $F_1 = (kd)^2/4$, radiative damping ($F_2 = i(kd)^3/12$),[29] and the influence of the presence of the gold layer $F_3 = (1/4)[d/(2D^* + d)]^3((\varepsilon_g - \varepsilon_m)/(\varepsilon_g + \varepsilon_m))$, $D^* = (D\varepsilon_d)/\varepsilon_m$ (approximation for high angles of incidence).[30]

The sensitivity of an SPR sensor (based on wavelength modulation) to changes in the surface density of N-AuNPs can be written as

$$S_\sigma = \frac{d\lambda_r}{d\sigma} = \frac{d\lambda_r}{dn_S}\frac{dn_S}{d\varepsilon_S}\frac{d\varepsilon_S}{d\sigma} = \frac{S_S}{2n_m}\frac{d\varepsilon_S}{d\sigma} \tag{4}$$

where $S_S = d\lambda_r/dn_S$ is the sensitivity to refractive index changes within the layer containing the randomly distributed N-AuNPs. As follows from perturbation theory,[22] the sensitivity S_S can be expressed as $S_S = S_B I_S d$, where $S_B = (d\lambda_r/dn_m)$ is the sensitivity to bulk refractive index changes (S_B = 4081 nm/RIU for λ_r = 750 nm). The term I_s is a factor reflecting the exponential profile of the surface plasmon field and can be written as

$$I_S = \frac{1 - \exp(-2d/L_{pd})}{d} \tag{5}$$

where L_{pd} is the penetration depth of the surface plasmon (L_{pd} = 275 nm for λ_r = 750 nm). By applying the perturbation theory and eq 2 and further neglecting the effect of the imaginary part of α, eq 4 can be reduced to

$$S_\sigma = \frac{n_m}{2} S_B I_S Re\{\alpha\} \tag{6}$$

As follows from eq 6, S_σ is directly proportional to (i) the bulk sensitivity S_B that describes the sensitivity of the sensor to refractive index changes, (ii) the factor I_S that accounts for the profile of the surface plasmon field (the I_S factor decreases with the size of the N-AuNPs), and (iii) the real part of the particle polarizability $Re\{\alpha\}$. The term $Re\{\alpha\}$ depends on the size and composition of the N-AuNPs, the distance of the N-AuNPs from the metal layer surface, and the incident wavelength. Specifically, for wavelengths longer than the localized surface plasmon resonance (LSPR) wavelength of a N-AuNP, $Re\{\alpha\}$ increases with the N-AuNP size, while the opposite trend holds for wavelengths shorter than the LSPR.[22]

In the special cases such that the N-AuNPs are rather distant from the surface ($d \ll D$, $F_3 \approx 0$), the effect of their shell is negligible ($\varepsilon \approx \varepsilon_g$); furthermore, if their size is much smaller that the incident wavelength ($d \ll \lambda_r$, $F_1 \approx F_2 \approx 0$), the real part of polarizability $Re\{\alpha\}$ increases with d_g^3. Additionally, if the diameter of N-AuNPs is much smaller than the penetration depth of the surface plasmon ($d \ll L_{pd}$), I_S can be reduced to $I_S \approx 2/L_{pd}$ (becoming independent of d), and the model can be simplified to

$$S_\sigma \approx \pi d_g^3 \frac{S_B n_m}{L_{pd}} Re\left\{\frac{(\varepsilon_g - \varepsilon_m)}{6\varepsilon_m + 2(\varepsilon_g - \varepsilon_m)}\right\} \tag{7}$$

where sensitivity S_σ is proportional to d_g^3.

Figure 6 shows S_σ calculated for a range of AuNP diameters using eq 6 (solid line) and eq 7 (dashed line). It can be seen that for very small N-AuNPs (until the diameter of N-AuNP core reaches about 20 nm) the simplified model (eq 7) provides accurate prediction and the sensitivity of the SPR sensor to N-AuNPs increases with approximately the third power of the diameter of the N-AuNP core. With further increases in the diameter of N-AuNPs core, the simplified model yields underestimated values; the faster growth of S_σ for larger N-AuNPs is a consequence of dynamic depolarization, radiative damping, the influence of the presence of the gold layer, and the fact the SPR wavelength is much longer than the LSPR wavelength of the N-AuNPs. The theoretical model described by eq 6 (solid line) is in excellent agreement with the experimental data throughout the whole range of AuNP diameters.

CONCLUSIONS

In this paper, we describe, both theoretically and experimentally, the ability of gold spherical NPs to enhance the sensitivity of SPR biosensors. The effect of NPs on the response of SPR sensor was experimentally studied using gold nanoparticles functionalized with neutravidin (N-AuNPs) in a model sandwich assay for the detection of carcinoembryonic antigen (CEA). The detection experiments combined with the characterization of each SPR chip using electron microscopy revealed that the observed sensor response enhancement is determined by two factors: sensor sensitivity to N-AuNP surface density (the response of the sensor to the single nanoparticle per unit surface, S_σ) and the ability of the N-AuNPs to bind functionalized sensor surface. Both these factors were found to have dependence on the size of the N-AuNPs; while the pure optical enhancement was found to increase with the size of N-AuNPs, the number of N-AuNPs bound to the SPR chip surface followed an opposite trend. To our knowledge, this represents the first time that the effect of the AuNP size on its ability to bind to target molecules on the

dx.doi.org/10.1021/ac502637u | Anal. Chem. 2014, 86, 10350−10356

sensor surface has been observed and quantified in SPR biosensor-based biodetection experiments. In addition, our findings suggest that this effect can be potentially significant and should be taken into account when planning the use of NPs to enhance the sensitivity of an SPR sensor. These results should stimulate and guide research into surface functionalization toward functional sensor surfaces and NPs harnessing the full enhancement potential of NPs predicted by theory.

A theoretical model has been established that describes the SPR sensor response due to the presence of the NPs. The model provides an analytical formula that relates S_σ with measurable characteristics of the NPs (composition, size) and geometry (distance of NPs from the surface of the SPR chip). This formula offers a simple means for predicting the enhancement of the sensor response for specific NPs, including variable experimental geometries, and provides a better understanding of the roles that pertinent experimental parameters may play. Special attention was paid to the role of the diameter of the NPs, and we described the conditions under which the enhancement follows the intuitive trend of scaling with the volume of the NP and, furthermore, how (potentially substantially) the enhancement may differ outside these conditions. The dependence of the optical enhancement on the size of N-AuNP provided by the theoretical model was in excellent agreement with the experimental data. Although the theory presented herein was developed for SPR biosensors, it can be adopted to different types of optical biosensors and expanded to a wide variety of sensor sensitivity enhancing NPs.

■ ASSOCIATED CONTENT

Supporting Information

Control experiments. This material is available free of charge via the Internet at http://pubs.acs.org.

■ AUTHOR INFORMATION

Corresponding Author

*E-mail: homola@ufe.cz.

Notes

The authors declare no competing financial interest.

■ ACKNOWLEDGMENTS

We thank N. S. Lynn for valuable comments and discussions. This research was supported by Praemium Academiae of the Academy of Sciences of the Czech Republic, the Czech Science Foundation (Contract # P205/12/G118) and by the US Army Research Office (Contract # W911NF-13-1-0460).

■ REFERENCES

(1) Homola, J. *Chem. Rev.* **2008**, *108*, 462−493.
(2) Su, F.; Xu, C.; Taya, M.; Murayama, K.; Shinohara, Y.; Nishimura, S. I. *Sensors* **2008**, *8*, 4282−4295.
(3) Chung, J. W.; Park, J. M.; Bernhardt, R.; Pyun, J. C. *J. Biotechnol.* **2006**, *126*, 325−333.
(4) Teramura, Y.; Iwata, H. *Anal. Biochem.* **2007**, *365*, 201−207.
(5) Kim, M. G.; Shin, Y. B.; Jung, J. M.; Ro, H. S.; Chung, B. H. *J. Immunol. Methods* **2005**, *297*, 125−132.
(6) Cao, C.; Sim, S. J. *J. Microbiol. Biotechnol.* **2007**, *17*, 1031−1035.
(7) Kubitschko, S.; Spinke, J.; Bruckner, T.; Pohl, S.; Oranth, N. *Anal. Biochem.* **1997**, *253*, 112−122.
(8) Teramura, Y.; Arima, Y.; Iwata, H. *Anal. Biochem.* **2006**, *357*, 208−215.
(9) Huang, L.; Reekmans, G.; Saerens, D.; Friedt, J. M.; Frederix, F.; Francis, L.; Muyldermans, S.; Campitelli, A.; Van Hoof, C. *Biosens. Bioelectron.* **2005**, *21*, 483−490.
(10) Springer, T.; Homola, J. *Anal. Bioanal. Chem.* **2012**, *404*, 2869−2875.
(11) Uludag, Y.; Tothill, I. E. *Anal. Chem.* **2012**, *84*, 5898−5904.
(12) Schneider, B. H.; Dickinson, E. L.; Vach, M. D.; Hoijer, J. V.; Howard, L. V. *Biosens. Bioelectron.* **2000**, *15*, 13−22.
(13) Bedford, E. E.; Spadavecchia, J.; Pradier, C. M.; Gu, F. X. *Macromol. Biosci.* **2012**, *12*, 724−739.
(14) Kwon, M. J.; Lee, J.; Wark, A. W.; Lee, H. J. *Anal. Chem.* **2012**, *84*, 1702−1707.
(15) Lyon, L. A.; Pena, D. J.; Natan, M. J. *J. Phys. Chem. B* **1999**, *103*, 5826−5831.
(16) Lyon, L. A.; Musick, M. D.; Smith, P. C.; Reiss, B. D.; Pena, D. J.; Natan, M. J. *Sens. Actuators, B: Chem.* **1999**, *54*, 118−124.
(17) He, L.; Smith, E. A.; Natan, M. J.; Keating, C. D. *J. Phys. Chem. B* **2004**, *108*, 10973−10980.
(18) Halpern, A. R.; Wood, J. B.; Wang, Y.; Corn, R. M. *ACS Nano* **2014**, *8*, 1022−1030.
(19) Mitchell, J. S.; Wu, Y. Q.; Cook, C. J.; Main, L. *Anal. Biochem.* **2005**, *343*, 125−135.
(20) Albers, W. M.; Munter, T.; Laaksonen, P.; Vikholm-Lundin, I. *J. Colloid Interface Sci.* **2010**, *348*, 1−8.
(21) Vaisocherova, H.; Zitova, A.; Lachmanova, M.; Stepanek, J.; Kralikova, S.; Liboska, R.; Rejman, D.; Rosenberg, I.; Homola, J. *Biopolymers* **2006**, *82*, 394−398.
(22) Uchiho, Y.; Shimojo, M.; Furuya, K.; Kajikawa, K. *J. Phys. Chem. C* **2010**, *114*, 4816−4824.
(23) Golden, M. S.; Bjonnes, A. C.; Georgiadis, R. M. *J. Phys. Chem. C* **2010**, *114*, 8837−8843.
(24) Springer, T.; Piliarik, M.; Homola, J. *Sensor Actuat B-Chem.* **2010**, *145*, 588−591.
(25) Springer, T.; Piliarik, M.; Homola, J. *Anal. Bioanal. Chem.* **2010**, *398*, 1955−1961.
(26) Johnson, P. B.; Christy, R. W. *Phys. Rev. B* **1972**, *6*, 4370−4379.
(27) Malinsky, M. D.; Kelly, K. L.; Schatz, G. C.; Van Duyne, R. P. *J. Am. Chem. Soc.* **2001**, *123*, 1471−1482.
(28) Bohren, C. F. Huffman, D. R. *Absorption and Scattering of Light by Small Particles*; John Wiley and Sons: New York, 1983.
(29) Jensen, P. *Rev. Mod. Phys.* **1999**, *71*, 1695−1735.
(30) Pinchuk, A.; Hilger, A.; von Plessen, G.; Kreibig, U. *Nanotechnology* **2004**, *15*, 1890−1896.

High-resolution biosensor based on localized surface plasmons

Marek Piliarik,[1] Hana Šípová,[1] Pavel Kvasnička,[1] Nicolle Galler,[2] Joachim R. Krenn,[2] and Jiří Homola[1,*]

[1] *Institute of Photonics and Electronics, Academy of Sciences of the Czech Republic, Chaberská 57, Prague, Czech Republic*

[2] *Institute of Physics, Karl-Franzens University Graz, Graz, Austria*

[*] *homola@ufe.cz*

Abstract: We report on a new biosensor with localized surface plasmons (LSP) based on an array of gold nanorods and the total internal reflection imaging in polarization contrast. The sensitivity of the new biosensor is characterized and a model detection of DNA hybridization is carried out. The results are compared with a reference experiment using a conventional high-resolution surface plasmon resonance (SPR) biosensor. We show that the LSP-based biosensor delivers the same performance as the SPR system while involving significantly lower surface densities of interacting molecules. We demonstrate a limit of detection of 100 pM and a surface density resolution of only 35 fg×mm^{-2} that corresponds to less than one DNA molecule per nanoparticle on average.

OCIS codes: (240.6680) Surface plasmons; (280.4788) Optical sensing and sensors; (310.6628) Subwavelength structures, nanostructures.

References and links

1. J. Homola, "Surface plasmon resonance sensors for detection of chemical and biological species," Chem. Rev. **108**(2), 462–493 (2008).
2. B. Sepúlveda, P. C. Angelome, L. M. Lechuga, and L. M. Liz-Marzan, "LSPR-based nanobiosensors," Nano Today **4**(3), 244–251 (2009).
3. P. Kvasnička and J. Homola, "Optical sensors based on spectroscopy of localized surface plasmons on metallic nanoparticles: sensitivity considerations," Biointerphases **3**(3), FD4–FD11 (2008).
4. K. M. Mayer, F. Hao, S. Lee, P. Nordlander, and J. H. Hafner, "A single molecule immunoassay by localized surface plasmon resonance," Nanotechnology **21**(25), 255503 (2010).
5. H. W. Huang, C. R. Tang, Y. L. Zeng, X. Y. Yu, B. Liao, X. D. Xia, P. G. Yi, and P. K. Chu, "Label-free optical biosensor based on localized surface plasmon resonance of immobilized gold nanorods," Colloids Surf., B **71**(1), 96–101 (2009).
6. J. X. Fu, B. Park, and Y. P. Zhao, "Nanorod-mediated surface plasmon resonance sensor based on effective medium theory," Appl. Opt. **48**(23), 4637–4649 (2009).
7. M. D. Arnold, M. G. Blaber, M. J. Ford, and N. Harris, "Universal scaling of local plasmons in chains of metal spheres," Opt. Express **18**(7), 7528–7542 (2010).
8. E. Petryayeva and U. J. Krull, "Localized surface plasmon resonance: nanostructures, bioassays and biosensing--a review," Anal. Chim. Acta **706**(1), 8–24 (2011).
9. S. Chen, M. Svedendahl, M. Käll, L. Gunnarsson, and A. Dmitriev, "Ultrahigh sensitivity made simple: nanoplasmonic label-free biosensing with an extremely low limit-of-detection for bacterial and cancer diagnostics," Nanotechnology **20**(43), 434015 (2009).
10. A. B. Dahlin, J. O. Tegenfeldt, and F. Höök, "Improving the instrumental resolution of sensors based on localized surface plasmon resonance," Anal. Chem. **78**(13), 4416–4423 (2006).
11. M. Piliarik, P. Kvasnička, N. Galler, J. R. Krenn, and J. Homola, "Local refractive index sensitivity of plasmonic nanoparticles," Opt. Express **19**(10), 9213–9220 (2011).
12. M. Piliarik, L. Párová, and J. Homola, "High-throughput SPR sensor for food safety," Biosens. Bioelectron. **24**(5), 1399–1404 (2009).
13. M. Piliarik, H. Vaisocherova, and J. Homola, "Towards parallelized surface plasmon resonance sensor platform for sensitive detection of oligonucleotides," Sens. Actuators B Chem. **121**(1), 187–193 (2007).
14. M. Svedendahl, S. Chen, A. Dmitriev, and M. Käll, "Refractometric sensing using propagating versus localized surface plasmons: a direct comparison," Nano Lett. **9**(12), 4428–4433 (2009).

#157119 - $15.00 USD Received 2 Nov 2011; revised 5 Dec 2011; accepted 10 Dec 2011; published 23 Dec 2011

15. M. Piliarik and J. Homola, "Surface plasmon resonance (SPR) sensors: approaching their limits?" Opt. Express **17**(19), 16505–16517 (2009).
16. B. Lamprecht, G. Schider, R. T. Lechner, H. Ditlbacher, J. R. Krenn, A. Leitner, and F. R. Aussenegg, "Metal nanoparticle gratings: influence of dipolar particle interaction on the plasmon resonance," Phys. Rev. Lett. **84**(20), 4721–4724 (2000).
17. J. Homola, *Surface Plasmon Resonance Based Sensors* (Springer-Verlag, Berlin-Heidelberg-New York, 2006).
18. H. Vaisocherová, A. Zítová, M. Lachmanová, J. Stepánek, S. Králíková, R. Liboska, D. Rejman, I. Rosenberg, and J. Homola, "Investigating oligonucleotide hybridization at subnanomolar level by surface plasmon resonance biosensor method," Biopolymers **82**(4), 394–398 (2006).
19. K. M. Mayer and J. H. Hafner, "Localized surface plasmon resonance sensors," Chem. Rev. **111**(6), 3828–3857 (2011).
20. G. J. Nusz, S. M. Marinakos, A. C. Curry, A. Dahlin, F. Höök, A. Wax, and A. Chilkoti, "Label-free plasmonic detection of biomolecular binding by a single gold nanorod," Anal. Chem. **80**(4), 984–989 (2008).
21. S. Techane, D. R. Baer, and D. G. Castner, "Simulation and modeling of self-assembled monolayers of carboxylic acid thiols on flat and nanoparticle gold surfaces," Anal. Chem. **83**(17), 6704–6712 (2011).
22. T. Cassier, K. Lowack, and G. Decher, "Layer-by-layer assembled protein/polymer hybrid films: nanoconstruction via specific recognition," Supramol. Sci. **5**(3-4), 309–315 (1998).
23. A. Rachkov, S. Patskovsky, A. Soldatkin, and M. Meunier, "Surface plasmon resonance detection of oligonucleotide sequences of the rpoB genes of Mycobacterium tuberculosis," Talanta **85**(4), 2094–2099 (2011).
24. E. Milkani, S. Morais, C. R. Lambert, and W. G. McGimpsey, "Detection of oligonucleotide systematic mismatches with a surface plasmon resonance sensor," Biosens. Bioelectron. **25**(5), 1217–1220 (2010).

1. Introduction

Surface plasmon resonance (SPR) has become the technology of choice in numerous biosensing applications providing a tool for the real-time analysis of molecular interactions and rapid and label-free detection of chemical and biological species [1]. Besides the propagating surface plasmon polaritons (SPP) which have dominated the field of SPR biosensing for nearly thirty years, the last decade has witnessed a growing exploitation of the localized surface plasmons (LSP) generated on metallic nanostructures [2]. In spectroscopic LSP-based biosensors, refractive index changes induced by biomolecular interactions are measured by tracking the resonant feature in the spectrum of scattered or transmitted light [3]. In comparison with SPPs, LSPs generate an electromagnetic field which is more closely tied to the surface of the metal and thus allow for even more localized probing of effects at the interfaces, on the scale comparable with the dimensions of individual biomolecules [4]. Various LSP-based sensor platforms have been developed exploiting LSPs generated on metallic nanopyramids [4], nanorods [5, 6], and chains of coupled nanoparticles [7]. These sensors are typically based on directly illuminating the plasmonic nanostructure with a polychromatic light and measuring changes in the extinction/transmission spectrum [8]. Although LSP-based sensors provide an attractive platform for monitoring interactions of low numbers of biomolecules, their bioanalytical applications have been challenged by the limited number of molecular binding events measured by the sensor and the low concentration of analyte molecules in real-world samples. The results of recent studies suggest that LSP-based biosensors are capable of resolving only a few molecules adsorbed to individual nanoparticles and detecting analytes at low concentrations [9, 10]. However, most of the works demonstrate the detection of biomolecules at nanomolar concentrations and the detection of sub-nM concentrations of biomolecules using LSP-based biosensor has not been convincingly demonstrated.

We report on a new LSP biosensor platform based on the excitation of LSPs on an array of gold nanorods by means of a prism coupler and the total internal reflection. A polarization control scheme (polarization contrast) is employed to take advantage of changes in both the amplitude and phase of the quasi-monochromatic light wave reflected from the array of gold nanorods. It is demonstrated that the presented approach allows for a detection performance comparable with that of the best SPR sensors while requiring a significantly lower number of biomolecular interactions to take place.

#157119 - $15.00 USD Received 2 Nov 2011; revised 5 Dec 2011; accepted 10 Dec 2011; published 23 Dec 2011

2. Surface plasmons in polarization contrast

Surface plasmons are charge density oscillations at a metal-dielectric interface associated with a corresponding electromagnetic field. Localized surface plasmons (LSP) refer to those oscillations confined to sub-wavelength metallic nanoparticles while propagating surface plasmon polaritons (SPP) propagate along a metal-dielectric interface. In general, the coupling of a light wave to a surface plasmon results in a change in the amplitude and phase of the light wave. This phenomenon is illustrated in Fig. 1 which shows the wavelength dependence of light intensity and phase of a light wave coupled to a LSP on a periodic array of gold nanorods on a glass substrate (nanorod dimensions: 40 nm × 110 nm × 30 nm, array periodicity 250 nm × 250 nm). The transmittance and phase of the light wave through the nanorod array was calculated using the finite-difference time-domain (FDTD) method, Fig. 1(a). As follows from Fig. 1, a change in the refractive index of the medium surrounding the plasmonic nanostructure causes a shift in the resonant features in the spectrum of both the light intensity and phase. Similar intensity and phase spectra can be obtained for the light wave coupled to a propagating SPP as shown in Fig. 1(c) and (d) respectively which show light reflectivity as a function of wavelength for a propagating SPP generated via prism coupling on a 50nm thick gold layer.

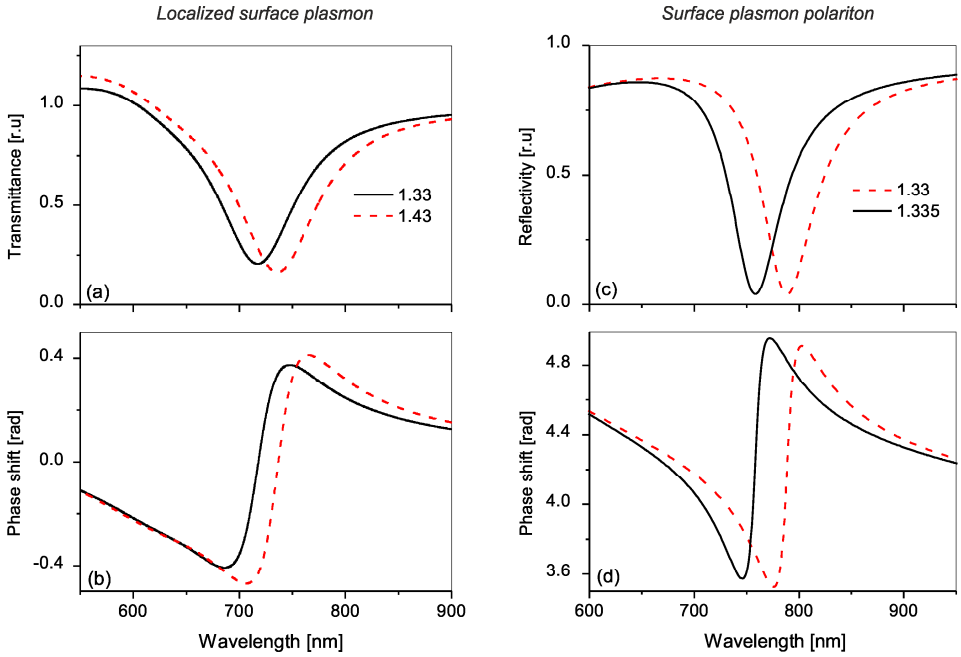

Fig. 1. Wavelength-dependent intensity and phase of a light wave coupled to a LSP on a nanorod array ((a) and (b)) and a propagating SPP ((c) and (d)) calculated for two different refractive indices of adjacent dielectric. a) Transmittance through a nanorod array (ratio of light intensities polarized parallel and transverse to the nanorod axis) and (b) phase-shift (between parallel and transverse polarizations) for a nanorod array. (c) Reflectivity (TM/TE ratio) and (d) phase-shift (TM-TE) for light coupled to a SPP on a 50 nm thick gold film via a prism coupler.

As follows from the comparison of Fig. 1(a) and 1(b) with Fig. 1(c) and 1(d), the sensitivity to the bulk refractive index change is approximately 30 times higher for the propagating SPP than for the LSP. This property is associated with a higher LSP field localization at the metallic nanoparticle [11] and consequently a lower penetration depth of the evanescent field into the dielectric medium. For the considered structure, the penetration

#157119 - $15.00 USD Received 2 Nov 2011; revised 5 Dec 2011; accepted 10 Dec 2011; published 23 Dec 2011

depth of the propagating SPP and LSP was 300 nm and ~9 nm (this is an average figure as the exact field profile of LSP varies along the surface of the nanorod), respectively.

The total internal reflection imaging sensor with polarization contrast takes advantage of both the light intensity changes and phase shift in similar fashion to a previously reported configuration employing a propagating SPP (referred to as SPR imaging) [12]. In this configuration a collimated narrowband light beam passes a prism coupler and is made incident onto a nanorod array attached to the base of the prism (Fig. 2). Upon the incidence on the base of the prism, the light undergoes total reflection and excites LSPs on nanorods via the evanescent field. The amplitude and phase of the reflected light depend on the parameters of the optical system, the parameters of the nanorod array, the polarization of the incident light and the refractive index in the vicinity of the nanorods. When the incident light is linearly polarized and contains both TE and TM polarizations, the light reflected from the array on the nanorods is generally elliptically polarized. The parameters of the polarization ellipse vary with the refractive index in the vicinity of the nanorods and therefore the refractive index changes can be determined by measuring the polarization of the reflected light. By adjusting the phase difference between the TE and TM component (by a waveplate) and selecting an appropriate linearly polarized component (by a polarizer), the sensitivity of the intensity of the light to the refractive index in the vicinity of the nanorods can be maximized. The polarization contrast has been previously used in sensors based on propagating surface plasmons and has been demonstrated to improve the sensitivity and signal to noise ratio by an order of magnitude [13].

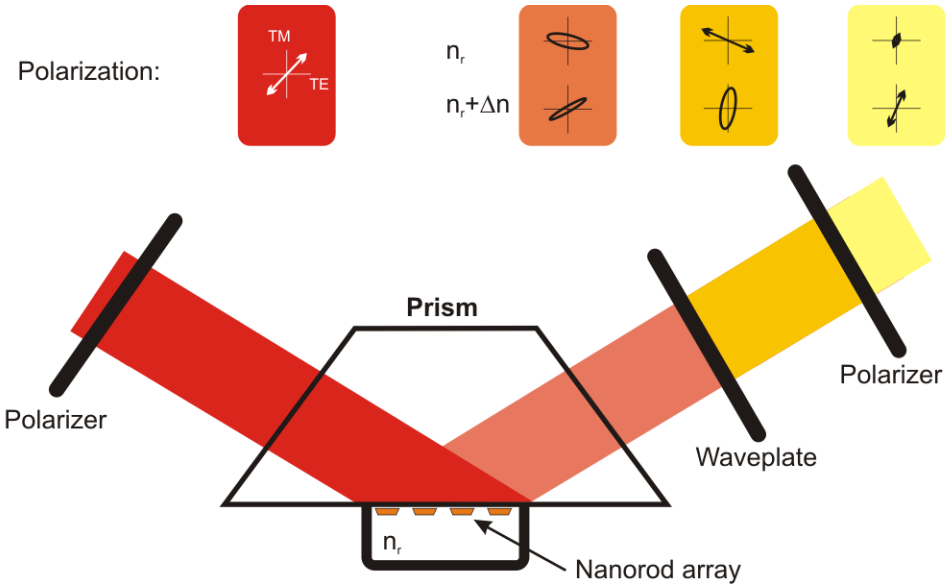

Fig. 2. The concept of an optical sensor based on the excitation of LSPs on an array of gold nanorods by the total internal reflection and polarization contrast (bottom) and the state of polarization of light in different sections of the optical path for two different values of the refractive index in the vicinity of the gold nanorods (top).

The theoretical model of the sensor was developed to predict the response of the sensor and to allow for its performance optimization. The intensity of light transmitted in the polarization contrast was calculated using the previously determined amplitude and phase using the Jones calculus (Fig. 3(a)). As for nanoparticles much smaller than the wavelength, the coupling to LSP has only a weak dependence on the angle of incidence [14], the theoretical model of LSP coupling with a normally incident light wave can be considered to also model the LSP coupling via the evanescent wave in the attenuated total reflection

#157119 - $15.00 USD Received 2 Nov 2011; revised 5 Dec 2011; accepted 10 Dec 2011; published 23 Dec 2011

geometry. The plot in Fig. 3(a) corresponds to the input polarizer set to 53 deg, the waveplate set to −48 deg, and the output polarizer at −39 degrees with respect to the plane of incidence. The simulations suggest a nearly linear dependence of intensity on the change in bulk refractive index and a sensitivity of 700 per cent per RIU (relative intensity change normalized to a refractive index unit). Using the theory described in Ref [15], we compared the performance of the proposed approach and the approach based on spectroscopy of LSPs on the same array of metallic nanorods. Theoretical analysis revealed that the approach based on the total internal reflection and polarization contrast allows for measuring changes in the refractive index at the surface of the nanorods with a resolution twice as good as that provided by spectroscopy of LSPs (the simulations were performed assuming averaging over the area of 400 detector pixels and 100 acquired images, and a shot noise equal to 0.6% of the measured intensity).

The arrays of gold nanorods were fabricated by electron beam lithography using positive resist poly(methyl methacrylate) (PMMA) on glass substrates covered with a 10 nm-layer of indium-tin-oxide (ITO). By incorporating a transparent and conductive layer of ITO, charging of the substrate during e-beam exposure was suppressed. Following exposure, the PMMA layer was developed and the substrates were coated with a gold layer by means of thermal evaporation. A 0.5 nm thick chromium layer was used to promote adhesion of the gold to the substrate. The preparation of the nanorod arrays was completed by lift-off in acetone. The produced nanorod arrays were characterized using scanning electron microscopy (SEM). The inset in Fig. 3(b) shows a part of a resulting nanorod array. The thickness of the gold layer was determined to be 30 nm using a stylus profilometer (Alphastep, Tencor Instruments). The dimensions of the nanorod were measured from SEM image to be 40 nm x 110 nm. The substrate comprising two identical nanorod arrays for sensing and reference channels was interfaced with the prism in such a way that the longer axis of nanorods is parallel to the plane of incidence. In the experiments, the incident light was linearly polarized approximately at 45 deg with respect to the plane of incidence. The waveplate and analyzer were adjusted to maximize the sensitivity of the sensor to changes in the refractive index of the medium adjacent to the nanorods. In order to achieve high performance in which the sensor operates in the shot-noise limited regime, two gold mirrors were prepared on the prism surface. The light blocked and reflected by these mirrors provides dark and bright reference signals for real-time compensation of fluctuations in the intensity of stray light and incident light, respectively. Images acquired from the CCD camera were averaged (100 frames per record) and intensities from pixels within each measurement area were binned. The area of the sensor surface imaged on the CCD camera was 6.4 mm × 9 mm. An acrylic flow cell with gaskets made of vinyl adhesive foil of a total thickness of 50 μm was pressed against the sensor chip to contain the liquid sample during the experiment. A broadband halogen light source and a spectrometer were used to assist in identifying the optimum polarization contrast. Once the polarization contrast was optimized, a low-coherence narrowband light source (superluminescent diode, central wavelength 780 nm, spectral width 10 nm) and a CCD camera were mounted to image both sensing and reference channels.

As follows from Fig. 3(b), the experimentally obtained spectrum agrees closely with the theoretical model of the LSP in polarization contrast. However, the experimentally obtained spectrum contains a peak corresponding to a polariton at a wavelength different from the LSP resonance. The polariton originates from a dipolar interaction of metallic nanoparticles provided by the grazing diffraction mode of the nanostructure when the light fields corresponding to the −1st order change from evanescent to radiative [16].

#157119 - $15.00 USD Received 2 Nov 2011; revised 5 Dec 2011; accepted 10 Dec 2011; published 23 Dec 2011

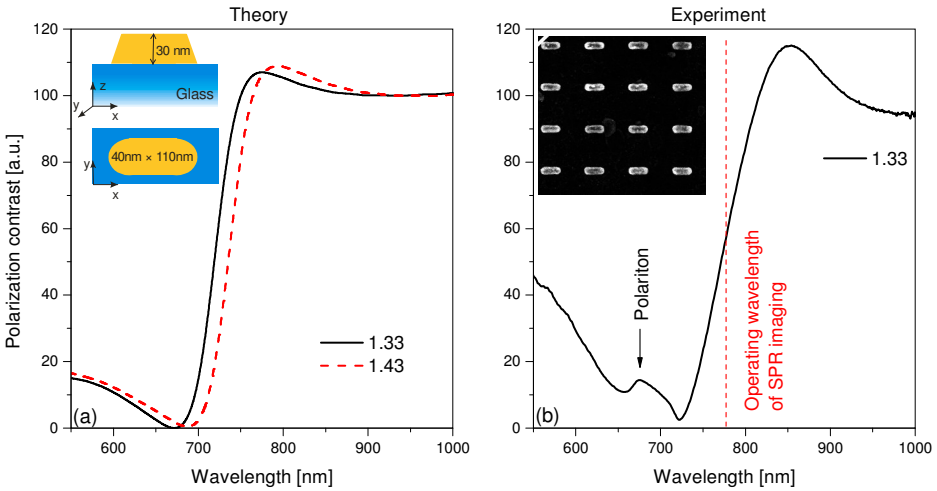

Fig. 3. Wavelength spectrum of the light intensity in polarization contrast configuration. (a) Calculated spectra based on the FDTD model and (b) measured spectra of the fabricated nanorod array.

3. Characterization of the LSP-based biosensor

In general, the sensitivity of LSP-based biosensors depends strongly on the distance from the surface at which the interaction between the biorecognition element and the analyte molecule takes place. In order to account for this feature, the sensitivity of the biosensor at different distances from the surface was characterized by measuring the sensor response to the formation of a multilayer of bovine serum albumin (BSA). Prior to the experiment, the substrate comprised of nanorod arrays was cleaned with UV/O_3 and mounted to the sensor system. Citrate buffer (10 mM sodium citrate, 1 mM sodium hydroxide, pH 4 at 25°C) was flowed across the sensor surface. After 5 minutes in the buffer, the BSA solution (500 µg/mL) was injected in the flow-cell. The solution was flowed through the flow-cell until the sensor response leveled off which corresponds to the surface coated with a monolayer of BSA (after approximately 10 minutes). Then, the sensing surface was washed with CB and solution of dextrane sulfate (DS) (1 mg/ml) was flowed over the BSA monolayer for 10 minutes. Negatively charged DS molecules adsorb electrostatically to the positively charged BSA monolayer creating a foundation layer for adsorption of another layer of BSA. In our experiments, a total of 9 BSA monolayers were formed on the sensor surface by using this approach (for the sensorgram, see Fig. 4(a)).

Considering the thickness of one BSA monolayer to be approximately 5 nm [17], the dependence of the sensor sensitivity on the thickness of the biomolecular layer thickness was reconstructed. The first layer was excluded from this analysis as BSA monolayers adsorbed directly on gold exhibit different properties than those adsorbed on the previously adsorbed BSA/DS molecules. Figure 4 depicts the dependence of the LSP sensor response to one BSA monolayer as a function of the distance from the sensor surface at which the adsorption took place. This dependence exhibits an exponential behavior which can be split into two contributions: (i) the contribution to the sensitivity from the LSP which is dominant in close vicinity to the surface and (ii) a weak contribution originating from the residual polariton which prevails at greater distances from the sensor surface (> 40 nm). Due to the setting of the polarization contrast these two effects influence the sensor response in opposite directions and at a distance of around 30 nm from the sensor surface cancel each other (resulting in zero sensitivity to the formation of the BSA monolayer). Therefore in order to operate the sensor within the LSP sensing mode, the biomolecular interactions under investigation should take place within 30 nm from the surface of the nanorods.

#157119 - $15.00 USD Received 2 Nov 2011; revised 5 Dec 2011; accepted 10 Dec 2011; published 23 Dec 2011

In order to quantify the surface concentration of adsorbed biomolecules and calibrate the biosensor sensitivity, the experiment was repeated using a laboratory sensor based on propagating SPPs (PLASMON IV) developed at the Institute of Photonics and Electronics, Prague, Czech Republic [18]. By comparing results from the two sensing platforms, a surface concentration of 3 ng × mm^2 was found to correspond to each monolayer of BSA. Assuming that the adsorption of BSA is driven by its interaction with the BSA/DS layer regardless of the surface geometry on a large scale, a monolayer with the same surface density can be achieved on the nanorod array. This implies that for the nanorod array one monolayer contains about 100 BSA molecules per nanorod. This surface density corresponds approximately to a geometrical consideration of a densely packed monolayer of ellipsoidal molecules with the dimensions of 9 nm × 5 nm × 5 nm.

The standard deviation of the baseline noise obtained during monitoring of the formation of the BSA multilayer was 1.4 × 10^{-4} (arbitrary units used in the plot) yielding an RMS-based resolution of surface coverage of 35 fg × mm^{-2} (relative to the area including both the Au and ITO surfaces). This minimum detectable surface coverage corresponds to about 0.03 BSA per nanorod, or one BSA molecule per 35 nanorods. Typical sensors based on spectroscopy of LSPs measure changes in the position of the peak in the extinction/transmission spectrum with an accuracy in the order of 0.01-0.1 nm [19, 20]. The accuracy with which the intensity of light is measured in the presented sensor corresponds, in terms of the response of the spectroscopic LSP sensor, to a change in the resonant wavelength in the order of 10^{-4} nm. A similar level of performance has recently been demonstrated by Chen et. al [9] who also achieved the minimum detectable surface coverage of 40 fg × mm^{-2}.

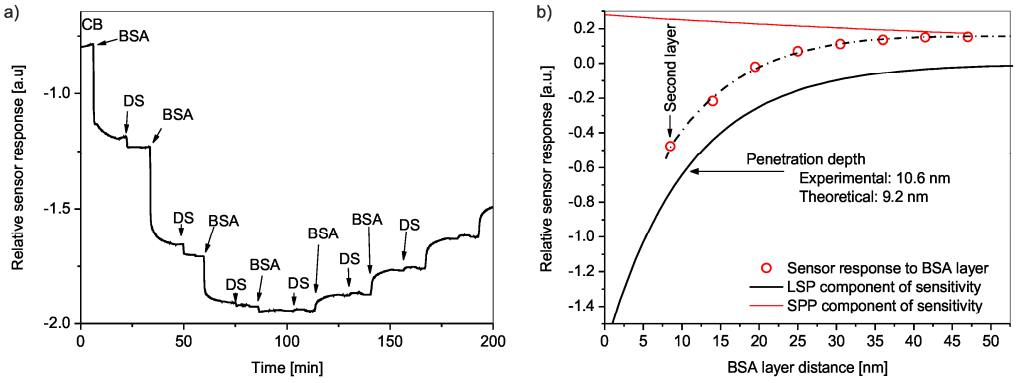

Fig. 4. Calibration of the LSP-based sensor using a BSA multilayer. (a) Temporal sensor response to the formation of the BSA/DS multilayer. (b) Sensor sensitivity as a function of the distance from the surface of the nanorod array (red circles) and the two contributions associated with LSP (black line) and the polariton (red line).

4. Detection of oligonucleotides

To assess the detection capabilities of the LSP-based imaging biosensor a model biodetection experiment was carried out in which short oligonucleotides were detected via complementary oligonucleotides immobilized on the sensor surface. The nanorod arrays were first functionalized with a self-assembled monolayer of ω-carboxyalkylthiols on which streptavidin was attached via the amide bond. Subsequently, biotinylated oligonucleotides were attached to the streptavidin via the streptavidin-biotin link. The immobilization procedure is described below. First, the substrates were immersed overnight in 1 mM solution of (1-mercapto-11-undecyl)hexa(ethylene glycol) carboxylic acid (HSC11–EG6–OCH2–COOH) and dissolved in absolute ethanol to form a self-assembled monolayer of carboxyl terminated alkanethios. Then the substrates were mounted into the SPR sensor and the

#157119 - $15.00 USD Received 2 Nov 2011; revised 5 Dec 2011; accepted 10 Dec 2011; published 23 Dec 2011

carboxylic terminal groups of the alkanethiols were activated with a mixture of 0.5M1-ethyl-3-(3-dimethylaminopropyl)-carbodiimide (EDC) and 0.1M N-hydroxysuccinimide (NHS) from GE Healthcare, USA. Subsequently, a 50µg/mL solution of streptavidin (Sigma–Aldrich, USA) in 10mM sodium acetate buffer (pH 5.0) was introduced to the flow-cell for 10 min. The non-covalently bound streptavidin was removed with high ionic strength buffer saline. Finally a 100 nM solution of biotinylated DNA probe (Biotin-$(TEG)_2$—5′-TAT TAA CTT TAC TCC CTT CC-3′) in tris buffer with 500mM NaCl was flowed along the sensor surface for 15 min. The sensing channels functionalized only with the self-assembled monolayer of alkanethiols were used as reference.

Freshly functionalized nanostructures were immediately used for experiments. The sensor was exposed to DNA (5′-GGA AGG GAG TAA AGT TAA TA-3′) molecules complementary to the probes immobilized in the sensing channel contained in tris buffer with 500mM NaCl. In the detection experiment, the following concentrations of DNA targets were used: 500 pM, 1 nM, 5 nM, 10 nM, and 100nM. The sensor response obtained in the reference channel was subtracted from the one obtained in the sensing channel and recalibrated to the surface coverage using the calibration described in the previous section. For the sensitivity calibration the distance of the hybridization reaction from the nanoparticle surface was estimated based on the thickness of the self-assembled monolayer of alkanethiols of 3.5 nm [21], streptavidin size of 5 nm [22] and the length of the DNA probe of 6 nm. Therefore the DNA interaction was assumed to take place at a distance between 8 nm and 14 nm from the nanoparticle surface (this corresponds to the third BSA monolayer used for the calibration experiment).

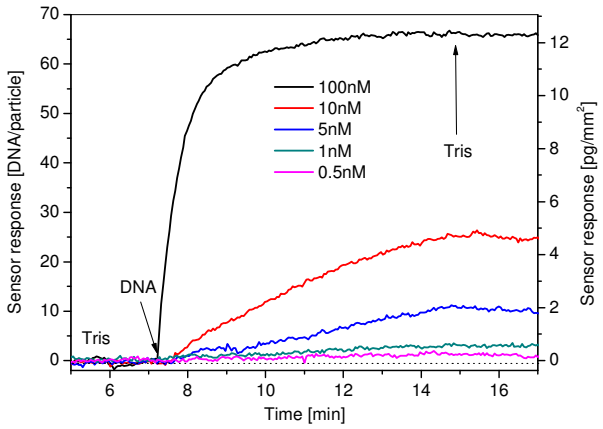

Fig. 5. Temporal response of the LSP-based sensor to five different concentrations of target oligonucleotides.

Figure 5 depicts the temporal sensor response to the hybridization of DNA molecules at the surface of the nanorod array. Clearly, the injection of the DNA sample in the flow-cell results in a strong sensor response, indicating that DNA hybridization takes place. The increase in the sensor response saturates for the highest DNA concentration at the surface coverage of 65 DNA/particle. The lowest concentration of DNA (500 pM) which corresponds to a surface coverage of only 1 DNA molecule per particle results in a sensor response above the baseline noise level. The standard deviation of baseline noise corresponded to only about 0.2 DNA/particle (35 fg × mm^{-2}). A calibration curve was created using the initial binding rate (determined from the initial linear portion of the binding curve) as a sensor output, Fig. 6. The binding rates obtained in the reported experiments are directly proportional to the

#157119 - $15.00 USD Received 2 Nov 2011; revised 5 Dec 2011; accepted 10 Dec 2011; published 23 Dec 2011

concentration which is in agreement with previous studies of DNA hybridization using SPR biosensor technology [18].

The limit of detection (LOD) (defined as the sample concentration which corresponds to the sensor response equal to three standard deviations of the sensor response to a blank sample) was determined to be approximately 200 pM (it should be noted, that this LOD applies to the detection of target DNA in buffer and would be higher in complex samples due to the non-specific interaction between the sensor and complex sample matrix [17]). This LOD is comparable with the LODs obtained using the high-performance SPR biosensors which have detected DNA at nM [23] or 100 pM levels [18, 24]. This result clearly indicates that although the LSP-based biosensor can detect numbers of molecules by orders of magnitude lower than their propagating SPP-based counterparts, the resulting analytical performance of both these approaches is approximately the same. This outcome is mostly due to the kinetics of interacting molecules as the probability of the biomolecular interaction is directly proportional to the number of the interacting molecules.

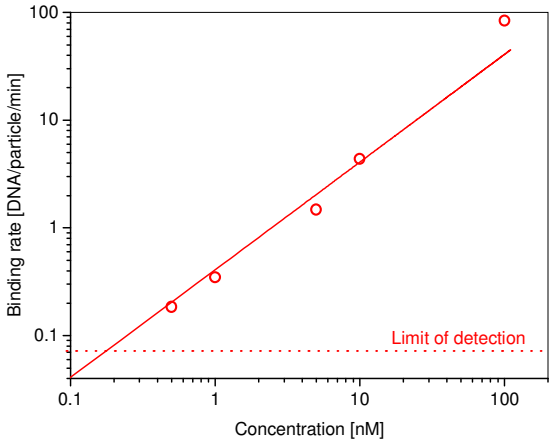

Fig. 6. Calibration curves obtained for the detection of short oligonucleotides. The solid line corresponds to a linear fit through zero.

5. Conclusion

A new approach to the development of high-performance biosensors based on localized surface plasmons (LSPs) is reported. The presented approach is based on the imaging of surface plasmons in polarization contrast and takes advantage of the change in the polarization of light coupled to localized surface plasmons on a gold nanorod array. It is shown that the LSP-based biosensor delivers the same high performance as state-of-the-art SPR biosensors while involving a two orders of magnitude lower number of molecular interactions. We demonstrate that the sensor is capable of detecting only one short DNA molecule per nanoparticle on average and measuring concentrations of short oligonucleotides down to 200 pM. Moreover, the implementation of the LSP-based biosensor is implicitly multichannel and potentially offers high throughput.

Acknowledgments

This research was supported by the Academy of Sciences of the Czech Republic under the contract KAN200670701 and Praemium Academiae, by the Ministry of Education, Youth and Sports under contract OC09058, by COST Action MP0803, and by the European Science Foundation (ESF) under the activity PLASMON-BIONANOSENSE.

#157119 - $15.00 USD Received 2 Nov 2011; revised 5 Dec 2011; accepted 10 Dec 2011; published 23 Dec 2011